Bio-Inspired Visuomotor Convergence in Navigation and Flight Control Systems

Thesis by

James Sean Humbert

In Partial Fulfillment of the Requirements

for the Degree of

Doctor of Philosophy

California Institute of Technology

Pasadena, California

2005

(Defended June 2, 2005)

Acknowledgements

First and foremost, I would like to acknowledge my advisor Richard Murray. Throughout the duration of my time at Caltech, Richard provided an environment with the highest level of professionalism and expectation. Thanks for the financial and intellectual support, the freedom, and the flexibility that was so generously extended; for these things I owe a large debt of gratitude. I wish to thank the other members of my committee: Michael Dickinson, Doug MacMynowski, and Joel Burdick. Michael's integrated approach to the study of insect behavior is both revolutionary and refreshing, and was instrumental in the development of this thesis topic. Thanks to Doug and Joel for their interest and time; their constructive comments significantly improved the quality of this work. I also wish to thank my undergraduate advisor from UC Davis, Art Krener. Without the opportunities that Art provided during my time as an undergraduate, I would not be where I am today.

Gracious thanks are due to all of my family and friends; especially to my grandmother, Peg, for giving me the strength to pursue my dreams, and my late grandfather, Chuck, to whom I dedicate this thesis. I hope someday my accomplishments will be able to stand shoulder to shoulder with yours. Thanks to all the members of El Toro Guapo, our championship Red Bull Flugtag team, and thanks to all of my Southern California friends: James, Bob, Richie, Shawn, Brian, Ilias, Eimear, and Ross. We've had an amazing four years, and I have no doubt the next will be equally memorable.

Lastly, I wish to acknowledge the financial support for this research, including the Army Research Office (ARO) Institute for Collaborative Biotechnologies program under grant DAAD19-03-D-0004 and the Air Force Office of Scientific Research (AFOSR) under grant F30602-01-2-0558.

Abstract

Insects exhibit incredibly robust closed loop flight dynamics in the face of uncertainties. A fundamental principle contributing to this unparalleled behavior is rapid processing and convergence of visual sensory information to flight motor commands via spatial wide-field integration, accomplished by retinal motion pattern sensitive interneurons (LPTCs) in the lobula plate portion of the visual ganglia. Within a control-theoretic framework, an inner product model for wide-field integration of retinal image flow is developed, representing the spatial decompositions performed by LPTCs in the insect visuomotor system. A rigorous characterization of the information available from this visuomotor convergence technique for motion within environments exhibiting non-homogeneous spatial distributions is performed, establishing the connection between retinal motion sensitivity shape and closed loop behavior. The proposed output feedback methodology is shown to be sufficient to give rise to experimentally observed insect navigational heuristics, including forward speed regulation, obstacle avoidance, hovering, and terrain following behaviors. Hence, extraction of global retinal motion cues through computationally efficient wide-field integration processing provides a novel and promising methodology for utilizing visual sensory information in autonomous robotic navigation and flight control applications.

Contents

List of Figures

List of Tables

Chapter 1

Introduction

Insects represent incredible efficiency and diversity, with millions of existing species backed by over 350 million years of evolutionary design. Flying insects, in particular, are micro-miniaturized packages capable of efficient and effective visual-based navigation. In spite of the size and simplicity of their nervous systems, they represent the highest standard for performance and robustness in flight control and navigation of uncertain environments. On the other hand, local maneuvering and obstacle avoidance in cluttered environments poses a significant challenge for autonomous, unmanned aerial vehicles (UAVs) in operational scenarios. With the current limitations, agile, near-ground flight is impractical. Simple, robust, and lightweight solutions are required for autonomous behavior to be achievable within the power, weight, and size constraints of a miniature UAV. Despite these challenges, artificial vision-based systems appear to be essential to the development of truly autonomous UAVs, especially for near-ground flight.

A characteristic of typical vision sensors is that they provide a vast amount of information at any given time instant. Hence, any successful vision-based navigation algorithm must be able to rapidly and intelligently parse this information to provide appropriate motor control signals at required servo rates. Current research in autonomous visual navigation has focused on several useful, but complex algorithms that involve (but are not limited to) feature detection, extraction, and classification as well as simultaneous localization and mapping (SLAM). Nature, on the other hand, has developed elegant and simple solutions to the problems of perception and navigation as evidenced by a comparison of the computation power required for implementation. Insect brains pack approximately 330,000 neurons – about 2/3 of which are dedicated specifically to visual processing – in a volume smaller than a sesame seed, whereas typical robotic platforms that implement the algorithms de-

scribed above require several state of the art computer processors. If one does a neuron to transistor comparison, there is a difference of *several* orders of magnitude, all without the accompanying performance and robustness that is seen in nature. The fundamental principles inherent to insect navigation are both elusive and promising candidates for closing the considerably large gap in performance and robustness that exists between biological systems and their robotic counterparts.

As the important details of the biology are uncovered through behavioral and neurophysiological studies, the challenge is not only to develop appropriate mathematical models of these processes but also to understand how information is integrated at the system level to control locomotion. This thesis, through rigorous modeling and characterization of the control-relevant information available through wide-field integration of retinal image flow, is a dedicated effort to unravel the visuomotor convergence properties that provide the performance and robustness that is seen in the natural world.

1.1 Review of the Insect Visuomotor System

Prevalent in many natural sensory systems is the phenomenon of sensorimotor convergence, wherein signals from arrays of spatially distributed and differentially tuned sensors converge in vast numbers onto motor neurons responsible for controlling locomotive behavior. A prime example occurs in the processing of retinal image pattern movement (optic flow) by the visuomotor systems of insects (Figure 1.1). Insect visual systems encode optic flow by combining motion estimates from arrays of local movement detectors in a way that preserves the spatial layout of the retina [15]. This spatially preserved motion information is parsed by wide-field motion sensitive interneurons in the lobula plate section of the visual ganglia (called tangential cells, or LPTCs for short). The output of these neurons is communicated via decending neurons to the motor control centers, creating a sensory processing front end that spatially integrates the optic flow [6]. This visuomotor convergence technique, spatial wide-field integration, is presumed to be used by insects to extract behaviorally relevant information from optic flow patterns to modulate the kinematics of flight.

Early Stages of Visuomotor Processing

As an insect moves through an environment, patterns of luminence form on the retina

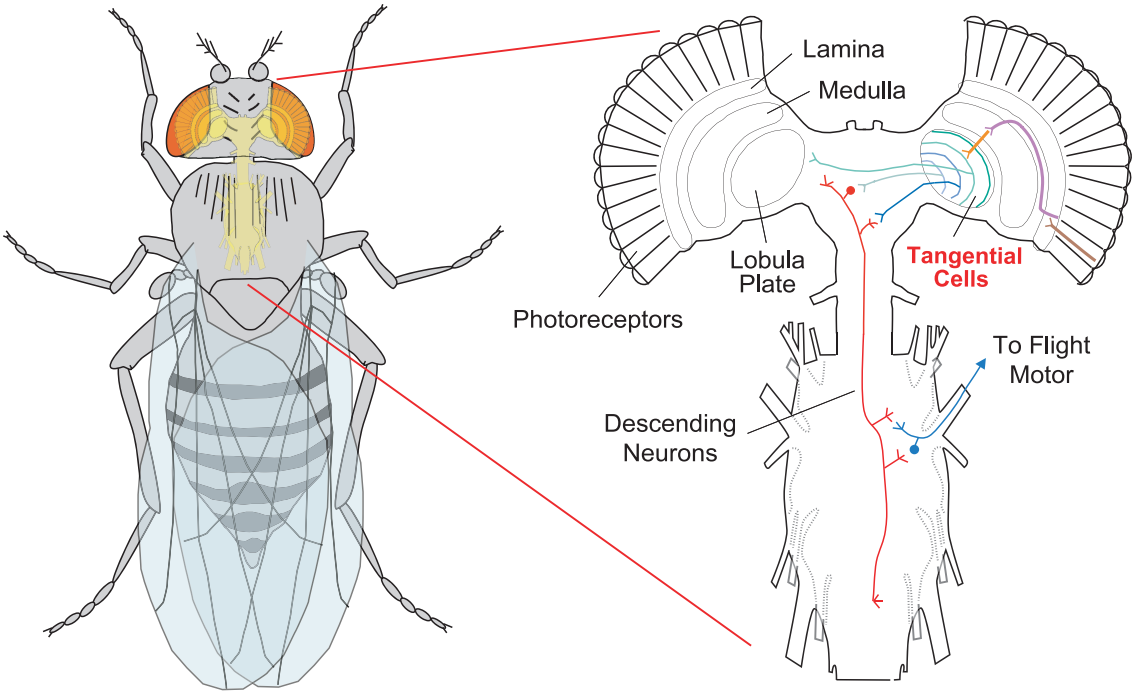

Figure 1.1: Visuomotor system of *Drosophila*

of the compound insect eye. The individual units of the eye, or ommatidia, are essentially bundles of photoreceptors that provide an estimate of the brightness over a specific patch of the visual space. In the case of *Drosophila melanogaster*, the 1400 ommatidia (700 per eye) can sample roughly 85% of this visual space [34]. Photoreceptor axons synapse in the region of the insect brain called the visual ganglia, composed of three successive layers termed the lamina, the medulla, and the lobula complex. The lobula complex is composed of two regions, the lobula and the lobula plate, that receive input in parallel from the medulla. Shown in Figure 1.1 is the pathway through the lobula plate, as this is the processing layer of interest. These layers of neuropile maintain the spatial organization of photoreceptor inputs, and therefore relationships between adjacent ommatidia are conserved within the nervous system [6]. The patterns that form on the retina are time dependent and are a function of the particular kinematics of the motion as well as the spatial layout of the environment [41], and therefore contain critical information useful for stabilization and navigation tasks. The magnitude and direction of these local image shifts, taken over the entire visual space, form

what is known as the retinal motion field, also called the *optic flow field*.

Insect visuomotor systems do not have access to this field directly; however, it is hypothesized that they compute local estimates based on two-dimensional arrays of movement detectors [15]. Reichardt and Hassenstein proposed an elementary local motion detection model [48], consisting of asymmetrical input channels correlated with a nonlinear (multiplicative) element. Due to the dynamics inherent to this structure, a perfect estimate of local image velocity is not possible, but rather it depends characteristically on the structure and properties of the retinal pattern [26], [50]. This arrangement forms a discrete array of directionally selective and spatially organized estimates that is subsequently passed to the wide-field sensitive visual interneurons in the lobula plate section of the visual ganglia, also known as the tangential cells (Figure 1.1).

Wide-Field Motion Sensitive Tangential Neurons

Organized in the third visual neuropile of each hemisphere, a region referred to as the *lobula plate* (Figure 1.1), are approximately 60 tangential interneurons (LPTCs) that receive spatially organized dendritic input from local movement detectors [5], [43]. Early experimental research showed these neurons to be an essential component of visually mediated behaviors [24], [33]. Axons typically project to three locations including the outputs of the visual ganglia (descending cells), the contralateral half of the brain, and others, termed centrifugal cells, are presynaptic in the lobula plate and postsynaptic in the central brain [30], [23]. Descending cells, which receive dendritic input from LPTCs, drive motor neurons controlling the steering muscles of the mechanosensory halteres, which provide input to neurons controlling wing kinematics [22], [29].

Early studies of these neurons focused on structure, arrangement, and synaptic connectivity [62]; however, recent developments in experimental capabilities have provided various classifications based on response characteristics (for an extensive review, see [6]). Notable are the groups of horizontal (HS) cells [31] and vertical (VS) cells [35], whose receptive field organization and response characteristics have been studied extensively [32], [42]. Due to their receptive field structure, which is similar to the equivalent projected velocity fields for certain cases of rotary self motion, these neurons are thought to contribute to stabilization and course control [42], [16]. In addition, there is evidence for existence of more complicated, translational-like pattern sensitivities as seen in the Hx cells [42]. Significant progress

has been made in understanding how insect visual systems encode behaviorally relevant information [16]; however, the exact functional role that each of these neurons hold in the stabilization and navigation system of the fly remains a challenging and open question.

1.2 The Matched Filter Concept

Since optic flow was first recognized as a critical source of information [25], there has been considerable interest in adapting this type of sensory system for bio-inspired autonomous navigation. One concept that has recently received a significant amount of attention is that of the biological *matched filter* [67], where the neural images formed from sensory inputs are compared with pre-determined templates, presumably to assist in determination of behavioral responses. As receptive field structure of particular VS and HS tangential cells [32], [42] have revealed similarites to the equivalent projected velocity fields for certain cases of rotary self motion, it has been postulated [43] that LPTCs extract particular types of self-motion from optic flow fields.

Investigations comparing VS neuron receptive field organizations and matched filter models based on rotary optic flow fields have been performed [19]. The models, comprised of weighted sums of optic flow components, were generated using an optimality principle that minimized the variance of filter output caused by noise and variability of the distance distribution from scene to scene. In order to perform these calculations, knowledge about the distance statistics of the environment, self-motion, and EMD noise had to be assumed. It was concluded that some of the VS neurons are optimized for detecting the sign of rotary optic flow about selected axes; however none were able to code the rotation rate.

In a classical linear estimation approach, the same type of LPTC-based processing model mentioned above has been investigated as an estimator for robot kinematic states directly from observed optic flow [18]. In this case, however, the quadratic error in the estimated motion parameters was minimized instead of output variance about fixed motion axes. To compute the weights used in the estimator, prior knowledge about the particular environmental distance distribution and about the noise and egomotion statistics of the sensor were used. In order to compute the distance statistics, a robot was sent around the environment along prescribed trajectories recording the distance information. From the measurements, an average distance and covariance were computed. The noise statistics were determined

by presenting the flow algorithm with artificially translated images of the laboratory environment. It was concluded that with the aid of detailed prior knowledge of the specific environment, rotation estimates were fairly reliable; however translation estimates were difficult due to variability of spatial structure from scene to scene.

There are several points that should be noted regarding the performance of these types of matched filter implementations. Firstly, optic flow is inherently a *relative* measurement; that is to say, it is a measure of effective angular image velocity or speed/depth. The implementations described above are attempting to estimate *absolute* quantities (rotational and translational velocities) that would presumably be utilized in a closed feedback loop. The difficulty is evident when you consider utilizing the approach above for estimating the same egomotion for a robot that is translating through two distinct environments. The motion is the same, but the optic flow, and more specifically the estimated egomotion parameters, can be drastically different from environment to environment. Secondly, detailed statistics regarding the particular environment as well as the noise and egomotion of the sensor were required in order to achieve the results obtained. Presuming that insects do collect this information, as evidenced by the fact that LPTC receptive field organization does not depend on visual experience [39], the navigational robustness of insects with respect to different environments suggests other principles might be at work. Lastly, it has been shown that the particular receptive field sensitivites that have been measured experimentally are not optimal for extracting the magnitude of rotational and translational velocity measurements when utilized in estimation approaches described above, and at most can predict the presence and the sign of a specific egomotion component [11].

1.3 Global Optic Flow Cues for Navigation

While there have been extensive research efforts focused on understanding the neurobiology of the insect visuomotor system, there have also been efforts that have focused on understanding the function of this complex sensory and control system from a behavioral point of view. In this context, LPTCs are interpreted as an intermediate processing layer that extracts specific global cues from the complicated patterns of retinal motion that presumably are useful for navigational and stabilization tasks. Most notably, the classical *optomotor response* has received a significant amount of attention over the past 40 years [27], [28], [49].

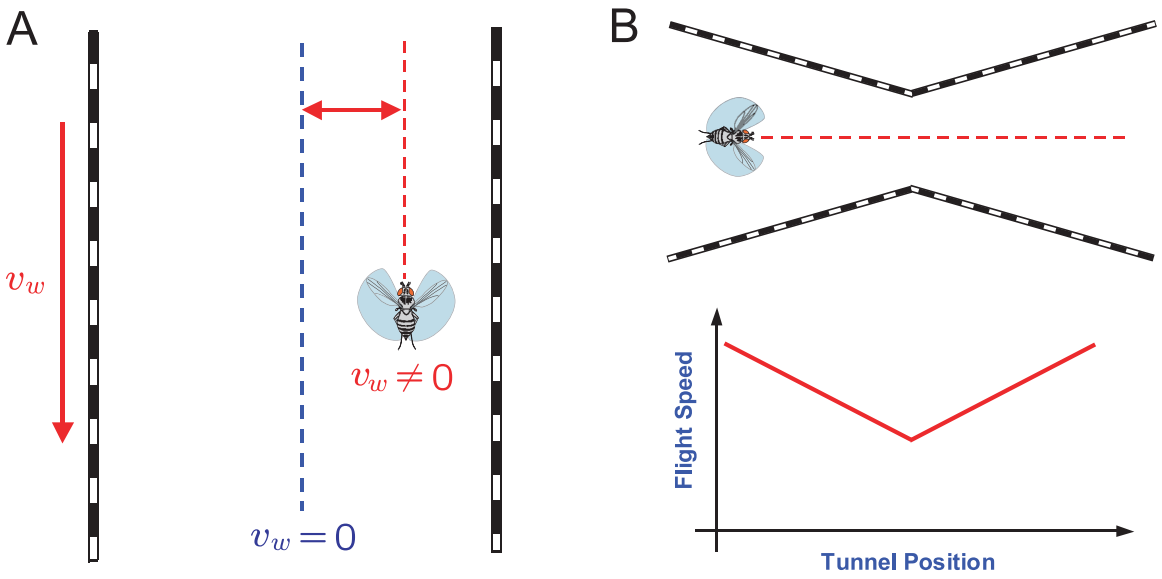

Figure 1.2: Navigation with global optic flow cues. (A) The centering response; insects adjust their flight path in order to balance the effective angular velocity induced by wall motion. (B) The forward speed regulation response; insects modulate forward speed based on the average global image velocity.

In these investigations it was found that the visuomotor systems of tethered flies robustly generate torques to minimize large-field rotational motion on their retinas.

Recently explored behaviors have shown that visual cues derived from optic flow might be used to accomplish far subtler tasks [56]. In experiments with honeybees, *centering* and *forward speed regulation* responses were studied [58], [60], and in *Drosophila*, the forward speed regulation response was studied in [12]. These reflexive behaviors are different from the optomotor response in a very fundamental way; the optomotor response attempts to regulate a retinal equilibrium of zero image velocity, whereas the centering and forward speed responses regulate nonzero retinal image motion patterns. This suggests that insects might be attempting to regulate spatial structure of retinal image flow instead of a global average or uniform balance, as previously hypothesized, over the two hemispheres.

The centering response states that in order to negotiate a narrow gap, an insect must balance the speeds of the image velocity on each retina. This heuristic was postulated based on the well-known facts that insects have immobile eyes with fixed-focal length optics and hence are unable to reliably estimate range to objects via binocular stereopsis [59]. In experiments bees were trained to fly down a tunnel to collect a sugar reward. The flight paths of the bees were investigated as a wall of the tunnel aparatus, consisting of a grated

pattern, was given motion. With no wall motion, the flight path of the bees tended to be directly down the center. However, when the wall was given motion, the flight paths of the bees shifted. For motion along (against) the flight direction, the induced image velocity on the corresponding retina is reduced (increased), and hence the flight paths were seen to shift towards (away from) the moving wall. The conclusion from the experiments is that the bees were in some sense *balancing* the image speeds on their retinas.

The forward speed regulation response, in this case of *Drosophila*, was investigated in [12]. In these experiments flies navigating a cylindrical tunnel were held stationary by rotating the walls of the cylinder, and hence inducing backward pattern motion indicative of forward flight. The flies were also observed to modulate thrust to compensate for wind in order to hold the angular velocity of the image constant. In separate experiments this behavior was investigated in bees using a converging-diverging tunnel aparatus [60]. As bees negotiated the tunnel, they were found to regulate their forward speed in proportion to tunnel width, i.e., a more narrow tunnel dictates a reduced speed. The conclusion was that the bees were holding the apparent angular velocity of the retinal image induced by the walls at 320 deg/s.

1.4 Visually Mediated Wind Disturbance Rejection

Recent experimental results [64] demonstrate that flies posses a robust tendency to orient towards the frontally-centered focus of the visual motion field that typically occurs during upwind flight. In these experiments large-field visual motion stimuli were presented in open loop to tethered flies (Figure 1.3). A–D shows the averaged turning response of the flies measured from an optical sensor that records wing activity. Figure 1.3A corresponds to the classic optomotor response [27], in which the fly responds to coherent full field rotatory motion by turning to minimize retinal slip. The plots in B and C show the mean response of the fly to front- and rear-field rotatory motion. The response in A is shown to be the sum of the responses in B and C (dashed line). However, the response in C, clearly contradicts the predictions of the optomotor response, since the attempted turn is not in the direction that would minimize the rotatory stimuli. The response in D shows that the strongest response is obtained when the fly attempts to orient towards a contracting focus of the motion stimulus. This shows that the fly can detect the location of the visual focus of contraction (or is doing

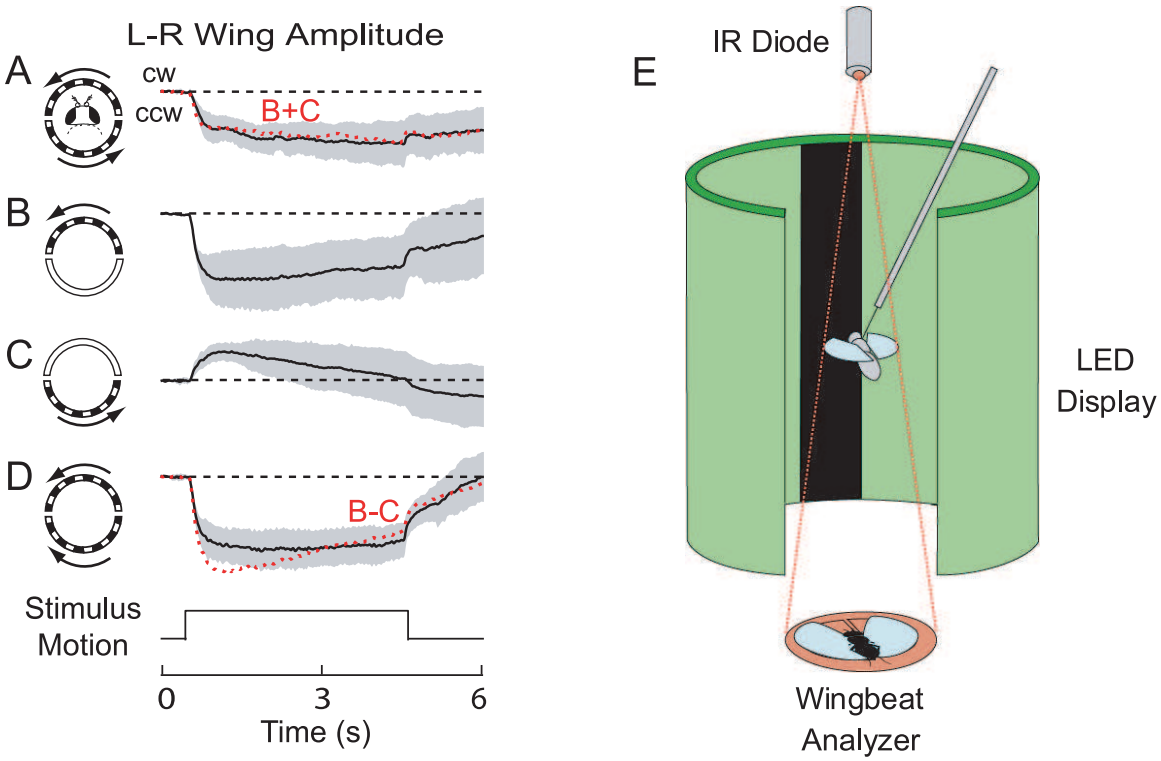

Figure 1.3: Open loop visuomotor reflexes in *Drosophila*. (A-D) The quantity plotted on the vertical axis is the difference between the right and left wing beat amplitudes measured by an optical sensor. Each trace represents the mean ± S.D. (shaded area), from 10 flies. These data have been replotted from Tammero *et. al.*, 2002. (E) Experimental setup. Tethered flies are presented with visual stimuli, and the left minus right wingbeat response is measured using an IR-based wingbeat analyzer.

something functionally equivalent). The focus of contraction (expansion) is the point of no motion in a velocity field induced by pure translation, which all motion vectors point towards (away from). These data suggest that a control algorithm based on feedback of the movement of the visual focus of contraction could be used to detect wind direction, since upwind flight induces a frontally centered focus of the visual motion field.

In [51] we sought to answer the question of how an insect is able to extract this global optic flow cue based on the known visual processing capabilities available through the lobula plate tangential cells. As the experimental evidence described in Section 1.1 suggests, LPTCs perform a spatial decomposition of the retinal motion field. Mathematically, this operation can be represented by an inner product (Appendix A) between the instantaneous optic flow field and a set of spatially defined functions representing the visual motion pattern sensitivity of each specific LPTC. Under a planar model assumption, both the optic flow

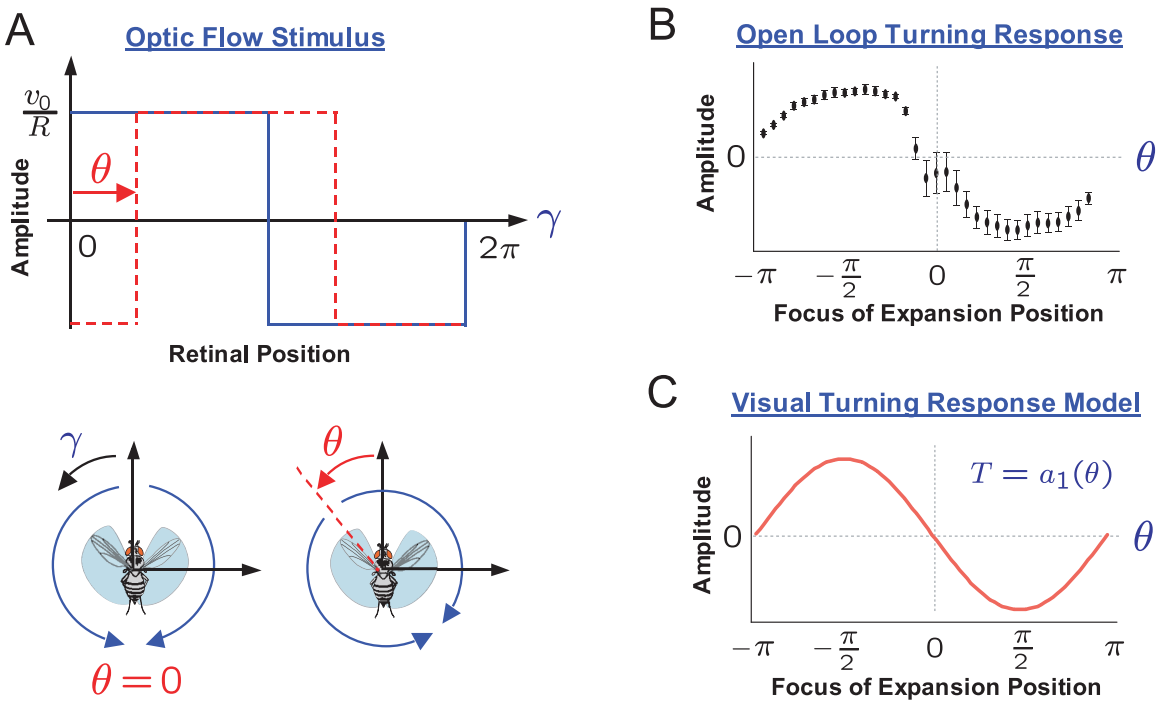

Figure 1.4: Open loop visuomotor reflexes in *Drosophila*. (A) Open loop visual stimulus pattern as a function of the retinal viewing angle γ. (B) Open loop response as a function of the position of the focus of expansion on the retina of tethered animals. The quantity plotted on the vertical axis is the difference between the right and left wing beat amplitudes measured by an optical sensor. (C) Open loop response of the visual turning model as a function of the focus of expansion position.

stimulus $\dot{Q}$ and the pattern sensitivity F, representing a left and right hemispherical pair of LPTCs, are 2π-periodic functions of the body-fixed retinal viewing angle γ. The open loop optic flow stimulus presented in the experiments of [64] depends on radius of the arena R, the magnitude of optic flow v_0/R, and the location of the focus of expansion on the retina θ (Figure 1.4A). Described as a spatial Fourier series expansion in terms of γ,

$$\dot{Q}(\gamma,\theta) = \frac{4v_0}{\pi R}\left(\sum_{n=1,3,5,\ldots}^{\infty}\frac{\cos n\theta}{n}\sin n\gamma - \sum_{n=1,3,5,\ldots}^{\infty}\frac{\sin n\theta}{n}\cos n\gamma\right), \tag{1.1}$$

with amplitudes of the cosine and sine spatial harmonics

$$\begin{aligned} a_n(\theta) &= \frac{1}{\pi}\int_0^{2\pi}\dot{Q}(\gamma,\theta)\cdot\cos n\gamma\, d\gamma = -\tfrac{4v_0}{\pi R n}\sin n\theta \\ b_n(\theta) &= \frac{1}{\pi}\int_0^{2\pi}\dot{Q}(\gamma,\theta)\cdot\sin n\gamma\, d\gamma = \tfrac{4v_0}{\pi R n}\cos n\theta. \end{aligned} \tag{1.2}$$

If we assume the following visuomotor control model for yaw torque

$$T(\theta) \quad = \quad \langle \dot{Q}(\gamma, \theta), F(\gamma) \rangle, \tag{1.3}$$

along with a LPTC motion pattern sensitivity

$$F(\gamma) \quad = \quad \cos \gamma, \tag{1.4}$$

then the open loop turning response is

$$T(\theta) \quad = \quad -\frac{4v_0}{\pi R} \sin \theta, \tag{1.5}$$

which corresponds to the first spatial harmonic of optic flow $a_1(\theta)$ from (1.2). Open loop turning response experiments were performed in [64], whose data is replotted in Figure 1.4B along with the open loop model response (1.5) in Figure 1.4C. The simple model of open loop visual response is shown to be in remarkable agreement with the behavioral data from the tethered *Drosophila*.

Based on these results, a closed loop planar insect flight model was constructed, with a control algorithm based on feedback of the location of the visual focus of contraction. The equations describing the dynamics and the actuation were based on current understanding of the biomechanics and aerodynamics [52], [21], and the optic flow was assumed planar and generated by a motion with respect to a homogeneous and uniform spatial distribution of objects in the environment. Under these assumptions, feasibility of visually mediated upwind orientation was demonstrated in the range of behaviorally relevant wind speeds (0.4 to 1.2 m/s).

1.5 Thesis Contributions and Organization

The experiments in [64] and modeling effort in [51] provide an initial step in the verification of the hypothesis that LPTCs extract global optic flow cues for use in navigation and stabilization, in contrast to more traditional suggestions that LPTCs might be used as direct estimators of kinematic states [18]. However, these efforts have assumed that the environment has a homogeneous and uniform spatial distribution of objects. In order to

generalize the conclusions to free flight behavior, as well as develop optic flow based methodologies for autonomous robotic guidance and navigation, we must relax the uniformity and homogeneity assumptions on the environment.

As will be shown in Chapter 2, there are two critical pieces of information available from retinal motion fields; body frame kinematics, useful for vehicle stabilization, and the spatial layout information of the environment, useful for guidance and navigation tasks. Experimental evidence suggests (Section 1.1) that LPTCs decompose complicated 2-D visual motion fields into approximately 120 separate outputs that are available to the motor control centers of the insect. In this thesis, a spatial inner product model for LPTCs is proposed and analyzed with an emphasis on extraction of behaviorally relevant optic flow cues. General retinal motion pattern sensitivities are assumed, and using the intuition from the corresponding decomposition, retinal sensitivity functions are constructed that provide stabilization of behaviors such as obstacle avoidance via a centering response, forward speed regulation, hover, and terrain following. The computationally efficient wide-field integration outputs require no direct estimation of depth or kinematic states, nor any prior knowledge of the environment. A general theory of planar optic flow based navigation and flight control is presented, demonstrating that the global optic flow cues extracted by LPTCs, which are generalized combinations of speed/depth, provide control-relevant information, as well as a novel methodology for utilizing optic flow sensory information in bio-inspired robotic applications.

In Chapter 2, a control-theoretic version of the equations that describe general spherical optic flow fields [41] for 3-D environments and 6 DOF dynamics is developed, which is required for a rigorous mathematical analysis of LPTC retinal motion processing. Specifically, the previous discretization of the environment into a finite number of rigid fiducial points [41] is replaced with a spatially continuous representation (that is, a representation that is a function of a set of continuous spatial independent variables) called the *nearness*, which is the inverse of the distances to the nearest objects along any direction from a general vantage point that is the center of a spherical retina. The rotational and translational contibutions to the retinal motion field are rewritten in a spherical coordinate-based linear operator formulation with the velocity dependence expressed in terms of quantities that are of interest for feedback control, namely the yaw, pitch, and roll rates for rotational velocity and forward, vertical, and sideslip translational velocities. Two special cases (horizontal

and vertical cross sections) of 1-D tangential optic flows corresponding to 3DOF planar motion are examined.

A model for wide-field integration of planar optic flow, corresponding to LPTC processing, is formalized in Chapter 3. It is shown that the set of all possible wide-field integration outputs is characterized by the spatial Fourier coefficients of the planar optic flows from Chapter 2. In addition, these Fourier coefficients are characterized in terms of the body frame linear and angular velocity and the spatial harmonics of the nearness function. Interpretations of these wide-field integration outputs for arbitrary environments are presented, which suggest a general methodology for stabilization of various navigational tasks. Essentially, by balancing various spatial harmonics of optic flow, we can obtain generalized feedback terms in relative units of speed/depth that are functions of rotational and lateral stiffness with respect to flight trajectories that avoid objects in the environment, as well as terms that contain rotational, lateral, and forward velocities, which are useful for closed loop stabilization and performance.

Obstacle avoidance and forward speed regulation is discussed in Chapter 4, with applications to planar wheeled robots and hovercraft. A static output feedback control structure is proposed, where force and torque inputs are computed (as would be the case with LPTCs) by taking the inner product of the instantaneous optic flow with pre-determined sensitivity functions for each required control input. Based on the analysis of the spatial Fourier decomposition of planar optic flows in Chapter 3, the connection between the retinal motion sensitivity function shape and its corresponding contributions to closed loop rotational and lateral stiffness and damping is formalized. Sensitivity function shape is then tied to behavior (closed loop eigenvalues) via a local asymptotic stability analysis. It is shown that the proposed methodology has sufficient complexity to give rise to the centering (obstacle avoidance) and clutter (forward speed regulation) responses exibited in experiments with insects, which were discussed in Section 1.3. Simulations of centering and forward speed regulation responses, as well as navigation of general environments, are presented.

In Chapter 5, wide-field integration outputs are coupled to pitch-altitude dynamics of rotorcraft. Using the same analytical approach as in Chapter 4, hovering and terrain following behaviors are stabilized. In this case, however, hover stabilization required a pitch (attitude) estimate as the rotational stiffness provided by forward motion is not available at the desired equilibrium point. Presumably this attitude estimate can be obtained by insects

from other sensory modalities, such as the visual-based ocelli [61]. As for the stabilization of the terrain following behavior, an absolute estimate of either forward velocity or altitude is required for zero steady-state error (a velocity estimate was assumed). This is due to the fact that wide-field integration outputs are derived from an optic flow field that is a relative speed/depth measurement. In the case of navigation between obstacles (centering response), the goal is to fly in between them so this problem is not encountered. Simulations of hovering and terrain following behaviors over general surfaces are presented.

Chapter 2

A Spatially Continuous Model of Optic Flow on the Sphere

Conceptually, the term *true optic flow* refers to the velocity field produced by motion of a projected image over the surface of the retina. This velocity field depends on the geometry of the retinal surface, the motion of the retinal vantage point, and the spatial distribution and motion of objects in the environment. Insects, who possess relatively simple visual systems, cannot measure this velocity field directly. However, they are able to compute estimates based on the spatiotemporal patterns of luminance values sensed by their compound eyes, which are large arrays of photoreceptors [4]. Moreover, the arrays of local movement detectors thought to perform the estimation, which are postsynaptic to the photoreceptors, depend on stimulus characteristics unrelated to motion. Hence, it is important to note the distinction between *true optic flow*, which is a purely geometric object, and what is more traditionally known as *optic flow*, the estimate provided by local motion detection that depends on structure, contrast, and spatial wavelength of retinal patterns [6], [26], [50].

In this thesis the idealized case of "true optic flow" will be considered, henceforth refered to as "optic flow," along with the assumption that the objects in the environment are fixed with respect to an inertial frame. The latter approximation is known as the *rigidity hypothesis*, described in [40]. The work presented will be restricted to a spherical retinal geometry; however the analysis approach adopted is completely general and can be applied to any assumed geometry.

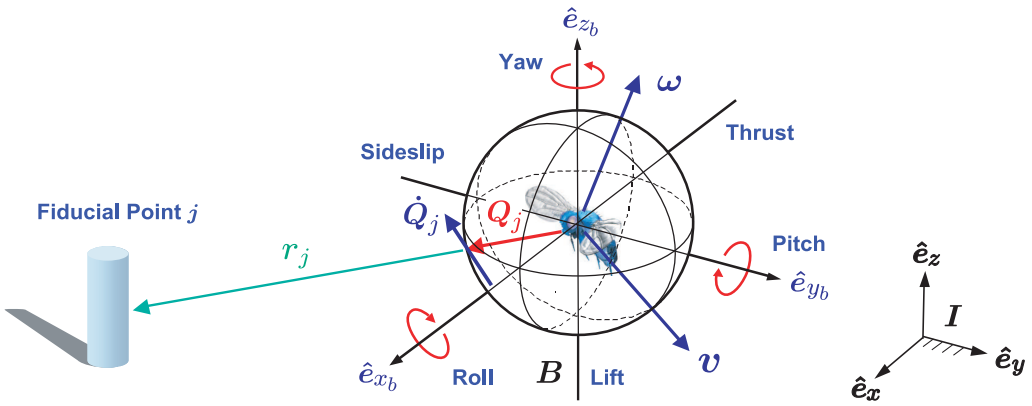

Figure 2.1: Optic flow field geometric definitions.

2.1 Review of Spatially Discrete Optic Flow

The basic set of equations that specify a general spatially discrete optic flow field for a spherical retinal surface geometry and an environment composed of $j = 1 \dots N$ rigid fiducial points (Figure 2.1) was developed in [41]:

$$\dot{\boldsymbol{Q}}_j \;=\; -\boldsymbol{\omega} \times \boldsymbol{Q}_j - \frac{1}{r_j}\left[\boldsymbol{v} - \langle \boldsymbol{v}, \boldsymbol{Q}_j \rangle \boldsymbol{Q}_j\right]. \tag{2.1}$$

A fiducial point j is located with respect to the vantage point, i.e., the origin of the rigidly attached body frame coordinate system $\boldsymbol{B} = (\hat{\boldsymbol{e}}_{x_b}, \hat{\boldsymbol{e}}_{y_b}, \hat{\boldsymbol{e}}_{z_b})$, by a vector $\boldsymbol{r}_j \in \mathbb{R}^3$ with magnitude $r_j = \|\boldsymbol{r}_j\|$ along marker $\boldsymbol{Q}_j = \boldsymbol{r}_j / r_j$. In this formulation, the motion parallax $\dot{\boldsymbol{Q}}_j = \dot{\boldsymbol{Q}}_{\boldsymbol{\omega},j} + \dot{\boldsymbol{Q}}_{\boldsymbol{v},j}$ is defined as the time derivative of the marker $\boldsymbol{Q}_j \in S^2$, which has contributions from both the angular and linear velocities $\boldsymbol{\omega}, \boldsymbol{v} \in \mathbb{R}^3$ of the body frame $\boldsymbol{B}$ with respect to an inertial frame $\boldsymbol{I} = (\hat{\boldsymbol{e}}_x, \hat{\boldsymbol{e}}_y, \hat{\boldsymbol{e}}_z)$. The rotational contribution,

$$\dot{\boldsymbol{Q}}_{\boldsymbol{\omega},j} \;=\; -\boldsymbol{\omega} \times \boldsymbol{Q}_j, \tag{2.2}$$

produces a velocity field independent of the distances to objects in the environment. The translational contribution,

$$\dot{\boldsymbol{Q}}_{\boldsymbol{v},j} \;=\; \frac{1}{r_j}\left[\boldsymbol{v} - \langle \boldsymbol{v}, \boldsymbol{Q}_j \rangle \boldsymbol{Q}_j\right], \tag{2.3}$$

is the relative linear velocity of the fiducial point, scaled inversely by the distance, with the radial component removed. Collectively, the set of markers and motion parallax vectors

$\{\boldsymbol{Q}_j, \dot{\boldsymbol{Q}}_j, j = 1 \ldots N\}$ compose a general spatially discrete optic flow field. However, we will use the terms *optic flow* and *motion parallax* synonymously.

2.2 Spatially Continuous Optic Flow

Equation (2.1) is a composition of two critical pieces of information: the vantage point motion, useful for the flight stabilization task, and the spatial distribution of objects in the environment, which is useful for navigation tasks such as obstacle avoidance and terrain following. As noted in Chapter 1, it is presumed that insect visual systems extract these types of control-relevant information by parsing the optic flow field via wide-field pattern sensitive neurons. A thorough and rigorous analysis of the information available from this sensory process from a system viewpoint will require a control-theoretic version of the 3-D optic flow field (2.1). In this section we develop a body-frame-relative spherical coordinate representation $\dot{\boldsymbol{Q}} = \dot{Q}_\gamma \, \hat{\boldsymbol{e}}_\gamma + \dot{Q}_\beta \, \hat{\boldsymbol{e}}_\beta$ with a continuous formulation of the spatial distribution of objects in the environment and kinematics $\boldsymbol{\omega}, \boldsymbol{v}$ expressed in body frame coordinates (Figure 2.2B).

For a continuous representation of the spatial distribution of the environment, the instantaneous set of distances to the fiducial points $\{r_i, i = 1 \ldots N\}$ becomes a function of the azimuth and elevation (Figure 2.2A) angles $r(\gamma, \beta) : [0, 2\pi] \times [-\frac{\pi}{2}, \frac{\pi}{2}] \mapsto (0, \infty)$. Implicit to this definition, r also depends on the particular environment as well as the vantage point configuration $\mathbf{q}(t)$, i.e., the position and orientation within that environment. We expect this function to take on values from $(0, \infty)$ and contain discontinuities, especially in a cluttered object field. By explicitly disallowing contact $r(\gamma, \beta, \mathbf{q}) = 0$, we ensure that the reciprocal, defined as the *nearness*,

$$\mu(\gamma, \beta, \mathbf{q}) \quad = \quad \frac{1}{r(\gamma, \beta, \mathbf{q})} \, , \tag{2.4}$$

is a bounded, piecewise continuous function with a finite (countable) number of discontinuities and at each instant in time is restricted to the space of square integrable functions

$$L_2\left([0, 2\pi] \times [0, \pi]\right) \quad = \quad \left\{ f : [0, 2\pi] \times [-\frac{\pi}{2}, \frac{\pi}{2}] \to \mathbb{R} : \int_0^{2\pi} \int_0^{\pi} |f(\gamma, \beta)|^2 \, d\gamma d\beta < \infty \right\}.$$

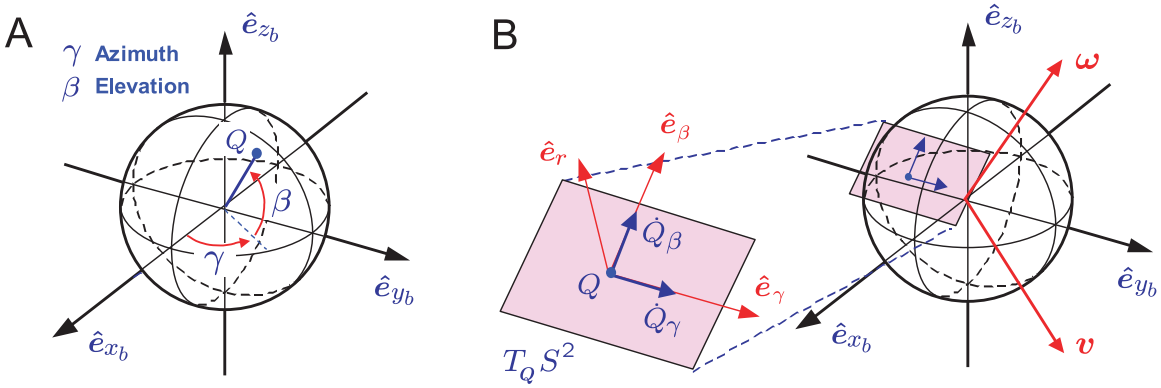

Figure 2.2: Spherical retinal geometry. (A) Azimuth and elevation angles (B) Spherical optic flow components $\dot{Q}_\gamma$ and $\dot{Q}_\beta$.

2.2.1 Rotational Optic Flow

We would like to express the optic flow in terms of quanities that are useful for feedback control; hence we define the roll, pitch, and yaw rates as the projections of the body frame angular velocity $\boldsymbol{\omega}$ onto the unit directions for $\boldsymbol{B}$,

$$\boldsymbol{\omega} \;=\; \dot{\psi}\,\hat{\boldsymbol{e}}_{x_b} + \dot{\phi}\,\hat{\boldsymbol{e}}_{y_b} + \dot{\theta}\,\hat{\boldsymbol{e}}_{z_b}. \tag{2.5}$$

For this spatially continuous formulation, we express a general point on the sphere $\boldsymbol{Q} \in S^2$ in terms of the azimuth γ and elevation β angles in $\boldsymbol{B}$ (Figure 2.2A):

$$\boldsymbol{Q}(\gamma,\beta) \;=\; \cos\gamma\cos\beta\,\hat{\boldsymbol{e}}_{x_b} + \sin\gamma\cos\beta\,\hat{\boldsymbol{e}}_{y_b} + \sin\beta\,\hat{\boldsymbol{e}}_{z_b}, \tag{2.6}$$

Now considered as an operator $\dot{\boldsymbol{Q}}_{\boldsymbol{\omega}} : \mathbb{R}^3 \mapsto \mathbb{R}^3$, the map $\boldsymbol{\omega} \mapsto -\boldsymbol{\omega} \times \boldsymbol{Q}$ is linear and has a skew-symmetric matrix representation

$$\hat{\boldsymbol{Q}}(\gamma,\beta) \;=\; \begin{pmatrix} 0 & -\sin\beta & \sin\gamma\cos\beta \\ \sin\beta & 0 & -\cos\gamma\cos\beta \\ -\sin\gamma\cos\beta & \cos\gamma\cos\beta & 0 \end{pmatrix}.$$

Hence, the rotational optic flow field in $\boldsymbol{B}$ coordinates is given by

$$\dot{\boldsymbol{Q}}_{\boldsymbol{\omega}} \;=\; \hat{\boldsymbol{Q}}\boldsymbol{\omega}. \tag{2.7}$$

2.2.2 Translational Optic Flow

As in the rotational contribution, we define the forward, lateral, and vertical velocities as projections of the body frame linear velocity $\boldsymbol{v}$ onto the unit directions for $\boldsymbol{B}$:

$$\boldsymbol{v} \;=\; \dot{x}_b\,\hat{\boldsymbol{e}}_{x_b} + \dot{y}_b\,\hat{\boldsymbol{e}}_{y_b} + \dot{z}_b\,\hat{\boldsymbol{e}}_{z_b}. \tag{2.8}$$

Using the definition (2.6), the operator $\boldsymbol{v} \mapsto \boldsymbol{v} - \langle \boldsymbol{v}, \boldsymbol{Q}\rangle \boldsymbol{Q}$ can be written compactly as

$$\left(I - \boldsymbol{Q}\boldsymbol{Q}^T\right)(\gamma,\beta) = \begin{pmatrix} 1-\cos^2\!\gamma\cos^2\!\beta & -\cos^2\!\beta\sin\gamma\cos\gamma & -\cos\gamma\sin\beta\cos\beta \\ -\cos\gamma\sin\gamma\cos\beta^2 & 1-\sin^2\!\gamma\cos^2\!\beta & -\sin\gamma\sin\beta\cos\beta \\ -\cos\gamma\sin\beta\cos\beta & -\sin\gamma\sin\beta\cos\beta & 1-\sin^2\!\beta \end{pmatrix}. \tag{2.9}$$

To obtain the translational optic flow field in $\boldsymbol{B}$ coordinates, we scale (2.9) by the nearness function (2.4):

$$\dot{\boldsymbol{Q}}_{\boldsymbol{v}} \;=\; \mu\left(I - \boldsymbol{Q}\boldsymbol{Q}^T\right)\boldsymbol{v}. \tag{2.10}$$

2.2.3 Spherical Coordinates

As noted in Section 2.1, the action of (2.10) is to extract the radial component from the velocity field of stationary objects relative to the moving body frame $\boldsymbol{B}$. Therefore, for an arbitrary point $\boldsymbol{Q}(\gamma,\beta) \in S^2$ on a spherical sensor or retina, the resulting translational optic flow vector is a projection of the relative velocity of the point on the nearest object along direction $\boldsymbol{Q}$ into the tangent space $T_{\boldsymbol{Q}}S^2$ at the point $\boldsymbol{Q}$, i.e.,

$$\left(I - \boldsymbol{Q}\boldsymbol{Q}^T\right) \;:\; \mathbb{R}^3 \mapsto TS^2. \tag{2.11}$$

The same result may be concluded regarding the action of (2.7):

$$\hat{\boldsymbol{Q}} \;:\; \mathbb{R}^3 \mapsto TS^2. \tag{2.12}$$

Therefore, it makes sense to put (2.7) and (2.10) into spherical coordinates, by applying the transformation from rectangular coordinates

$$R = \begin{pmatrix} \cos\gamma\cos\beta & \sin\gamma\cos\beta & \sin\beta \\ -\sin\gamma & \cos\gamma & 0 \\ -\cos\gamma\sin\beta & -\sin\gamma\sin\beta & \cos\beta \end{pmatrix}.$$

The resulting spherical coordinate representation $\dot{\boldsymbol{Q}} = \dot{Q}_\gamma\,\hat{\boldsymbol{e}}_\gamma + \dot{Q}_\beta\,\hat{\boldsymbol{e}}_\beta$ is given by

$$\dot{\boldsymbol{Q}} = A\boldsymbol{\omega} + \mu B\boldsymbol{v}. \tag{2.13}$$

The matricies $A(\gamma,\beta) = R\hat{\boldsymbol{Q}}$ and $B(\gamma,\beta) = -R\left(I - \boldsymbol{Q}\boldsymbol{Q}^T\right)$, reflecting the spherical retina geometry, are given by

$$A(\gamma,\beta) = \begin{pmatrix} \sin\beta\cos\gamma & \sin\beta\sin\gamma & -\cos\beta \\ \sin\gamma & \cos\gamma & 0 \end{pmatrix}$$

$$B(\gamma,\beta) = \begin{pmatrix} -\sin\gamma & \cos\gamma & 0 \\ -\sin\beta\cos\gamma & -\sin\beta\sin\gamma & \cos\beta \end{pmatrix}.$$

It is further assumed that the kinematics $\dot{\mathbf{q}} = (\boldsymbol{v},\boldsymbol{\omega})$ of the body frame $\boldsymbol{B}$ are bounded, piecewise-continuous functions of time; hence the instantaneous optic flow components $\dot{Q}_\gamma$ and $\dot{Q}_\beta$, given by (2.13), are restricted to the function space $L_2\left([0,2\pi]\times[-\frac{\pi}{2},\frac{\pi}{2}]\right)$.

2.3 Planar Optic Flow

For planar guidance and navigation applications where rigid body motion is restricted to 3 DOF (planar translation with single-axis rotation) we will consider two special cases of general spherical optic flows (2.13).

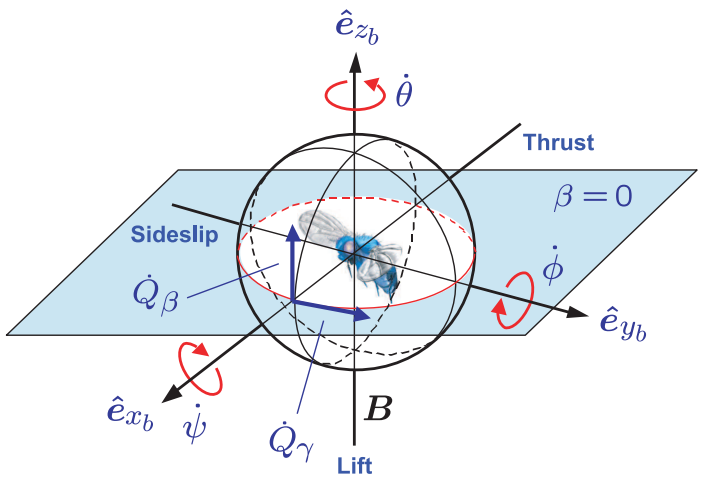

Figure 2.3: Horizontal cross-section optic flow definitions.

2.3.1 Horizontal Applications

The tangential and normal optic flow components $\dot{Q}_\gamma$ and $\dot{Q}_\beta$ for the circle defined by the intersection of S^2 and the plane $\beta = 0$ (Figure 2.3B) are given by

$$\dot{Q}_\gamma = -\dot{\theta} + \mu(\gamma, 0, \mathbf{q}) \, (\dot{x}_b \sin\gamma - \dot{y}_b \cos\gamma) \tag{2.14}$$

$$\dot{Q}_\beta = -\dot{\psi} \sin\gamma + \dot{\phi} \cos\gamma - \mu(\gamma, 0, \mathbf{q}) \, \dot{z}_b \tag{2.15}$$

For motion restricted to the plane $\beta = 0$, we define the vehicle configuration $\mathbf{q} = (x, y, \theta)$ and velocity $\dot{\mathbf{q}} = (\dot{x}_b, \dot{y}_b, \dot{\theta})$ with respect to an inertial (static) environment. Under these conditions, the normal component $\dot{Q}_\beta$ is zero, and the tangential component $\dot{Q}_\gamma$ becomes a 2π-periodic function of the vehicle-referred viewing angle γ. Clearly for fixed t, $\mu(\gamma, 0, \mathbf{q}) \in L_2[0, 2\pi]$ and therefore $\dot{Q}_\gamma \in L_2[0, 2\pi]$. For notational convenience we will refer to the planar nearness function for the environment of interest as $\mu(\gamma, \mathbf{q})$, noting the dependence on components of the configuration of the vehicle. In addition we will drop the γ subscript and refer to the tangential optic flow component as $\dot{Q}(\gamma, \mathbf{q}, \dot{\mathbf{q}})$, noting the dependence on the vehicle's configuration and velocity:

$$\dot{Q}(\gamma, \mathbf{q}, \dot{\mathbf{q}}) = -\dot{\theta} + \mu(\gamma, \mathbf{q}) \, (\dot{x}_b \sin\gamma - \dot{y}_b \cos\gamma) \, . \tag{2.16}$$

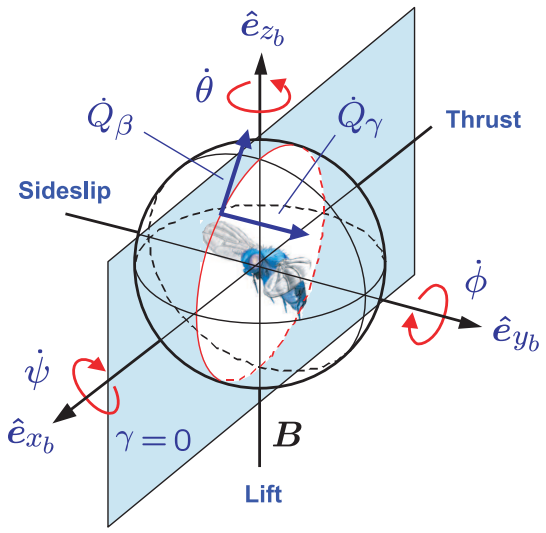

Figure 2.4: Vertical cross-section optic flow definitions.

2.3.2 Vertical Applications

The tangential and normal optic flow components $\dot{Q}_\gamma$ and $\dot{Q}_\beta$ for the circle defined by the intersection of S^2 and the plane $\gamma = 0$ (Figure 2.4) are given by

$$\dot{Q}_\gamma = \dot{\psi}\sin\beta - \dot{\theta}\cos\beta - \mu(0,\beta,\mathbf{q})\ \dot{y}_b \tag{2.17}$$

$$\dot{Q}_\beta = \dot{\phi} + \mu(0,\beta,\mathbf{q})\ (\dot{x}_b\sin\beta - \dot{z}_b\cos\beta) \tag{2.18}$$

For motion restricted to the plane $\gamma = 0$, we define the vehicle configuration $\mathbf{q} = (x, z, \phi)$ and velocity $\dot{\mathbf{q}} = (\dot{x}_b, \dot{z}_b, \dot{\phi})$ with respect to an inertial environment. We let β span the circle, i.e., $\beta \in [0, 2\pi]$, and for notational convienience redefine the sign convention of ϕ such that it agrees with that of the β coordinate. Under these conditions, the component normal to the circle $\dot{Q}_\gamma$ is zero, and the component tangent to the circle $\dot{Q}_\beta$ becomes a 2π-periodic function of the vehicle-referred viewing angle β. Clearly for fixed t, $\mu(0,\beta,\mathbf{q}) \in L_2[0, 2\pi]$ and therefore $\dot{Q}_\beta \in L_2[0, 2\pi]$. As in the horizontal case, we will refer to the planar nearness function for the environment of interest as $\mu(\beta, \mathbf{q})$, noting the dependence on components of the configuration of the vehicle. In addition we will drop the β subscript and refer to the tangential optic flow component as $\dot{Q}(\beta, \mathbf{q}, \dot{\mathbf{q}})$, noting the dependence on the vehicle's configuration and velocity:

$$\dot{Q}(\beta,\mathbf{q},\dot{\mathbf{q}}) = -\dot{\phi} + \mu(\beta,\mathbf{q})\,(\dot{x}_b\sin\beta - \dot{z}_b\cos\beta)\,. \tag{2.19}$$

Chapter 3

A Model for Wide-Field Integration of Optic Flow

3.1 Planar Optic Flow Processing Model

For this treatment we will represent the lobula plate tangential cells (or ispi- and contralateral pairs as may be appropriate) by a general weight $F_i(\gamma) \in L_2[0, 2\pi]$, which models their sensitivity to retinal motion patterns (Figure 3.1A). Weights $F_i(\gamma)$ are essentially a spatially distributed set static gains that are applied to the output at the corresponding local motion detectors at retinal azumuthal positions γ (Figure 3.1B). With the analysis presented in this chapter, we are interested in characterizing the available information relevant for use in closed loop feedback. We expect these retinal motion pattern sensitivities to be piecewise continuous and square-integrable; hence the restriction to the function space $L_2[0, 2\pi]$. For this analysis we will also assume that optic flow estimation processing (photoreceptors and local motion detectors) have negligible dynamics, that is, wide-field spatial integration (henceforth WFI) can be modeled in entirety by a transformation W, representing a spatial inner product over the circle S^1 with the optic flow kernel

$$\dot{Q}(\gamma, \mathbf{q}, \dot{\mathbf{q}}) \;\; = \;\; -\dot{\theta} + \mu(\gamma, \mathbf{q}) \; (\dot{x}_b \sin\gamma - \dot{y}_b \cos\gamma), \tag{3.1}$$

which acts on elements $F_i(\gamma)$ to produce a sensor output signal $z_i(\mathbf{q}, \dot{\mathbf{q}})$, hence

$$W : \; F_i \in L_2[0, 2\pi] \; \mapsto \; z_i \in \mathbb{R}.$$

The transformation W defined by $z_i = WF_i$ can be represented as a linear functional using the inner product structure available (A.0.2) on $L_2[0, 2\pi]$:

$$z_i(\mathbf{q}, \dot{\mathbf{q}}) \;=\; \langle \dot{Q}, F_i \rangle_w \;=\; \frac{1}{\pi} \int_0^{2\pi} \dot{Q}(\gamma, \mathbf{q}, \dot{\mathbf{q}}) \cdot F_i(\gamma)\, d\gamma. \tag{3.2}$$

The inner product (3.2) has been defined with a factor of $1/\pi$ to be compatible with the typical Fourier harmonic component definition so that later notation is simplified.

3.2 Characterization of WFI Outputs

We are interested in characterizing the set of all possible sensory outputs available within this model and their dependency on vehicle motion and spatial distribution of objects in the environment. Since $L_2[0, 2\pi]$ is a separable Hilbert space, per (A.0.1) a countably infinite orthonormal basis $\{\phi_n(\gamma)\}$ exists. For every instant in time, the optic flow (3.1) resides in $L_2[0, 2\pi]$; therefore also by (A.0.1) we are guaranteed a unique generalized Fourier series expansion

$$\dot{Q} \;=\; \sum_n \langle \dot{Q}, \phi_n \rangle \; \phi_n.$$

For the orthonormal basis (A.0.2)

$$\Phi \;=\; \{1/\sqrt{2}\} \cup \{\cos n\gamma : n \in \mathbb{Z}^+\} \cup \{\sin n\gamma : n \in \mathbb{Z}^+\}, \tag{3.3}$$

the expansion becomes

$$\dot{Q} \;=\; \frac{a_0}{2} + \sum_{n=1}^{\infty} a_n \cos n\gamma + \sum_{n=1}^{\infty} b_n \sin n\gamma,$$

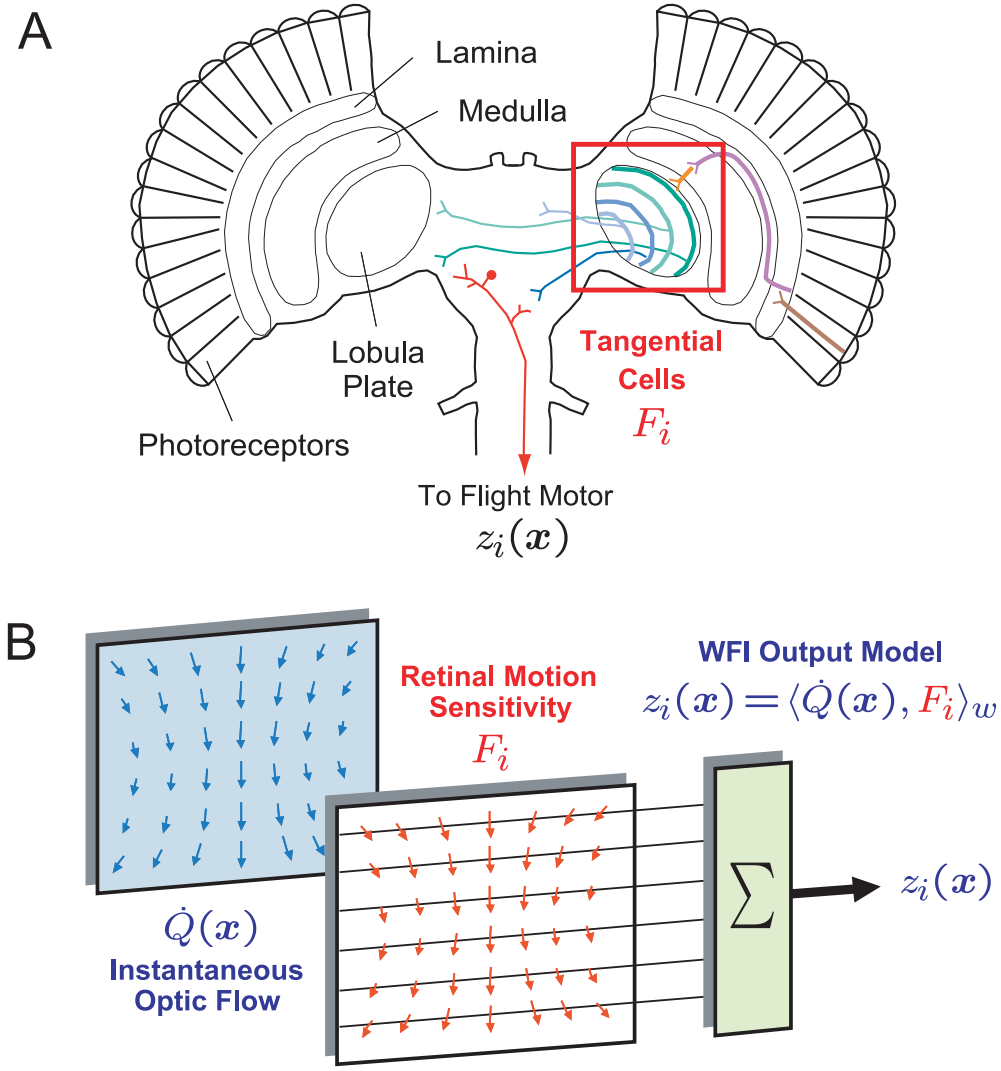

Figure 3.1: (A) Visuomotor system of insects. Wide-field retinal motion sensitive interneurons (tangential cells) parse spatially-preserved visual information and transmit it to motor control centers. (B) WFI processing model. Spatial modes $z_i(\boldsymbol{x})$ of optic flow are extracted by retinal motion sensitivity kernels F_i.

where the Fourier coefficients of the optic flow, which are functions of the configuration and velocity, are defined as

$$\begin{aligned} a_0(\mathbf{q},\dot{\mathbf{q}}) &= \langle \dot{Q}, 1/\sqrt{2}\rangle_w &= \frac{1}{\pi}\int_0^{2\pi} \dot{Q}(\gamma,\mathbf{q},\dot{\mathbf{q}})/\sqrt{2}\; d\gamma \\ a_n(\mathbf{q},\dot{\mathbf{q}}) &= \langle \dot{Q}, \cos n\gamma\rangle_w &= \frac{1}{\pi}\int_0^{2\pi} \dot{Q}(\gamma,\mathbf{q},\dot{\mathbf{q}})\cdot\cos n\gamma\; d\gamma \\ b_n(\mathbf{q},\dot{\mathbf{q}}) &= \langle \dot{Q}, \sin n\gamma\rangle_w &= \frac{1}{\pi}\int_0^{2\pi} \dot{Q}(\gamma,\mathbf{q},\dot{\mathbf{q}})\cdot\sin n\gamma\; d\gamma. \end{aligned}$$

With some manipulations, we can re-write these expressions in terms of the vehicle velocity $\dot{\mathbf{q}} = (\dot{x}_b, \dot{y}_b, \dot{\theta})$ and the spatial harmonics $\{A_0(\mathbf{q}), A_k(\mathbf{q}), B_k(\mathbf{q}) : k \in \mathbb{Z}^+\}$ of the nearness function $\mu(\gamma,\mathbf{q})$:

$$\begin{aligned} a_0 &= (-\dot{\theta} + \dot{x}_b B_1 - \dot{y}_b A_1/\sqrt{2} \\ a_n &= \frac{\dot{x}_b}{2}\left(-B_{n-1} + B_{n+1}\right) - \frac{\dot{y}_b}{2}\left(A_{n-1} + A_{n+1}\right) \\ b_n &= \frac{\dot{x}_b}{2}\left(A_{n-1} - A_{n+1}\right) - \frac{\dot{y}_b}{2}\left(B_{n-1} + B_{n+1}\right), \end{aligned} \tag{3.4}$$

where the nearness function has been expanded in the orthonormal basis Φ:

$$\mu = \frac{A_0}{2} + \sum_{k=1}^{\infty} A_k \cos n\gamma + \sum_{k=1}^{\infty} B_k \sin n\gamma,$$

and whose configuration-dependent Fourier series coefficients are defined as

$$\begin{aligned} A_0(\mathbf{q}) &= \langle \mu, 1/\sqrt{2}\rangle_w &= \frac{1}{\pi}\int_0^{2\pi} \mu(\gamma,\mathbf{q})/\sqrt{2}\; d\gamma \\ A_k(\mathbf{q}) &= \langle \mu, \cos k\gamma\rangle_w &= \frac{1}{\pi}\int_0^{2\pi} \mu(\gamma,\mathbf{q})\cdot\cos k\gamma\; d\gamma \\ B_k(\mathbf{q}) &= \langle \mu, \sin k\gamma\rangle_w &= \frac{1}{\pi}\int_0^{2\pi} \mu(\gamma,\mathbf{q})\cdot\sin k\gamma\; d\gamma. \end{aligned}$$

Now, under the interpretation

$$W\Phi = \{a_0\} \cup \{a_n : n \in \mathbb{Z}^+\} \cup \{b_n : n \in \mathbb{Z}^+\},$$

the equations (3.4) define the action of the linear transformation $W : L_2[0, 2\pi] \mapsto \mathbb{R}$ on a basis Φ for the domain, and as such uniquely characterize the set of all possible wide-field

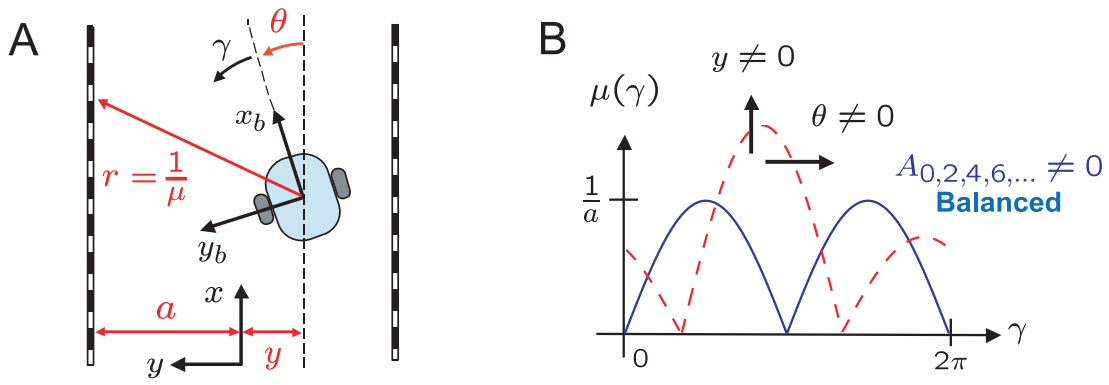

Figure 3.2: Planar tunnel geometry. (A) Notation and vehicle configuration definitions (B) Balanced planar nearness function $\mu(\gamma)$ and lateral/rotational perturbations of μ.

integration sensory outputs.

3.3 Interpretation of WFI Outputs

The relationships in (3.4) define how WFI outputs depend on vehicle velocity $\dot{\mathbf{q}} = (\dot{x}_b, \dot{y}_b, \dot{\theta})$ and object nearness $\mu : \{A_0, A_k, B_k : k \in \mathbb{Z}^+\}$ with respect to the vantage point configuration $\mathbf{q}$; however the intuition required to utilize them in closed loop feedback is not readily apparent. In the following we consider several motivational examples that suggest a general methodology for stabilization of various reflexive behaviors.

3.3.1 Planar Tunnel Geometry

As a first example, we consider a planar tunnel geometry (Figure 3.2A), which provides a reasonable approximation to flight between two obstacles. In this case the nearness function $\mu(\gamma, \mathbf{q})$ is independent of the axial position x and can be expressed in closed form as a function of the lateral position y, body frame orientation θ, and the tunnel half-width a:

$$\mu(\gamma, \mathbf{q}) \quad = \quad \begin{cases} \frac{\sin(\gamma+\theta)}{a-y} & 0 \leq \gamma + \theta < \pi \\ -\frac{\sin(\gamma+\theta)}{a+y} & \pi \leq \gamma + \theta < 2\pi \end{cases} . \tag{3.5}$$

Table 3.1: Planar Tunnel Spatial Fourier Decomposition

Mode	Balanced	Perturbed	Linearized $\bar{A}_k, \bar{B}_k$	Interpretation
A_0	$\frac{2}{\pi a}$	$\frac{2a}{\pi(a^2-y^2)}$	$\frac{2}{\pi a}$	Balanced
A_1	0	$\frac{y\sin\theta}{(a^2-y^2)}$	0	-
B_1	0	$\frac{y\cos\theta}{(a^2-y^2)}$	$\frac{y}{a^2}$	Lateral Displacement
$A_{2,4,\ldots}$	$-\frac{4}{\pi a(k^2-1)}$	$-\frac{4a\cos k\theta}{\pi(a^2-y^2)(k^2-1)}$	$-\frac{4}{\pi a(k^2-1)}$	Balanced
$B_{2,4,\ldots}$	0	$-\frac{4a\sin k\theta}{\pi(a^2-y^2)(k^2-1)}$	$-\frac{4k\theta}{\pi a(k^2-1)}$	Rotary Displacement
$A_{3,5,\ldots}$	0	0	0	-
$B_{3,5,\ldots}$	0	0	0	-

For a perfectly centered vehicle $(y, \theta) = (0, 0)$, (3.5) reduces to $|\sin\gamma|/a$, which has a Fourier series expansion

$$\mu(\gamma, \mathbf{q})|_{y,\theta=0} = \frac{2}{a\pi} - \sum_{k=2,4,6,\ldots}^{\infty} \frac{4}{a\pi(k^2-1)} \cos k\gamma. \tag{3.6}$$

Note that the expansion is composed of a DC component and even cosine harmonics $\{A_k : k = 0, 2, 4, \ldots\}$ of decreasing amplitude only. Equation (3.6) represents the *balanced* or *equilibrium* nearness shape (Figure 3.2B), as it corresponds to a position and orientation along the centerline of the tunnel. For lateral and rotary displacements, the spatial harmonics of the perturbed nearness function are computed in Table 3.1. Also shown are their linearizations

$$\begin{aligned} \bar{A}_k(\mathbf{q}) &= A_k(\mathbf{q}_0) + \sum_i \frac{\partial A_k}{\partial q_i}(\mathbf{q}_0) \cdot (q_i - q_{0i}) \\ \bar{B}_k(\mathbf{q}) &= B_k(\mathbf{q}_0) + \sum_i \frac{\partial B_k}{\partial q_i}(\mathbf{q}_0) \cdot (q_i - q_{0i}), \end{aligned} \tag{3.7}$$

with respect to the configuration variables $\mathbf{q} = (y, \theta)$ at a reference configuration $\mathbf{q}_0 = (0, 0)$. From these linearizations it is clear that the B_1 harmonic provides an estimate of the lateral displacement (Figure 3.3A) while the B_2 harmonic provides an estimate of the rotary displacement (Figure 3.3B).

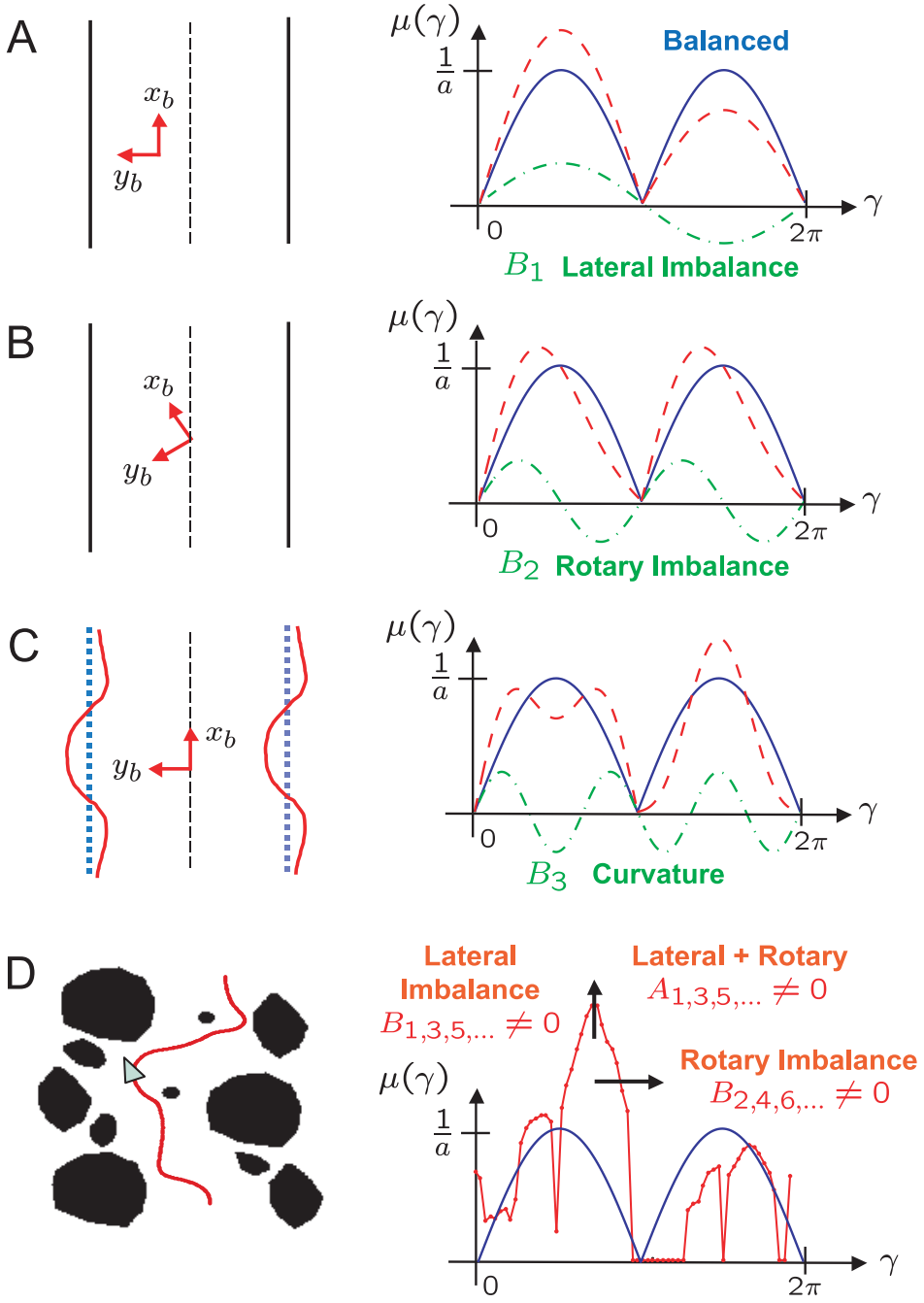

Figure 3.3: Connections between WFI outputs and spatial structure of μ. (A) The B_1 harmonic corresponds to a lateral displacement. (B) The B_2 harmonic is a leading order estimate of the rotation. (C) The B_3 harmonic represents local curvature. (D) μ perturbations in environments with higher order spatial structure; odd B_k correspond to a lateral imbalance, even B_k correspond to a rotary imbalance, and odd A_k appear when there is a coupled lateral/rotary imbalance.

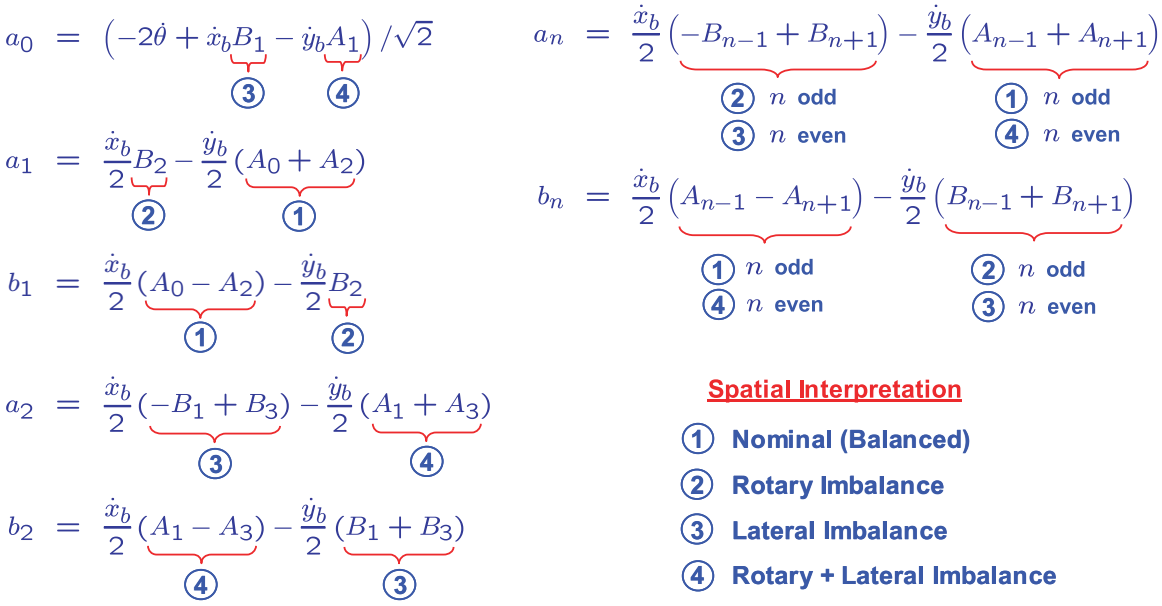

Figure 3.4: Spatial interpretation of horizontal WFI outputs. Nearness function spatial harmonics $\{A_0, A_k, B_k, k \in \mathbb{Z}^+\}$ appear in one of four spatially significant combinations.

These results can immediately be generalized to environments with more complicated spatial structure (Figures 3.3 C,D). Spatial harmonics of the nearness function appear in one of four spatially significant combinations whose interpretation is shown in Figure 3.4. We have defined even cosine harmonics $\{A_k : k = 0, 2, 4, \ldots\}$ to represent a balanced nearness function; thus, the presence of even sine harmonics $\{B_k : k = 2, 4, \ldots\}$ indicates a rotary imbalance, odd sine harmonics $\{B_k : k = 1, 3, 5, \ldots\}$ a lateral imbalance, and odd cosine harmonics $\{A_k : k = 1, 3, 5, \ldots\}$ a coupled rotary/lateral imbalance.

3.3.2 Planar Surface Geometry

The planar surface geometry (Figure 3.5A) serves as a second motivating example; the nearness function $\mu(\beta, \mathbf{q})$ is independent of the lateral position along the surface and can be expressed in closed form as a function of the reference height h, body frame pitch orientation ϕ, and the vertical height z above the reference:

$$\mu(\beta, \mathbf{q}) = \begin{cases} 0 & 0 \leq \beta + \phi < \pi \\ -\frac{\sin(\beta+\phi)}{z+h} & \pi \leq \beta + \phi < 2\pi \end{cases}. \tag{3.8}$$

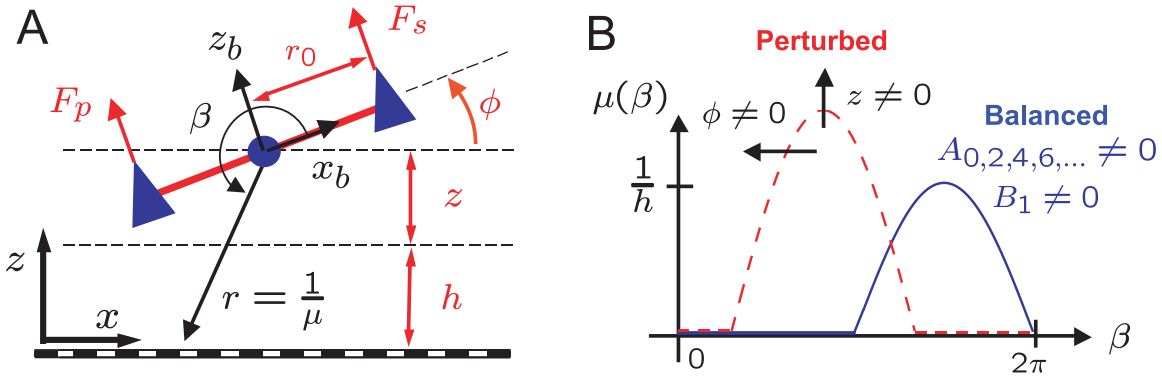

Figure 3.5: Planar surface geometry. (A) Rotorcraft geometry and kinematic definitions. (B) Balanced planar nearness function $\mu(\beta)$ with altitude and pitch perturbations.

For the case $z = 0$ and $\phi = 0$, (3.8) has a Fourier series expansion

$$\mu|_{z=0,\Phi=0} \quad = \quad \frac{2}{\pi h} - \frac{1}{2h}\sin\beta - \sum_{k=2,4,6,\ldots}^{\infty} \frac{2}{\pi h(k^2-1)}\cos k\beta. \tag{3.9}$$

Note that the expansion is composed of the fundamental sine harmonic B_1, a DC component and even cosine harmonics $\{A_k : k = 0, 2, 4, \ldots\}$ of decreasing amplitude. In this case, (3.9) represents the *balanced* or *equilibrium* nearness shape (Figure 3.5B), as it corresponds to level ($\phi = 0$) flight over a plane at the reference height h, i.e., $z = 0$.

The Fourier series for general rotary and altitude perturbations ($\phi \neq 0, z \neq 0$) from this equilibrium configuration can also be computed, and the terms are shown in Table 3.2. For rotary perturbations $\phi \neq 0$ we see that new spatial harmonics appear, specifically the fundamental cosine harmonic A_1, in proportion to $\sin\phi$, along with even sine harmonics $\{B_k : k = 0, 2, 4, \ldots\}$, in proportion to $\sin k\phi$. The amplitudes of the nominal harmonics present in the balanced nearness shape (3.9) are also influenced for $\phi \neq 0$ as they appear in proportion to $\cos k\phi$. Altitude perturbations $z \neq 0$ have the effect of scaling the amplitudes of all the harmonics present by $h/(z+h)$. Also shown in Table 3.2 are the linearizations with respect to the configuration variables $\mathbf{q} = (z, \phi)$ at a reference configuration $\mathbf{q}_0 = (0, 0)$. Clearly the A_1 and $\{B_k : k = 0, 2, 4, \ldots\}$ harmonics provide an estimate of the pitch displacement, while the amplitudes of B_1 and $\{A_k : k = 0, 2, 4, \ldots\}$ provide a relative altitude estimate.

Table 3.2: Planar Surface Spatial Fourier Decomposition

Mode	Balanced	Perturbed	Linearized $\bar{A}_k, \bar{B}_k$	Interpretation
A_0	$\frac{2}{\pi h}$	$\frac{2}{\pi(z+h)}$	$\frac{2}{\pi h}\left(1-\frac{z}{h}\right)$	Altitude Displacement
A_1	0	$-\frac{\sin\phi}{2(z+h)}$	$\frac{1}{2h}\phi$	Pitch Displacement
B_1	$-\frac{1}{2h}$	$-\frac{\cos\phi}{2(z+h)}$	$-\frac{1}{2h}\left(1-\frac{z}{h}\right)$	Altitude Displacement
$A_{2,4,6,...}$	$-\frac{2}{\pi h(k^2-1)}$	$-\frac{2\cos k\phi}{\pi(z+h)(k^2-1)}$	$-\frac{2}{\pi h(k^2-1)}\left(1-\frac{z}{h}\right)$	Altitude Displacement
$B_{2,4,6,...}$	0	$\frac{2\sin k\phi}{\pi(z+h)(k^2-1)}$	$\frac{2k\phi}{\pi h(k^2-1)}$	Pitch Displacement
$A_{3,5,7,...}$	0	0	-	-
$B_{3,5,7,...}$	0	0	-	-

Chapter 4

Obstacle Avoidance and Forward Speed Regulation

4.1 WFI-Based Static Output Feedback

If we were to write down a simple block diagram for planar vehicle implementation based on the various connections within the visuomotor system of the fly, it might look something like Figure 4.1. The *plant dynamics* block, described by the set of nonlinear differential equations $\dot{x} = f(x, u)$, $f \in \mathbb{R}^n$, takes force and torque inputs $u(t) \in \mathbb{R}^p$ and outputs the state of the vehicle $x(t) \in \mathbb{R}^n$. The *optic flow estimation* block takes as inputs the state $x = (\mathbf{q}, \dot{\mathbf{q}})$ and the spatial nearness $\mu(\gamma, \mathbf{q}) \in L_2[0, 2\pi]$ and outputs the instantaneous optic flow $\dot{Q}(\gamma, \mathbf{q}, \dot{\mathbf{q}}) \in L_2[0, 2\pi]$. In the insect visual system this is thought to be accomplished with photoreceptors and arrays of elementary (local) motion detectors [15], whereas in a robotic application this function may be performed in a number of ways, for example, by image interpolation algorithms based on camera image inputs [57]. The *wide field integration* block(s), which model the LPTC spatial decompositions of the optic flow kernel input $\dot{Q}$ through pre-determined sensitivity functions $F_{u_i}(\gamma) \in L_2[0, 2\pi]$, produce the requisite force and torque inputs, which are fed back to the dynamics. Insects implement this function via wide-field sensitive neurons, contained in the lobula plate (Figure 3.1), which parse the spatially preserved motion estimates from the earlier stages of the vision system. In robotic applications, this function can be implemented easily as long as a minimum of computation ability is available.

The advantages of the block diagram in Figure 4.1 are that it is simple to implement in robotic navigation applications, along with the fact that it requires very little computation

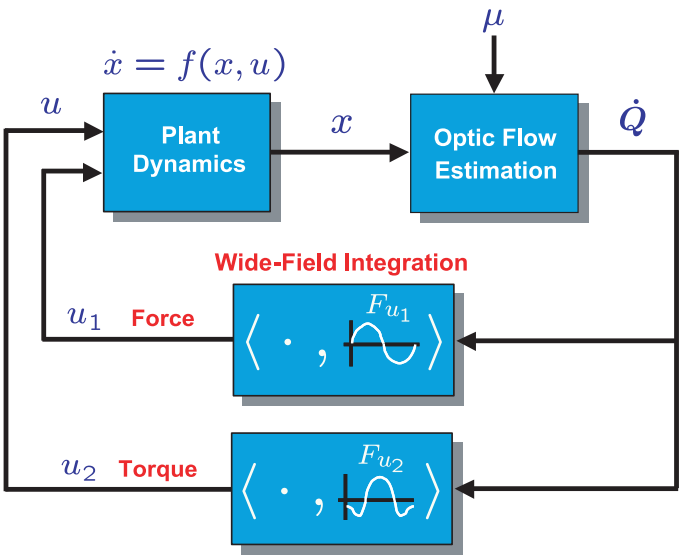

Figure 4.1: Basic closed loop block diagram for static output feedback of wide-field integration processing information.

time (hence only very minor servo delay). Given an instantaneous optic flow estimate, one just needs to perform a spatial inner product with pre-determined sensitivity patterns to compute each force and torque control input desired,

$$u_i \quad = \quad \langle \dot{Q}, F_{u_i} \rangle_w. \tag{4.1}$$

This speed and simplicity are greatly desired from the point of view of closing visual-based control loops where significant bandwidth is required, as in the case with the fast, highly-agile dynamics of MAVs.

Figure 4.1 represents a system level representation of the insect visuomotor system as well as a simple implementation for robotic applications. However, as formulated it does not lend any particular insight into how to design retinal motion sensitivity functions $F_{u_i}(\gamma)$ to accomplish navigation and control tasks. For that insight, we look to the block diagram representation in Figure 4.2. In this case, the plant dynamics and optic flow estimation blocks remain unchanged, and the wide-field integration block is represented functionally as a *decomposition* or a *projection* of the optic flow $\dot{Q}$ onto a set of basis functions $\{\phi_n(\gamma)\}$:

$$\dot{Q}(\gamma, \mathbf{q}, \dot{\mathbf{q}}) \quad = \quad \sum_n^{\infty} c_n(\mathbf{q}, \dot{\mathbf{q}}) \cdot \phi_n(\gamma), \tag{4.2}$$

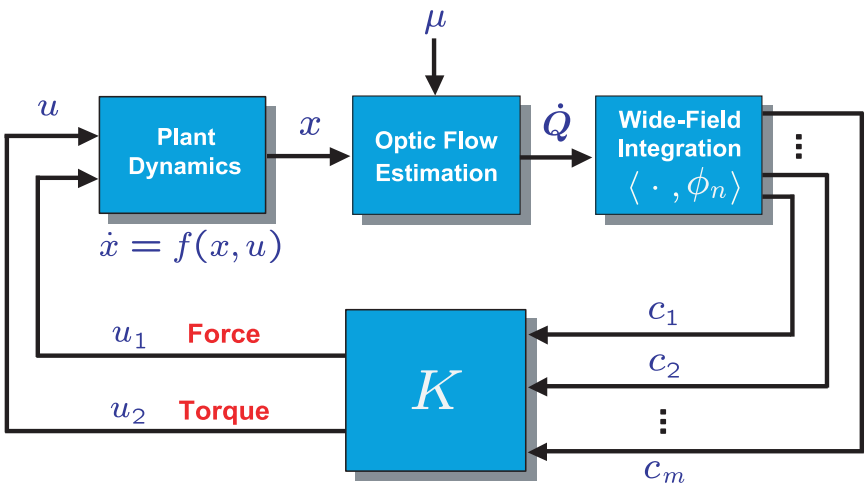

Figure 4.2: Control-theoretic representation of static output feedback of WFI information. The WFI operator acts to decompose the optic flow into projections c_n onto a finite set of basis functions ϕ_n.

where the projections are defined as

$$c_n(\mathbf{q}, \dot{\mathbf{q}}) \quad = \quad \langle \dot{Q}(\gamma, \mathbf{q}, \dot{\mathbf{q}}), \phi_n(\gamma) \rangle. \tag{4.3}$$

The advantage to thinking of wide-field integration as a decomposition of optic flow is that it provides a basis $\{c_n\}$ of possible output feedback terms that are, assuming the basis $\{\phi_n(\gamma)\}$ is wisely chosen, relatively simple functions of the quantities of interest $(\mathbf{q}, \dot{\mathbf{q}})$ for navigation and control. For instance, a particular decomposition might provide terms that uncouple lateral and rotational stiffness or damping. Hence, with selection of gains $\mathbf{K} \in \mathbb{R}^{p \times m}$, where m is the number of basis functions used for decomposition, we can intelligently feed back commands to force and torque inputs in such a way to stabilize various reflexive behaviors:

$$u_i \quad = \quad \sum_{j=1}^{m} K_{ij} \, c_j. \tag{4.4}$$

The block diagrams in Figure 4.1 and Figure 4.2 are completely mathematically equivalent. Therefore, once we have designed the gains $\mathbf{K} = [K_{ij}]$, we can immediately write down the corresponding motion sensitivity functions

$$F_{u_i}(\gamma) \quad = \quad \sum_{j=1}^{m} K_{ij} \, \phi_j(\gamma), \tag{4.5}$$

that upon taking the spatial inner product with the optic flow $\dot{Q}$, compute the appropriate controlled inputs (4.1).

If an orthonormal basis of sinusoids (3.3) is used to decompose the optic flow into spatial harmonics (3.4), the force and torque control inputs u_1, u_2 can be computed as static combinations

$$u_i \quad = \quad K^a_{i0}\, a_0 + \sum_{j=1}^{m} K^a_{ij}\, a_j + \sum_{j=1}^{m} K^b_{ij}\, b_j, \tag{4.6}$$

which correspond to motion sensitivity functions

$$F_{u_i} \quad = \quad K^a_{i0} + \sum_{j=1}^{m} K^a_{ij} \cos j\gamma + \sum_{j=1}^{m} K^b_{ij} \sin j\gamma. \tag{4.7}$$

4.2 Wheeled Robot Control

In this section we demonstrate the utility of WFI sensory outputs (3.4) through coupling with planar wheeled robot dynamics via static output feedback (Figure 4.1) in order to stabilize obstacle avoidance (centering) and forward speed regulation (clutter) reflexive behaviors. We will consider rolling or wheeled vehicles of the unicycle type (Figure 4.3), subject to the nonholonomic constraint

$$\dot{x} \sin\theta - \dot{y} \cos\theta \quad = \quad 0. \tag{4.8}$$

This assumption enforces the zero sideslip condition $\dot{y}_b = 0$, resulting in a simplified optic flow field

$$\dot{Q}(\gamma, \mathbf{q}, \dot{\mathbf{q}}) \quad = \quad -\dot{\theta} + \mu(\gamma, \mathbf{q}) \cdot \dot{x}_b \sin\gamma. \tag{4.9}$$

It is assumed that the two wheels providing continuous contact with the ground are driven independently, and the vehicle center of mass is located at the midpoint along the axis between them. For the inertial configuration $\mathbf{q} = (x, y, \theta)$ the kinematic and dynamic

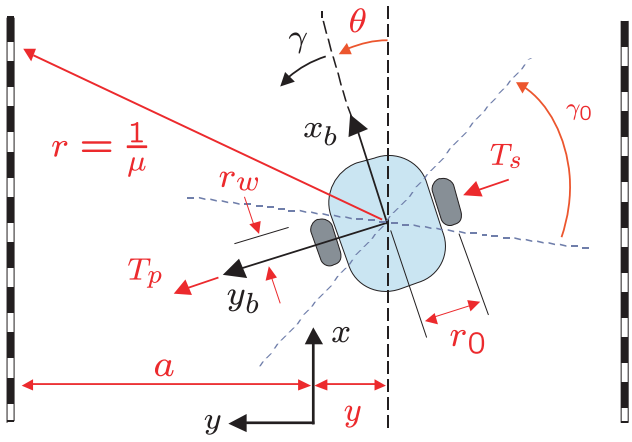

Figure 4.3: Wheeled robot geometry and kinematics.

equations describing the motion are

$$\begin{aligned} \dot{x} &= v\cos\theta \\ \dot{y} &= v\sin\theta \\ m\dot{v} &= \frac{1}{r_w}(T_s + T_p) \\ J\ddot{\theta} &= \frac{r_0}{r_w}(T_s - T_p)\,, \end{aligned} \tag{4.10}$$

where $v = \dot{x}_b$, starboard and port wheel torques are denoted by T_s and T_p, r_0 and r_w denote the vehicle width and wheel radius, and the vehicle mass and rotational inertia are given by m and J (Figure 4.3).

4.2.1 Navigation Methodology for General Environments

In this section we consider the interpretation of WFI static feedback in the context of the output regulation problem, that is, regulating or shaping the spatial harmonic content of the nearness μ. Recall the balanced nearness function (3.6) for the infinite tunnel, which was composed of DC and even (negative) cosine harmonics $\{A_k, k = 0, 2, 4, \ldots\}$. In the case of a more general obstacle field, we can choose this as our desired μ shape, and through feedback of WFI outputs we can filter out unwanted spatial content. The fundamental sine harmonic of the 1-D motion parallax field,

$$b_1 = \frac{\dot{x}_b}{2}(A_0 - A_2),$$

is proportional to the desired spatial content; therefore if we are close to the desired nearness shape, b_1 provides an estimate of the forward speed $\dot{x}_b$ and can be used to maintain a predetermined reference value. The speed setpoint is automatically reduced as the magnitudes of A_0 and A_2 increase, i.e., as the obstacle field becomes increasingly cluttered [36].

The DC and first two cosine harmonics of the motion parallax field,

$$\begin{aligned} a_0 &= -\sqrt{2}\dot{\theta} + \frac{\dot{x}_b}{\sqrt{2}} B_1 \\ a_1 &= \frac{\dot{x}_b}{2} B_2 \\ a_2 &= \frac{\dot{x}_b}{2}(-B_1 + B_3), \end{aligned}$$

are functions of even and odd sine harmonics B_k of the nearness function. Therefore, balancing (zeroing) the a_1 component contributes rotary stiffness to the loop and balancing the a_2 component contributes lateral stiffness (Figures 3.3A,B) for a control system that is regulating about a fixed forward speed $\dot{x}_b$. In addition, balancing the DC component adds rotary damping to the loop.

4.2.2 Local Asymptotic Stability Analysis

In this section feasibility of the proposed output feedback methodology will be evaluated though a linearized control design that guarentees local asymptotic stability of speed regulation and obstacle avoidance responses in the nonlinear system. To simplify notation we introduce the state definition $v = \dot{x}_b$ and input definitions

$$\begin{aligned} u_1 &= \frac{1}{m r_w}(T_s + T_p) \\ u_2 &= \frac{r_0}{J r_w}(T_s - T_p). \end{aligned} \tag{4.11}$$

Assuming small states (other than v) and control inputs, the linearized equations of motion for a centerline flight trajectory become

$$\begin{aligned} \dot{v} &= u_1 \\ \dot{y} &= v_0 \theta \\ \ddot{\theta} &= u_2. \end{aligned} \tag{4.12}$$

Table 4.1: Spatial Fourier Decomposition of Planar Tunnel Optic Flow for Vehicles with a Nonholonomic Sideslip Constraint

Mode	Tunnel Geometry	Linearization ($\boldsymbol{x}_0$)
a_0	$-\sqrt{2}\dot{\theta} + \frac{y}{\sqrt{2}(a^2-y^2)}\ \dot{x}_b \cos\theta$	$-\sqrt{2}\dot{\theta} + \frac{v_0}{\sqrt{2}a^2}\ y$
a_1	$\frac{4a}{3\pi(a^2-y^2)}\ \dot{x}_b \sin\theta\cos\theta$	$\frac{4v_0}{3\pi a}\ \theta$
b_1	$\frac{4a}{3\pi(a^2-y^2)}\ \dot{x}_b(\cos^2\theta + 1)$	$\frac{8}{3\pi a}\ \dot{x}_b$
a_2	$-\frac{y}{2(a^2-y^2)}\ \dot{x}_b \cos\theta$	$-\frac{v_0}{2a^2}\ y$
b_2	$\frac{y}{2(a^2-y^2)}\ \dot{x}_b \sin\theta$	0
a_n, $n = 1, 3, \ldots$	$\frac{4a}{n\pi(a^2-y^2)(n^2-4)}\ (n\sin\theta\cos n\theta - 2\cos\theta\sin n\theta)\ \dot{x}_b$	$-\frac{4v_0}{\pi a(n^2-4)}\ \theta$
a_n, $n = 2, 4, \ldots$	0	0
b_n, $n = 1, 3, \ldots$	$-\frac{4a}{n\pi(a^2-y^2)(n^2-4)}\ (n\sin\theta\sin n\theta + 2\cos\theta\cos n\theta)\ \dot{x}_b$	$-\frac{8}{n\pi a(n^2-4)}\dot{x}_b$
b_n, $n = 2, 4, \ldots$	0	0

We will first examine the task of maintaining a forward reference velocity and trajectory along the centerline of a tunnel. If we assume a nearness function (3.5) describing the planar tunnel geometry (Figure 3.2), we can explicitly compute the spatial Fourier harmonics of optic flow, as shown in the first column of Table 4.1. The second column is the resulting linearization

$$z(\boldsymbol{x}) \quad = \quad z(\boldsymbol{x}_0) + \sum_i \frac{\partial z}{\partial x_i}(\boldsymbol{x}_0)\ (x_i - x_{0i}), \tag{4.13}$$

with respect to the vehicle state $\boldsymbol{x} = (\dot{x}_b, y, \theta, \dot{\theta})$ along a reference trajectory $\boldsymbol{x}_0 = (v_0, 0, 0, 0)$, corresponding to a centerline flight path at a constant velocity v_0. As predicted from the analysis in Section 3.3, the b_1 mode is an estimate of the average global image velocity and, more specifically, yields a signal that is proportional to the forward speed v. In addition, the first and second cosine harmonics a_1 and a_2 provide rotary stiffness θ and lateral stiffness y, respectively, while the DC component a_0 is a function of rotary damping $\dot{\theta}$ and lateral stiffness y. The higher order spatial harmonics a_n,b_n for $n = 2, 4, \ldots$ are all zero due to the fact that all odd sine and cosine harmonics greater than one of the nearness function are zero (Table 3.1). In addition, the linearizations of a_n and b_n for $n = 1, 3, \ldots$ provide the same state information as for $n = 1$, just at a reduced gain. Therefore, we will attempt to stabilize the centering and clutter responses with the b_1, a_0, a_1, and a_2 spatial harmonics of optic flow, reflected in the choice of the observation equation $\boldsymbol{z} = C\boldsymbol{x}$ below:

$$\begin{pmatrix} z_{b_1} \\ z_{a_0} \\ z_{a_1} \\ z_{a_2} \end{pmatrix} = \begin{pmatrix} \frac{8}{3\pi a} & 0 & 0 & 0 \\ 0 & \frac{v_0}{\sqrt{2}a^2} & 0 & -\sqrt{2} \\ 0 & 0 & \frac{4v_0}{3\pi a} & 0 \\ 0 & -\frac{v_0}{4a^2} & 0 & 0 \end{pmatrix} \begin{pmatrix} v \\ y \\ \theta \\ \dot{\theta} \end{pmatrix}. \tag{4.14}$$

For $v_0 \neq 0$, C is full rank, and hence in the linearization we effectively have the equivalent of full state feedback since C is invertible. Notice in (4.12) that the v dynamics are decoupled from the y, θ dynamics, in (4.14) the linearized b_1 output is a function of v only, and the linearized a_0, a_1, a_2 outputs are functions of $y, \theta, \dot{\theta}$. Hence, with the linearized system we can effectively decouple the control problem into the *clutter* (forward speed regulation) response and the *centering* (obstacle avoidance) response.

Forward Speed Regulation

For the forward speed regulation task, we define a reference forward velocity r and corresponding scaling factor N and close the loop by setting the thrust input

$$u_1 = K_{11}^b(Nr - b_1), \tag{4.15}$$

where $b_1 = \langle \dot{Q}, \sin\gamma \rangle_w$, corresponding to the motion sensitivity function

$$F_{u_1}(\gamma) = K_{11}^b \sin\gamma. \tag{4.16}$$

With $r = v_0$, choose $N = 8/(3\pi a)$ for zero steady-state error, and the linearized closed loop dynamics become

$$\dot{v} = -\frac{N}{m} K_{11}^b (v - v_0).$$

One can easily verify that with $K_{11}^b > 0$, the closed loop eigenvalue is in the open left-half plane, and therefore local stability of the nonlinear system is achieved.

Obstacle Avoidance

A quick check of the controllability and observability matricies shows that the linearized system is completely controllable and observable about the equilibrium point $\boldsymbol{x}_0$ as long as $v_0 \neq 0$. Therefore, due to the coupling of the lateral to the rotational dynamics through the $v_0\theta$ term in (4.12), it is possible to accomplish stabilization of both modes via static output feedback through the torque input, taken to be

$$u_2 = K_{20}^a a_0 + K_{21}^a a_1 + K_{22}^a a_2. \tag{4.17}$$

Hence $u_2 = \langle \dot{Q}, F_{u_2} \rangle_w$, corresponding to the motion sensitivity function

$$F_{u_2}(\gamma) = K_{20}^a + K_{21}^a \cos\gamma + K_{22}^a \cos 2\gamma. \tag{4.18}$$

With this choice of torque control, the characteristic equation for the linearized closed loop

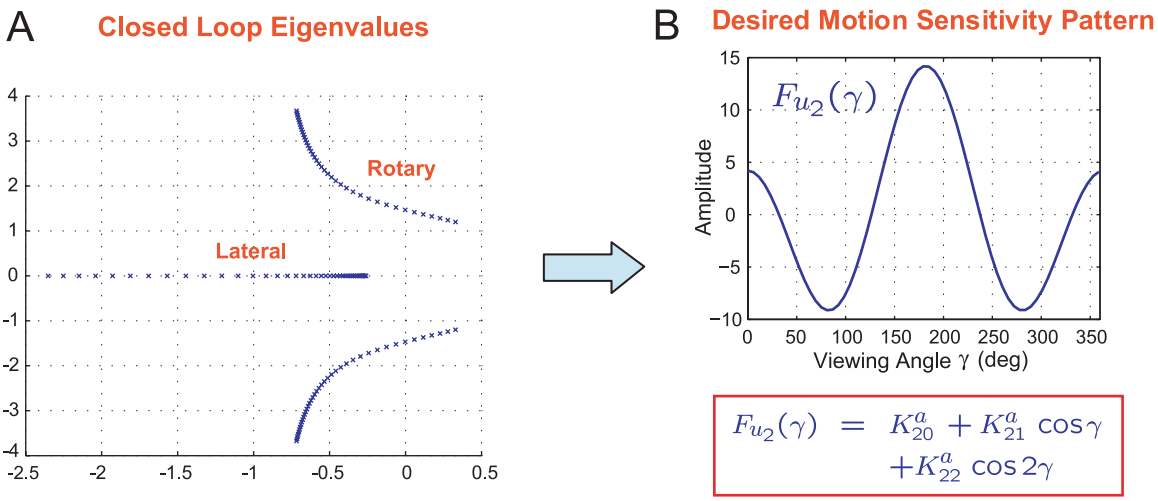

Figure 4.4: Connections between closed loop wheeled robot behavior (eigenvalues) and retinal motion sensitivity shape. (A) Root locus plot for $K^a_{20} = 0.1$, $K^a_{22} = 1.0$, and $-2 \leq K^a_{21} \leq 0$. (B) Once the desired closed loop eigenvalues (solutions to (4.19)) are selected, the shape of the motion sensitivity function is determined by the coefficients of the characteristic polynomial.

dynamics is

$$s^3 + \frac{K^a_{20}}{J}s^2 - \frac{8K^a_{21}v_0}{3J\pi a}s + \frac{v_0(K^a_{22} - \sqrt{2}K^a_{20})}{Ja^2} = 0. \tag{4.19}$$

The natural dynamics contain only inertial and viscous terms; therefore to achieve a stable centering/obstacle avoidance response, we require $K^a_{21} < 0$ for rotational stiffness and $K^a_{22} > 0$ for lateral stiffness. Additionally, rotational damping can be added with $K^a_{20} > 0$; however the linearization of the DC component a_0 of $\dot{Q}$ also has a lateral imbalance term (Table 4.1), and hence we further need the restriction $K^a_{22} > \sqrt{2}K^a_{20}$ to provide the correctly signed lateral stiffness required for a stable centering response.

4.2.3 Simulations of WFI-Based Navigation

Simulations were constructed based on the full nonlinear planar flight dynamics (4.10) to study the performance of the WFI control methodology in general environments (Figure 4.5). Environments were defined as bitmaps and converted to grayscale using the Matlab command `rgb2gray()`, which eliminates the hue and saturation information resulting in a matrix where a zero entry is defined as level ground and a nonzero entry as a point on an obstacle. At each instant in time the depth, or the distance to the near-

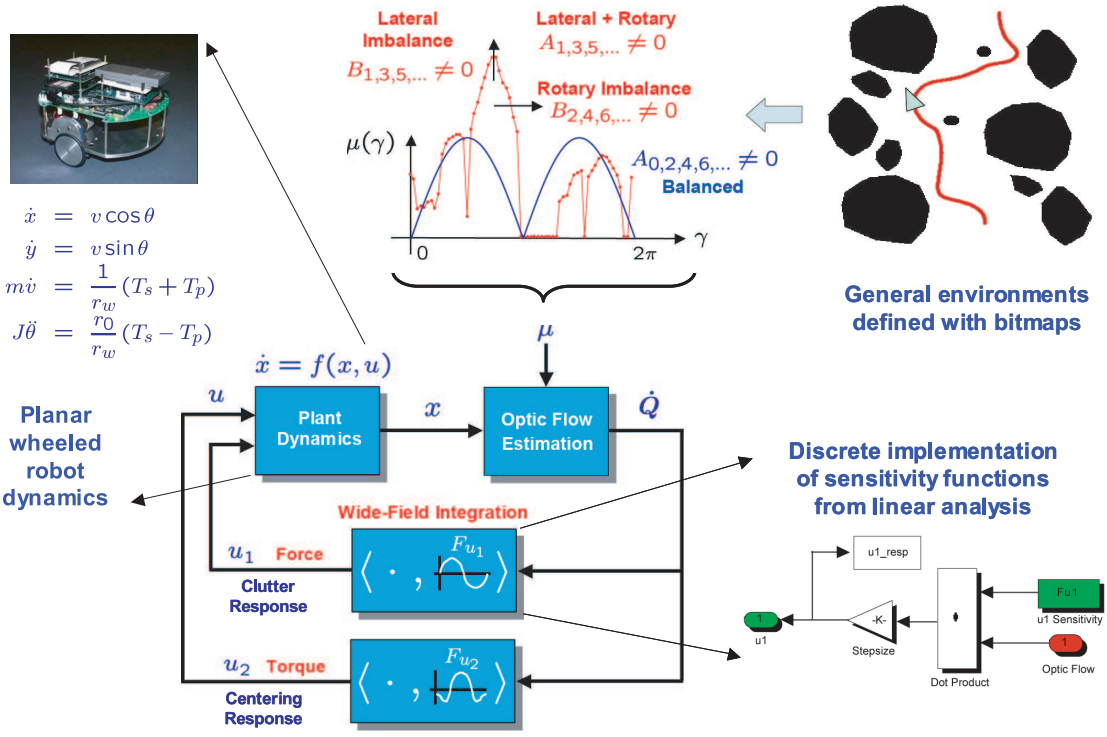

Figure 4.5: Simulations of WFI-based navigation. Full nonlinear vehicle dynamics are combined with a spatially-discretized optic flow estimation block. General environments are defined with bitmaps, from which the instantaneous nearness function is estimated. Force and torque control inputs are generated with a discrete inner product of the optic flow estimate and appropriately sampled sensitivity functions F_{u_i}.

est obstacle in the environment from the current location and orientation, is estimated at locations $\Gamma = [0 : \Delta\gamma : 2\pi]$, spaced equidistant by $\Delta\gamma$ about the circumference of the vehicle, for a total of $N = \texttt{floor}(2\pi/\Delta\gamma)$ points. The vehicle's current configuration $\mathbf{q}(t_i) = (x(t_i), y(t_i), \theta(t_i))$ is provided by the plant dynamics block that integrates the vehicle equations of motion. The planar nearness function $\mu(\gamma_j, t_i)$ is then computed by inverting the depth information at locations Γ. The instantaneous optic flow $\dot{Q}(\gamma_j, t_i)$ is computed by combining the instantaneous nearness function with the current kinematics $\dot{\mathbf{q}}(t_i) = (\dot{x}_b(t_i), \dot{y}_b(t_i), \dot{\theta}(t_i))$, from the vehicle dynamics block, according to

$$\dot{Q}(\gamma_j, t_i) \quad = \quad -\dot{\theta}(t_i) + \mu(\gamma_j, t_i) \cdot [\dot{x}_b(t_i)\sin\gamma_j - \dot{y}_b(t_i)\cos\gamma_j]. \tag{4.20}$$

Force and torque control inputs are generated by taking the discrete inner product of the instantaneous optic flow with appropriately sampled versions of the motion sensitivity func-

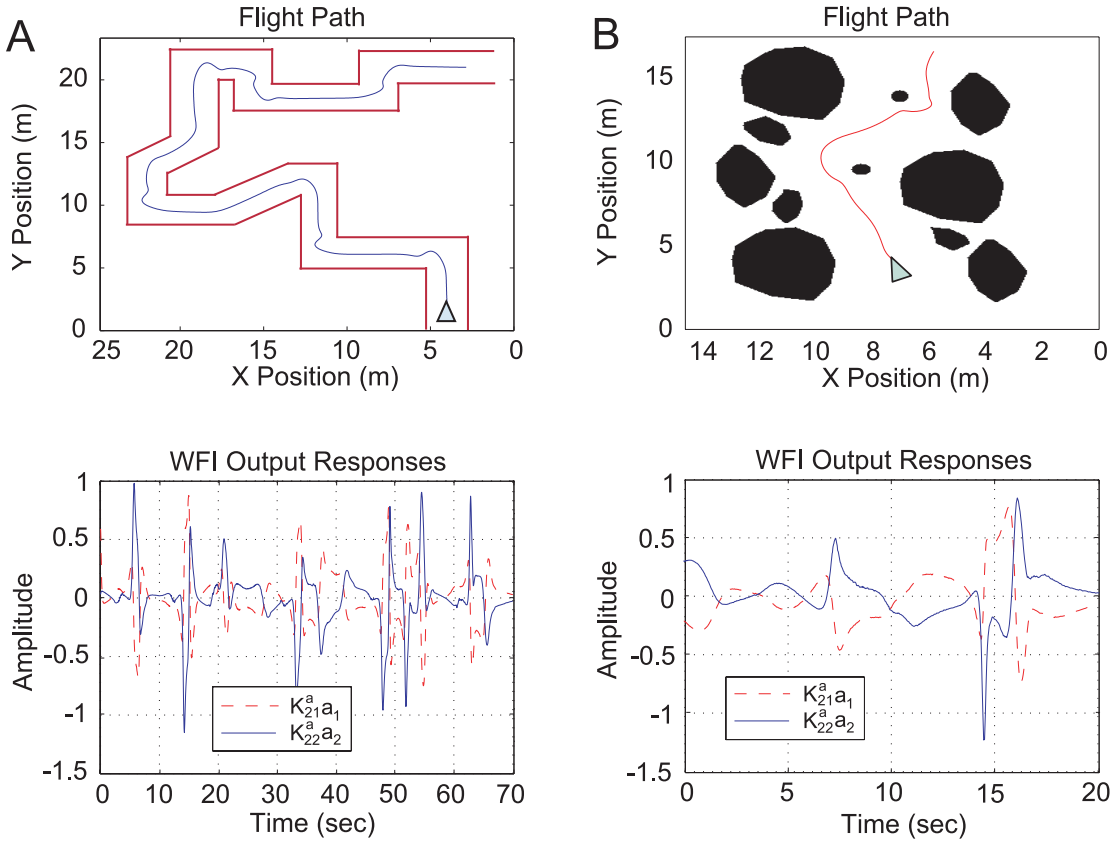

Figure 4.6: Simulations of WFI-based navigation. (A) Corridor navigation (B) Obstacle field navigation

tions (4.16) and (4.18):

$$u(t_i) \quad = \quad \frac{\Delta\gamma}{\pi} \sum_{j=1}^{N} \dot{Q}(\gamma_j, t_i) \cdot F_u(\gamma_j). \tag{4.21}$$

Sensitivity gains K^a_{ij} and K^b_{ij} used in the simulation were chosen based on the performance index of maximizing the bandwidth of the slow (lateral) mode in the linearized closed loop system (4.19). In Figure 4.6, the vehicle was directed to navigate a complicated corridor (C) and an obstacle field (D). Body velocities are shown for the corridor, and the responses of the first two cosine harmonics of the optic flow are shown for the obstacle field. The corrective torque for the lateral imbalance is supplied by a_2, and the dynamics are stabilized with the opposing rotational stiffness from a_1.

4.2.4 Global Stability Analysis

For the planar tunnel geometry, odd spatial harmonics A_k, B_k are zero for $k > 1$, and therefore we can obtain reduced expressions for the amplitide and phase of the second spatial harmonic of optic flow

$$\begin{aligned} A_2 &= \sqrt{a_2^2 + b_2^2} = \frac{y}{a^2 - y^2}\, \dot{x}_b \\ \Theta_2 &= \tan^{-1}\left(\frac{b_2}{a_2}\right) = -\theta. \end{aligned} \tag{4.22}$$

Under the assumptions that the forward speed is held constant $\dot{x}_b = v_0$ and the rotational inertia is negligible, the dynamics are

$$\begin{aligned} \dot{y} &= v_0 \sin\theta \\ \dot{\theta} &= u_2. \end{aligned} \tag{4.23}$$

Therefore, we consider the following control law (distinct from the control law proposed in Section 4.2.2)

$$u_2 = -K_\theta \theta + K_y \frac{y}{a^2 - y^2}\, v_0 \frac{\sin\theta}{\theta}, \tag{4.24}$$

based on the information available from (4.22). The Lyapunov function candidate

$$V = \frac{\theta^2}{2} + V_0 - \frac{1}{2}\ln\left(y^2 - a^2\right) \tag{4.25}$$

has derivative

$$\dot{V} = -K_\theta \theta^2 \leq 0,$$

hence utilizing LaSalle's principle we can conclude that the equilibrium $(y, \theta) = (0, 0)$ of the closed loop system is globally asymptotically stable.

4.3 Hovercraft Control

In this section we demonstrate the utility of WFI sensory outputs (3.4) through coupling with planar flight dynamics via static output feedback (Figure 4.1). For analysis and simulation purposes we will use the dynamics of the hovercraft from the Caltech multi-vehicle wireless testbed [10]. The vehicle admits planar translational motion (surge, sway) and a single axis of rotary motion (yaw). For the inertial configuration $\mathbf{q} = (x, y, \theta)$ the equations of motion are

$$\begin{aligned} m\ddot{x} &= (F_s + F_p)\cos\theta - b\dot{x} \\ m\ddot{y} &= (F_s + F_p)\sin\theta - b\dot{y} \\ J\ddot{\theta} &= (F_s - F_p)r_0 - c\dot{\theta}. \end{aligned} \tag{4.26}$$

The translational and rotational damping coefficients are denoted by b and c, respectively, the starboard and port thruster forces are denoted by F_s and F_p, and r_0 denotes the thruster moment arm. The vehicle mass is given by m, and the rotational inertia about the yaw axis is J.

4.3.1 Navigation Methodology for Vehicles with Sideslip

In Section 4.2.1 a navigation methodology was proposed for vehicles of the wheeled or rolling type with the nonholonomic constraint that prevents sideslip motion, i.e. $\dot{y}_b = 0$. For vehicles such as hovercraft that exhibit unconstrained, three degree of freedom (3 DOF) planar dynamics, this constraint does not hold, and the resulting spatial harmonics of optic flow contain additional terms proportional to the sideslip velocity, $\dot{y}_b$:

$$\begin{aligned} b_1 &= \frac{\dot{x}_b}{2}(A_0 - A_2) + \frac{\dot{y}_b}{2}B_2 \\ a_0 &= -\sqrt{2}\dot{\theta} + \frac{\dot{x}_b}{\sqrt{2}}B_1 - \frac{\dot{y}_b}{\sqrt{2}}A_1 \\ a_1 &= \frac{\dot{x}_b}{2}B_2 + \frac{\dot{y}_b}{2}(A_0 + A_2) \\ a_2 &= \frac{\dot{x}_b}{2}(-B_1 + B_3) + \frac{\dot{y}_b}{2}(A_1 + A_3), \end{aligned} \tag{4.27}$$

Interpreting these signals in the context of the output regulation problem, we still seek to regulate the harmonic content of the nearness function such that we achieve a balanced

Table 4.2: Spatial Fourier Decomposition of Planar Tunnel Optic Flow for Vehicles with Sideslip

Mode	Tunnel Geometry	Linearization ($\boldsymbol{x}_0$)
a_0	$-\sqrt{2}\dot{\theta} + \frac{y}{\sqrt{2}(a^2-y^2)}\ (\dot{x}_b \cos\theta - \dot{y}_b \sin\theta)$	$-\sqrt{2}\dot{\theta} + \frac{v_0}{\sqrt{2}a^2}\ y$
a_1	$\frac{4a}{3\pi(a^2-y^2)}\left[\dot{x}_b \sin\theta\cos\theta + \dot{y}_b(\cos^2\theta - 2)\right]$	$\frac{4}{3\pi a}\left(v_0\theta - \dot{y}_b\right)$
b_1	$\frac{4a}{3\pi(a^2-y^2)}\left[\dot{x}_b(\cos^2\theta + 1) - \dot{y}_b \sin\theta\cos\theta\right]$	$\frac{8}{3\pi a}\dot{x}_b$
a_2	$\frac{y}{2(a^2-y^2)}\left(-\dot{x}_b\cos\theta - \dot{y}_b\sin\theta\right)$	$-\frac{v_0}{2a^2}\ y$
b_2	$\frac{y}{2(a^2-y^2)}\left(\dot{x}_b\sin\theta - \dot{y}_b\cos\theta\right)$	0
a_n, $n = 1, 3, \ldots$	$\frac{4a}{n\pi(a^2-y^2)(n^2-4)}\left[\left(n\sin\theta\cos n\theta - 2\cos\theta\sin n\theta\right)\dot{x}_b + \left(n\cos\theta\cos n\theta - 2\sin\theta\sin n\theta\right)\dot{y}_b\right]$	$-\frac{4}{\pi a(n^2-4)}\left(v_o\theta - \dot{y}_b\right)$
a_n, $n = 4, 6, \ldots$	0	0
b_n, $n = 1, 3, \ldots$	$-\frac{4a}{n\pi(a^2-y^2)(n^2-4)}\left[\left(n\sin\theta\sin n\theta + 2\cos\theta\cos n\theta\right)\dot{x}_b + \left(n\cos\theta\sin n\theta - 2\sin\theta\cos n\theta\right)\dot{y}_b\right]$	$-\frac{8}{n\pi a(n^2-4)}\dot{x}_b$
b_n, $n = 4, 6, \ldots$	0	0

shape containing DC and even (negative) cosine harmonics $\{A_k, k = 0, 2, 4, \ldots\}$. In addition, we will attempt to track a reference trajectory or equilibrium with zero sideslip [38]. Under this requirement most of the new terms in (4.27) that are proportional to $\dot{y}_b$ will be second order and higher, and the previous local analysis will be applicable. However, the new term in the a_1 harmonic, $\frac{\dot{y}_b}{2}(A_0 + A_2)$, is also proportional to the desired spatial content of the nearness function and will have a first order contribution. As we will be shown in the next section, this will result in a coupling of the rotational imbalance term that is proportional to θ with a lateral velocity term proportional to $\dot{y}_b$.

4.3.2 Local Asymptotic Stability Analysis

As in the wheeled robot case we will first examine the task of maintaining a forward reference velocity and trajectory along the centerline of a planar tunnel. The intent is to show feasibility of the proposed output feedback methodology, and hence a linearized control design that guarentees local asymptotic stability of speed regulation and obstacle avoidance responses will be discussed. With this assumed geometry we can explicity compute the spatial Fourier harmonics of the optic flow (Table 4.2), in terms of kinematic variables $\boldsymbol{x} = (\dot{x}_b, y, \dot{y}_b, \theta, \dot{\theta})$, along with their linearization $z(\boldsymbol{x}) = z(\boldsymbol{x}_0) + \sum_i \frac{\partial z}{\partial x_i}(\boldsymbol{x}_0)\ (x_i - x_{0i})$ with respect to the reference trajectory $\boldsymbol{x}_0 = (v_0, 0, 0, 0, 0)$. Similar to the optic flow for the nonholonomic wheeled robot dynamics, the b_1 mode provides an estimate of the average global image velocity, the a_2 mode provides an estimate of the lateral imbalance y, and the DC component a_0 is a function of the angular velocity $\dot{\theta}$ and lateral imbalance y. However, the a_1 mode, which previously gave an estimate of the rotary imbalance, now provides a signal where the rotary imbalance θ is coupled with the lateral velocity $\dot{y}_b$. Due to this coupling, we no longer have the equivalent of full state feedback in the linearized system. However, we will attempt to stabilize the centering and clutter responses with the b_1, a_0, a_1, and a_2 spatial harmonics of optic flow.

In the following analysis it will be beneficial to define the state of the vehicle in terms of inertial coordinates $\boldsymbol{x} = (v, y, \dot{y}, \theta, \dot{\theta})$, where $v = \dot{x}$, and the inputs as

$$\begin{aligned} u_1 &= F_s + F_p - bv_0 \\ u_2 &= r_0(F_s - F_p), \end{aligned} \tag{4.28}$$

so that nominally a zero input is required to hold the vehicle at equilibrium. Assuming small states (other than v) and control inputs, the linearized equations of motion for a centerline flight trajectory become

$$\begin{aligned} m\dot{v} &= u_1 + b(v_0 - v) \\ m\ddot{y} &= b(v_0\theta - \dot{y}) \\ J\ddot{\theta} &= u_2 - c\dot{\theta}. \end{aligned} \tag{4.29}$$

With the above state definition, the observation equation $\boldsymbol{z} = C\boldsymbol{x}$ becomes

$$\begin{pmatrix} z_{b_1} \\ z_{a_0} \\ z_{a_1} \\ z_{a_2} \end{pmatrix} = \begin{pmatrix} \frac{8}{3\pi a} & 0 & 0 & 0 & 0 \\ 0 & \frac{v_0}{\sqrt{2}a^2} & 0 & 0 & -\sqrt{2} \\ 0 & 0 & -\frac{4}{3\pi a} & \frac{8v_0}{3\pi a} & 0 \\ 0 & -\frac{v_0}{2a^2} & 0 & 0 & 0 \end{pmatrix} \begin{pmatrix} v \\ y \\ \dot{y} \\ \theta \\ \dot{\theta} \end{pmatrix}. \tag{4.30}$$

Note that the observation matrix C is full row rank for $v_0 \neq 0$; however due to the coupling in the $\dot{y}$ and θ states we have constrained state feedback and will not be able to arbitrarily place the closed loop poles in a linear design. However, in (4.29) the v dynamics are decoupled from the y, θ dynamics, in (4.30) the linearized b_1 output is a function of v only, and the linearized a_0, a_1, a_2 outputs are functions of $y, \dot{y}, \theta, \dot{\theta}$. Hence, with the linearized system we can again decouple the control problem into the *clutter* (forward speed regulation) response and the *centering* (obstacle avoidance) response.

Forward Speed Regulation

For the forward speed regulation task, we define a reference forward velocity r and corresponding scaling factor N and close the loop by setting the thrust input

$$u_1 = K_{11}^b(Nr - b_1), \tag{4.31}$$

where $b_1 = \langle \dot{Q}, \sin\gamma \rangle_w$, corresponding to the motion sensitivity function

$$F_{u_1}(\gamma) = K_{11}^b \sin\gamma. \tag{4.32}$$

With $r = v_0$, choose $N = 8/(3\pi a)$ for zero steady-state error, and the linearized closed loop dynamics become

$$\dot{v} \quad = \quad -\frac{1}{m}\left(K_{11}^b N + b\right)(v - v_0). \tag{4.33}$$

One can easily verify that with $K_{11}^b > -b/N$, the closed loop eigenvalue is in the open left half plane, and therefore local stability of the nonlinear system is achieved.

Obstacle Avoidance

In terms of the control task we have two difficulties not present with the wheeled robot dynamics. First, the linearized observation equation (4.30) is not invertible, and therefore it is not possible to arbitrarily place the closed loop eigenvalues with static output feedback. In addition, for the underactuated hovercraft no control input is available in the sideslip (sway) direction. However, the lateral dynamics are coupled to the rotational dynamics through the $bv_0\theta$ term in (4.29), and hence it is possible to accomplish stabilization of both flight modes through the torque input, taken to be

$$u_2 \quad = \quad K_{20}^a a_0 + K_{21}^a a_1 + K_{22}^a a_2, \tag{4.34}$$

and hence $u_2 = \langle \dot{Q}, F_{u_2} \rangle_w$, corresponding to the motion sensitivity function

$$F_{u_2}(\gamma) \quad = \quad K_{20}^a + K_{21}^a \cos\gamma + K_{22}^a \cos 2\gamma. \tag{4.35}$$

With this choice of torque control, the characteristic equation for the linearized closed loop dynamics is

$$\begin{aligned} s^4 + \left(\frac{b}{m} + \frac{c + \sqrt{2}K_{20}^a}{J}\right)s^3 + \left(\frac{bc}{mJ} + \frac{\sqrt{2}bK_{20}^a}{mJ} - \frac{4K_{21}^a v_0}{3\pi Ja}\right)s^2 \\ -\frac{4K_{21}^a bv_0}{3\pi mJa}s + \frac{v_0^2 b(K_{22}^a - \sqrt{2}K_{20}^a)}{2mJa^2} \quad = \quad 0. \end{aligned} \tag{4.36}$$

The natural dynamics contain only inertial and viscous terms, and therefore to achieve a stable centering/obstacle avoidance response, we require $K_{21}^a < 0$ for rotational stiffness and $K_{22}^a > 0$ for lateral stiffness. Additionally, rotational damping can be added with $K_{20}^a > 0$;

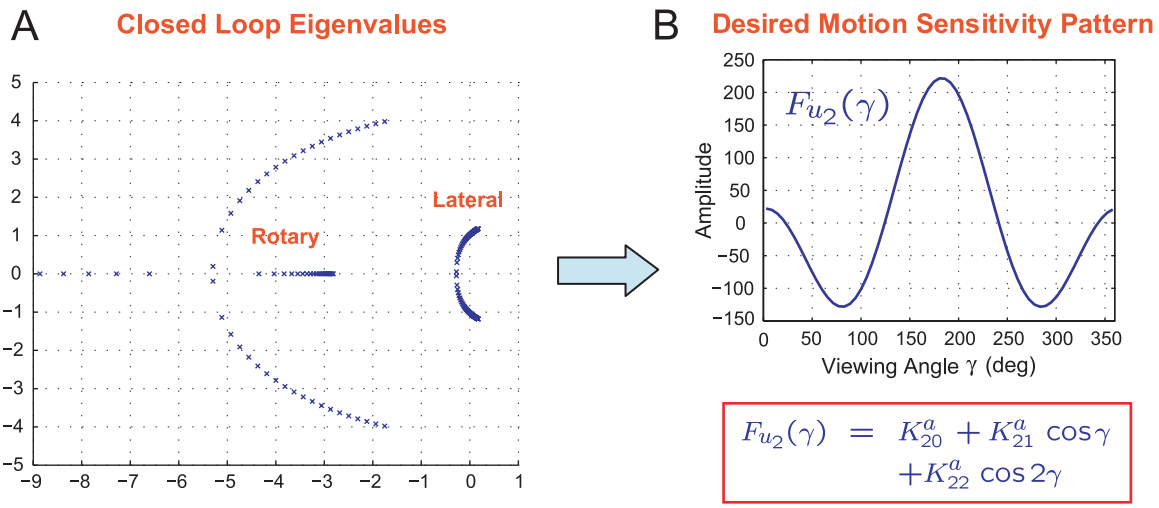

Figure 4.7: Connections between closed loop hovercraft behavior (eigenvalues) and retinal motion sensitivity shape. (A) Root locus plot for $K^a_{20} = 2.0$, $K^a_{22} = 6.0$, and $-22 \leq K^a_{21} \leq -14$. (B) Once the desired closed loop eigenvalues (solutions to (4.36)) are selected, the shape of the motion sensitivity function is determined by the coefficients of the characteristic polynomial.

however the linearization of the DC component a_0 of $\dot{Q}$ also has a lateral imbalance term (4.30), and hence we further need the restriction $K^a_{22} > \sqrt{2}K^a_{20}$ to provide the lateral stiffness required for a stable centering response (Figure 4.7).

4.3.3 Comparisons with Experimental Assays

It is useful at this point to make some comparisons with the experimental assays in honeybee tunnel navigation, namely the converging-diverging tunnel [60] and the moving wall [58], as discussed in Chapter 1. The converging-diverging tunnel assay investigated the hypothesis that bees control forward flight speed based on retinal image velocity, which is a behavior also described as the clutter response [2]. In experiments it was observed that bees regulated their forward flight speed in proportion to tunnel width; the more narrow the tunnel, the slower the flight speed, and vice-versa. It was concluded from the data that bees strive to hold constant the angular velocity of the image, i.e., the optic flow, within the lateral region of the eye.

To test whether or not the forward speed regulation methodology proposed in this thesis would give rise to this behavior, a converging-diverging tunnel environment was constructed (Figure 4.8A), and a simulation of the hovercraft using the controller described in Section 4.3.2 was performed. The axial and lateral velocities are plotted as a function of tunnel

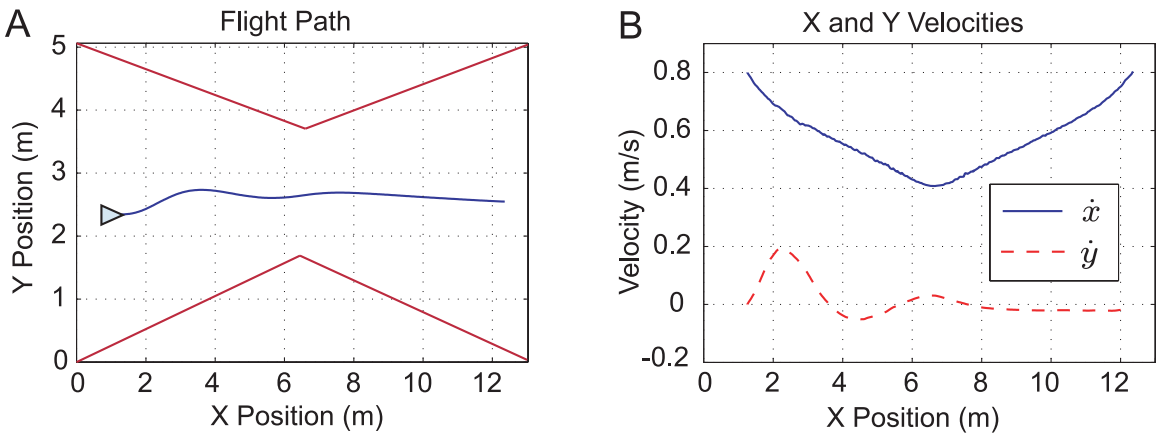

Figure 4.8: Simulations of WFI-based forward speed regulation (clutter rersponse). (A) Hovercraft flight path for a converging-diverging tunnel. (B) Clutter response; the forward speed of the hovercraft is proportional to the tunnel width.

position in Figure 4.8B. The initial condition started the hovercraft off-center, so we see the centering response in the lateral velocity. However, as seen in experiments, the forward speed of the hovercraft is indeed proportional to the tunnel width, as one would expect.

In the moving wall experiments [58], the centering response was examined. Honeybees were directed to fly down a tunnel with one of the walls moving at a constant rate along the flight path. It was observed that when the walls were stationary the bees tended to fly along the centerline, but when one wall was given constant motion along (against) the direction of travel, bees shifted their trajectories toward (away from) the moving wall. Within the framework we have constructed we can investigate the moving wall assay by modifying the planar tunnel optic flow with a constant left- or right-wall velocity bias (Figure 4.9A):

$$-v_w\ \hat{\boldsymbol{e}}_x \quad = \quad -v_w \cos\theta\ \hat{\boldsymbol{e}}_{x_b} + v_w \sin\theta\ \hat{\boldsymbol{e}}_{y_b}. \tag{4.37}$$

Hence,

$$\dot{x}_b \quad \mapsto \quad \dot{x}_b + v_w \cos\theta \tag{4.38}$$

$$\dot{y}_b \quad \mapsto \quad \dot{y}_b + v_w \sin\theta, \tag{4.39}$$

for $0 \leq \gamma + \theta < \pi$ (left wall movement) or $\pi \leq \gamma + \theta < 2\pi$ (right wall movement). Assuming

Table 4.3: Fourier Expansion of Optic Flow For a Moving Wall

Mode	Left Moving Wall
a_0	$-\dot{\theta} + \frac{1}{2(a^2-y^2)}\ \left[(\dot{x}_b\cos\theta - \dot{y}_b\sin\theta)\,y + v_w(a+y)(\cos^2\theta - \frac{1}{2})\right]$
a_1	$\frac{2}{3\pi(a^2-y^2)}\left[a\dot{x}_b\sin\theta\cos\theta + a\dot{y}_b(\cos^2\theta - 2) + v_w\sin\theta(a+y)(\cos^2\theta - 1)\right]$
b_1	$\frac{2}{3\pi(a^2-y^2)}\left[a\dot{x}_b(\cos^2\theta + 1) - a\dot{y}_b\sin\theta\cos\theta + v_w\cos^3\theta(a+y)\right]$
a_2	$\frac{y}{4(a^2-y^2)}\left[-(\dot{x}_b\cos\theta + \dot{y}_b\sin\theta)y - \frac{v_w}{2}(a+y)\right]$
b_2	$\frac{y}{4(a^2-y^2)}\,(\dot{x}_b\sin\theta - \dot{y}_b\cos\theta)$

left wall movement, the resulting optic flow is

$$\dot{Q}_w(\gamma, \mathbf{q}, \dot{\mathbf{q}}) = \begin{cases} -\dot{\theta} + \frac{\sin(\gamma+\theta)}{a-y}[(v_{x_b} + v_w\cos\theta)\sin\gamma & 0 \le \gamma+\theta < \pi \\ \qquad -(v_{y_b} + v_w\sin\theta)\cos\gamma] & \\ -\dot{\theta} - \frac{\sin(\gamma+\theta)}{a+y}\,(v_{x_b}\sin\gamma - v_{y_b}\cos\gamma) & \pi \le \gamma+\theta < 2\pi \end{cases} . \tag{4.40}$$

Similar to the case of a stationary planar tunnel, we can explicity compute the first several spatial Fourier harmonics of this optic flow (Table 4.3). The steady-state value $y = y_{ss}$ along the equilibrium trajectory

$$x_w : (v = v_0, y = y_{ss}, \dot{y} = 0, \theta = 0, \dot{\theta} = 0) \tag{4.41}$$

that results in a zero torque input $u_2 = \langle \dot{Q}_w, F_{u_2} \rangle_w|_{x_w} = 0$ is

$$y_{ss} \;=\; -\frac{a v_w}{2v_0 + v_w}. \tag{4.42}$$

Motion opposite the flight direction ($v_w > 0$) will result in a shift right ($y_{ss} < 0$) of the steady-state flight path while motion along the flight direction ($v_w < 0$) will result in a shift left ($y_{ss} > 0$), as observed in [58]. Also as $v_w \to 0$, $y_{ss} \to 0$ and as $v_w \to \pm\infty$, $y_{ss} \to \mp a$. The simulated hovercraft flight path for left wall motion with $v_w > 0$ is plotted in Figure 4.9, along with the time response of the first two spatial cosine harmonics a_1,a_2 of the optic flow. As discussed in the previous section, a_2 provides a corrective torque for the lateral

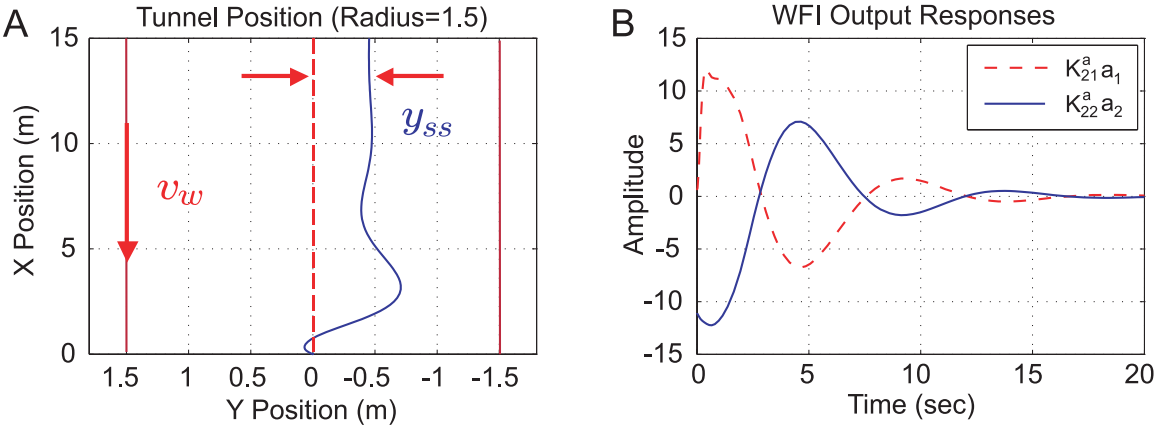

Figure 4.9: Simulations of WFI-based centering response. (A) Hovercraft flight path for a moving wall. (B) 1st and 2nd cosine harmonics of optic flow; a_2 is an estimate of the lateral spatial imbalance, which adds lateral stiffness, and a_1 provides a stabilizing rotational stiffness.

imbalance, and a_1 provides the opposing rotational stiffness required for stabilization.

Based on the analysis and simulations presented, we conclude that the proposed forward speed regulation and obstacle avoidance methodologies have sufficient complexity to give rise to experimentally observed navigational heuristics as the centering and clutter responses exhibited by honeybees. It is important to note that these reflexive behaviors were demonstrated using only sensory information obtained through wide-field integration of optic flow.

4.3.4 Simulations of General Environments

The closed loop behavior of this output feedback methodology was also evaluated in more complicated environments. Using the same feedback structure and gains, the vehicle was directed to navigate a complicated corridor (Figure 4.10A) and an obstacle field (Figure 4.10B). Body velocities are shown for the corridor, and the response of the first two cosine harmonics of the optic flow are shown for the obstacle field.

4.3.5 Limitations of the Proposed Centering Approach

The LPTC pathway (Figure 1.1) that forms the basis of the obstacle avoidance (centering) methodology is one of several feedback circuits found in insect visuomotor neurobiology. Experimental evidence [13] suggests that visual expansion is critical in triggering the rapid body saccades that contribute to obstacle avoidance behavior in free flight. When insects

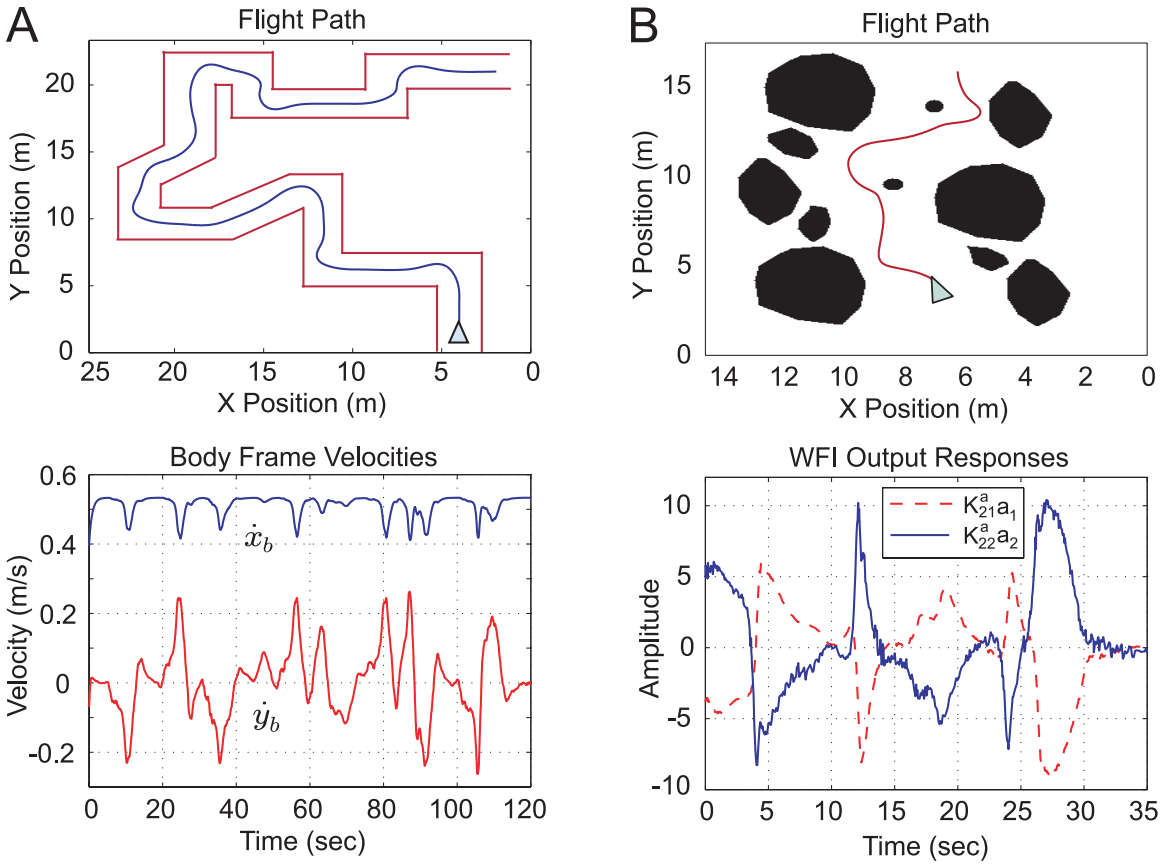

Figure 4.10: Simulations of WFI-based navigation. (A) Centering response for a maze and body frame velocities as a function of time. (B) General obstacle field navigation with time traces of the 1st and 2nd cosine harmonics of optic flow; a_2 is an estimate of the lateral spatial imbalance, which adds lateral stiffness, and a_1 provides a stabilizing rotational stiffness.

experience sustained expansion on a given side, they modulate wingstroke amplitude to turn away from the expanding stimulus [63]. When expansion occurs directly in front, this tends to elicit a landing response where the insect will rapidly extend their legs and increase wingbeat frequency [3]. The centering methodology proposed in this chapter can handle a wide range of spatially distributed environments. However, frontally symmetric object distributions, such as the one a vehicle would experience when oriented ninety degrees to a wall or a tunnel that converges symmetrically to a point, will not produce a lateral imbalance signal when the vehicle is maintaining a forward reference trajectory. In these types of cases a more general obstacle avoidance methodology, such as one that takes advantage of the expansion detection circuitry and algorithms utilized by insects, could be implemented to increase robustness of an optic flow based approach.

4.4 Comparisons with Previous Work

Local navigation of planar corridors and obstacle fields by wheeled robots utilizing optic flow information has been demonstrated in several approaches; an excellent review and summary is given in [20]. Typically in these implementations the optic flow is measured in all or part of the 360° field of view using one of several methods, including image interpolation techniques based on captured camera images [57], the ratio of temporal to spatial image derivatives [53], or local motion detector (EMD) arrays based on photoreceptor inputs [17]. A centering response is achieved by *uniformly* balancing the lateral image motion, as was previously suggested in [55] based on data from honeybee experiments. The resulting controlled input is generated by a control law of the form

$$u \;=\; K(\bar{\dot{Q}}_L - \bar{\dot{Q}}_R), \tag{4.43}$$

where K is a static gain and $\bar{\dot{Q}}_L$ and $\bar{\dot{Q}}_R$ represent the averaged image flow on the left and right sides, respectively. This type of implementation is based on the motion parallax formulation by [68] that assumes that the components of the optic flow due to rotary and lateral motion are negligible, i.e. the angular speed of an object at retinal angle γ, distance d, and due to forward translatory motion v_0 is

$$\Omega \;=\; \frac{v_0}{d}\sin\gamma. \tag{4.44}$$

In this case, if v_0 is known and $\Omega(\gamma)$ is measured, equation (4.44) can be averaged to generate a signal, representing the spatial imbalance, which is reflective the spatial distribution of objects $d(\gamma)$ located in the two lateral fields of view.

The assumption of zero lateral velocity holds for wheeled or rolling robots, assuming the sensor location is mounted along the axis of rotation, as these types of vehicles are subject to a nonholonomic constraint that precludes lateral motion (4.8). The controlled input (4.43), being a uniform average of the actual optic flow (4.9) experienced by wheeled robots, is composed of contributions from both rotational and translational motion. In applications where the rotational motion is significant, implementation required active removal of the rotary component [8], [66] or minimization to a sufficiently low level [53], [14].

The necessity for extraction of the rotary optic flow component under closed loop control

utilizing (4.43) is very clear once the theory developed in previous chapters is applied. In the corridor navigation case with a 360° field of view as in [17] and [66], the resulting control action (4.43) is the DC component of the azimuthal retinal motion field

$$a_0 \;=\; \frac{1}{\pi}\int_0^{2\pi} \dot{Q}_\gamma \cdot \frac{1}{\sqrt{2}}\, d\gamma, \tag{4.45}$$

which linearized about a centerline trajectory (Table 4.1) is given by

$$z_{a_0} \;=\; -\sqrt{2}\dot{\theta} + \frac{v_0}{\sqrt{2}a^2}\, y. \tag{4.46}$$

With the rotational contribution $\sqrt{2}\dot{\theta}$ is removed, the resulting signal is proportional to the lateral displacement y from the centerline. Similarly, for a partial lateral field of view (Figure 4.3), spanning $0 < \gamma_0 \leq \pi$ and symmetric about both the x_b and y_b body axes as in [9] and [53], we have a scaled version of (4.46):

$$z \;=\; -\frac{\sqrt{2}\gamma_0}{\pi}\dot{\theta} + \frac{v_0(\gamma_0 + \sin\gamma_0)}{\sqrt{2}a^2\pi}\, y, \tag{4.47}$$

which again provides the lateral displacement information once the rotation component has been removed. If this rotary term is not removed or minimized, it necessarily adds positive (destabilizing) rotational damping.

In alternative navigation strategies where vehicle dynamic stabilization is assumed or inherent, optic flow (image motion) has been considered as a source of depth information directly versus the more common stereo vision implementations that compute range. The advantage of the optic flow approach is that the computation times required are significantly less than the traditional stereo vision algorithms which solve the correspondence problem [55]. In [17], incremental translational motion is imposed on the wheeled robot so that in between small forward steps at a known velocity it can utilize (4.44) to back out estimates of depth. A similar type of wheeled robot implementation can be found in [54], where a zig-zag motion behavior is the result of imposing a forward motion constraint. The robot is only allowed to travel forward short distances incrementally at a known speed while it computes lateral optic flow to determine estimates of range, then prior to the subsequent translation it turns toward a known obstacle, where it can then travel a short distance safely and gather information about additional obstacles. This methodology is also a result of utilizing (4.44),

as it is difficult to accurately compute range measurements in the direction of translation ($\gamma = 0$) since the image velocity is small and measurements can be rendered unreliable due to noise.

A 3-D optic flow based ranging strategy has been examined in [7]. In this effort, an algorithm was developed for obtaining omnidirectional range maps from a panoramic image sensor positioned on a robotic gantry. The range, once again, is computed by translating the panoramic sensor through a known distance. In this case, however, an image interpolation algorithm was used to compute image deformation [57]. Once the instantaneous range map is computed, the various parts of the range image were tested for an obstacle free tunnel of a given width, resulting in a local navigation strategy.

There are two drawbacks to the range-based navigation approaches described above. In all three cases, incremental forward translational kinematics were imposed on the robots in order to compute accurate range information. Therefore, in realistic MAV/UAV types of vehicles where rotary and lateral motions are not negligible, especially micro-helicopter or flapping flight based realizations, the techniques (as implemented) are not extendable. Additionally, velocity measurements were required in all cases in order to back out the range information from the measured optic flow.

In conclusion, the planar navigation demonstrations to date have only utilized a limited part of the information that is available from optic flow. Through the LPTC-inspired wide-field integration approach developed in this thesis, additional information is available that can be used to significantly increase closed loop stability and performance, as well as simplify sensory and actuation requirements. Specifically, the lateral imbalance can be directly estimated from a $F(\gamma) = \cos 2\gamma$ motion sensitivity function, which eliminates the need for actively removing the rotation term from the DC component and allows for the possibility of injecting rotational damping using the $F(\gamma) = 1/\sqrt{2}$ motion sensitivity function. In addition, the orientation with respect to a balanced nearness function can be determined using a $F(\gamma) = \cos\gamma$ sensitivity, which can be used to add rotational stiffness to the loop, and the global translational image velocity can be extracted using the $F(\gamma) = \sin\gamma$ sensitivity, which can be used in forward speed regulation.

These conclusions become important when extending optic flow stabilization and navigation methodologies to the planar flight (hovercraft) problem posed in Section 4.3, as lateral and rotational stiffnesses are required in order to achieve a stable closed loop configuration.

To the author's knowledge, this is the first demonstration of planar, 3 DOF flight stabilization, as well as obstacle avoidance and forward speed regulation behaviors utilizing *solely* optic flow sensory information. Comparable implementations have not successfully solved the problem of simultaneous planar navigation and stabilization as they require additional types of sensory modalities and enforce kinematic constraints on the vehicle's motion.

Chapter 5

Pitch-Altitude Control and Terrain Following

In this chapter we demonstrate WFI-based hovering, pitch-altitude stabilization, and terrain following behaviors with planar rotorcraft flight dynamics via dynamic output feedback. We will assume a circular optic flow sensor oriented in the vertical plane (Figure 2.4), which measures the optic flow (Section 2.18):

$$\dot{Q}(\beta, \mathbf{q}, \dot{\mathbf{q}}) \;=\; -\dot{\phi} + \mu(\beta, \mathbf{q})\,(\dot{x}_b \sin\beta - \dot{z}_b \cos\beta)\,. \tag{5.1}$$

The rotorcraft (Figure 5.1A) admits planar translational motion in the x (thrust) and z (altitude) coordinates and has a single axis of rotary motion ϕ (pitch). In the inertial configuration $\mathbf{q} = (x, z, \phi)$ the equations of motion are

$$\begin{aligned} m\ddot{x} &= -(F_s + F_p)\sin\phi \\ m\ddot{z} &= (F_s + F_p)\cos\phi - mg \\ J\ddot{\phi} &= r_0(F_s - F_p). \end{aligned} \tag{5.2}$$

The starboard and port thruster forces are denoted by F_s and F_p, respectively, and r_0 denotes the rotor moment arm. The vehicle mass is given by m, and the rotational inertia about the pitch axis is J.

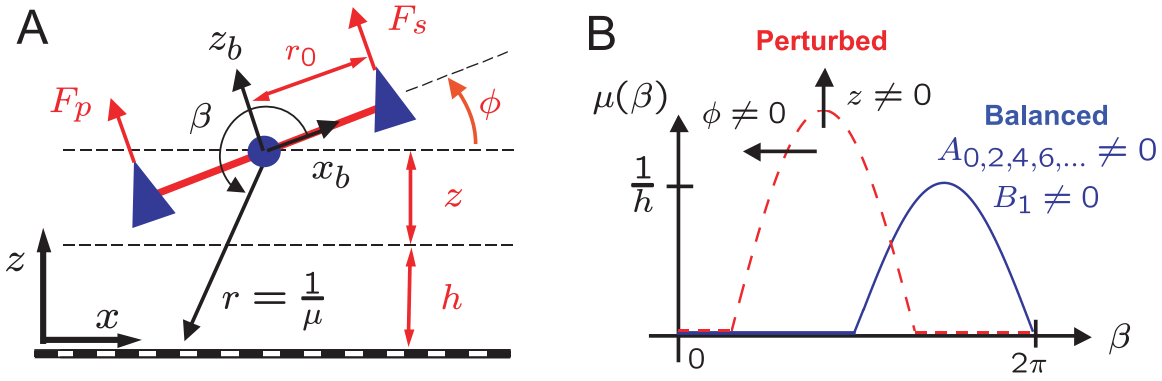

Figure 5.1: (A) Planar surface geometry and rotorcraft kinematic definitions (B) Altitude and pitch perturbations of the nearness function μ

5.1 Hover Stabilization Methodology

In this section we consider the interpretation of WFI outputs in the context of what is referred to as the *hover response*, where to achieve hover, the control system for the rotorcraft must zero the image velocity everywhere on the retina or optic flow sensor [2]. Since the measured optic flow at each point on the retina is proportional to the linear and angular velocity of the body frame, this can be achieved by zeroing the body frame velocities, assuming a rigid environment. In the following we propose a WFI-based control methodology that will stabilize the equilibrium point of the rotorcraft where the body frame velocities $\dot{x}_b$, $\dot{z}_b$, and $\dot{\phi}$ are zero, along with the pitch orientation ϕ. This methodology will not stabilize about a prescribed altitude, which is consistent with the author's observations of hoverflies that stabilize about the above equilibrium very effectively, but do not necessarily have a preferred height above ground to maintain.

If we assume a nearness function (3.8) describing a planar surface geometry, we can explicitly compute the spatial Fourier harmonics of the resulting optic flow in terms of kinematic variables $\boldsymbol{x} = (\dot{x}_b, z, \dot{z}_b, \phi, \dot{\phi})$ (Table 5.1). These signals contain information with respect to general velocity perturbations from a balanced nearness function (Figure 5.1B), composed of a fundamental sine harmonic B_1 and DC and even (negative) cosine harmonics $\{A_0, A_k, k = 2, 4, \ldots\}$. Table 5.1 also shows their linearization $y(\boldsymbol{x}) = y(\boldsymbol{x}_0) + \sum_i \frac{\partial y}{\partial x_i}(\boldsymbol{x}_0)\ (x_i - x_{0i})$ with respect to the hover equilibrum point $\boldsymbol{x}_0^h = (0, 0, 0, 0, 0)$. To leading order, we find the a_0 signal contains terms proportional to the pitch rate $\dot{\phi}$ and the lateral velocity $\dot{x}_b$, the a_1 signal is proportional to the vertical velocity $\dot{z}_b$, and the a_2

Table 5.1: Spatial Fourier Decomposition of Planar Surface Optic Flow and Linearizations about the Hover Equilibrium

Mode	Planar Surface Geometry	Linearization ($\boldsymbol{x}_0^h$)
a_0	$-\sqrt{2}\dot{\phi} - \frac{\sqrt{2}}{4(z+h)}\ (\dot{x}_b\cos\theta - \dot{z}_b\sin\theta)$	$-\sqrt{2}\dot{\phi} + \frac{1}{2\sqrt{2}h}\dot{x}_b$
a_1	$\frac{2}{3\pi(z+h)}\left[\dot{x}_b\sin\theta\cos\theta + \dot{z}_b(\cos^2\theta - 2)\right]$	$-\frac{2}{3\pi h}\dot{z}_b$
b_1	$\frac{2}{3\pi(z+h)}\left[\dot{x}_b(\cos^2\theta + 1) - \dot{z}_b\sin\theta\cos\theta\right]$	$\frac{4}{3\pi h}\dot{x}_b$
a_2	$\frac{1}{4(z+h)}\ (\dot{x}_b\cos\theta + \dot{z}_b\sin\theta)$	$\frac{1}{4h}\dot{x}_b$
b_2	$\frac{1}{4(z+h)}\ (-\dot{x}_b\sin\theta + \dot{z}_b\cos\theta)$	$\frac{1}{4h}\dot{z}_b$

signal is proportional to the lateral velocity $\dot{x}_b$ only. In this case we cannot expect to locally stabilize (5.2) with these three signals, but rather the pitch orientation ϕ is required for full state feedback. Insects possess additional sensors that can provide an estimate of ϕ, namely the *ocelli* which provide an estimate of horizon orientation [65], [61], as well as the *halteres* which are small biological gyroscopes that measure pitch rate through sensing or coriolis forces that could be integrated for pitch orientation [44], [45]. For our analysis we will assume ϕ to be measurable and will demonstrate a stable hover response utilizing the a_0, a_1 and a_2 spatial harmonics of optic flow.

5.1.1 Local Asymptotic Stability Analysis

As in the previous chapters, the intent is to show feasibility of the proposed output feedback methodology, and hence a linearized control design that guarentees local asymptotic stability of the hover equilibrium is discussed. Introducing the state definitions $v_x = \dot{x}$ and $v_z = \dot{z}$, rewriting the three independent signals a_0, a_1, and a_2 in terms of inertial states $\boldsymbol{x} = (v_x, v_z, \phi, \dot{\phi})$, and computing their respective linearizations along $\boldsymbol{x}_0 = (0,0,0,0)$, we form the observation equation $\boldsymbol{y} = C\boldsymbol{x}$:

$$\begin{pmatrix} y_{a_0} \\ y_{a_1} \\ y_{a_2} \end{pmatrix} = \begin{pmatrix} -\frac{1}{2\sqrt{2}h} & 0 & 0 & -\frac{1}{\sqrt{2}} \\ 0 & -\frac{2}{3\pi h} & 0 & 0 \\ \frac{1}{4h} & 0 & 0 & 0 \end{pmatrix} \begin{pmatrix} v_x \\ v_z \\ \phi \\ \dot{\phi} \end{pmatrix}. \tag{5.3}$$

Introducing the following input definitions

$$\begin{aligned} u_1 &= \frac{1}{m}(F_s + F_p) - g \\ u_2 &= \frac{r_0}{J}(F_s - F_p), \end{aligned} \tag{5.4}$$

and assuming small states and control inputs, the linearized equations of motion for the above equilibrium hover trajectory become

$$\begin{aligned} \dot{v}_x &= -g\phi \\ \dot{v}_z &= u_1 \\ \ddot{\phi} &= u_2. \end{aligned} \tag{5.5}$$

Vertical Velocity Control

In the linearization (5.5) the v_z dynamics and the lift input u_1 are decoupled from the v_x and ϕ dynamics and the torque input u_2. In order to stabilize the vertical velocity dynamics, we would like to have access to an estimate of v_z. In this case we can utilize the a_1 signal. With the choice of a static gain K_{11}^a, the vertical velocity control becomes

$$u_1 = K_{11}^a a_1, \tag{5.6}$$

hence $u_1 = \langle \dot{Q}, F_{u_1} \rangle_w$, corresponding to the motion sensitivity function

$$F_{u_1}(\beta) = K_{11}^a \cos\beta. \tag{5.7}$$

To leading order, this force control input is

$$u_1 = -\frac{2K_{11}^a}{3\pi h} v_z. \tag{5.8}$$

Therefore, with the appropriate choice of gain K_{11}^a we can arbitrarily place the closed loop eigenvalue in the left-half plane, guaranteeing local stability of the vertical velocity dynamics of the nonlinear system.

Lateral Velocity and Pitch Control

In (5.5) the lateral speed v_x dynamics are coupled to pitch through the $g\phi$ term, and therefore, even though we do not have an available input in lateral thrust we can utilize the torque input to stabilize both the ϕ and v_x dynamics. In order to stabilize this coupled system, we require estimates of the lateral velocity v_x, the pitch rate $\dot{\phi}$, and the pitch attitude ϕ. Utilizing the a_0 and a_2 signals, we can obtain $\dot{\phi}$ and v_x since to leading order we have

$$\dot{\phi} \quad = \quad -\left(\frac{\sqrt{2}}{2} y_{a_0} + y_{a_2}\right) \tag{5.9}$$

To add rotational stiffness, we assume an attitude ϕ measurement is available through other sensory modalities, as described in Section 5.1. The resulting torque control input is

$$u_2 \quad = \quad -\frac{\sqrt{2}}{2} K^a_{20} a_0 - K^a_{22} a_2 + K_\phi \phi, \tag{5.10}$$

and hence

$$u_2 \quad = \quad \langle \dot{Q}, F_{u_2} \rangle_w + K_\phi \phi \tag{5.11}$$

corresponding to the motion sensitivity function

$$F_{u_2}(\beta) \quad = \quad -\frac{\sqrt{2}}{2} K^a_{20} - K^a_{22} \cos 2\beta. \tag{5.12}$$

To leading order, this torque control law is

$$u_2 \quad = \quad \frac{1}{2h}(K^a_{20} - K^a_{22}) v_x + K_\phi \phi + K^a_{20} \dot{\phi}. \tag{5.13}$$

With this choice of torque control, the characteristic equation for the linearized closed loop dynamics is

$$s^3 - K^a_{20} s^2 - K_\phi s - \frac{g(K^a_{22} - K^a_{20})}{2h} \quad = \quad 0. \tag{5.14}$$

The natural dynamics (5.5) contain only inertial terms, and therefore to stabilize the attitude response we require $K_\phi < 0$ and $K^a_{20} < 0$, and to stabilize the lateral velocity we

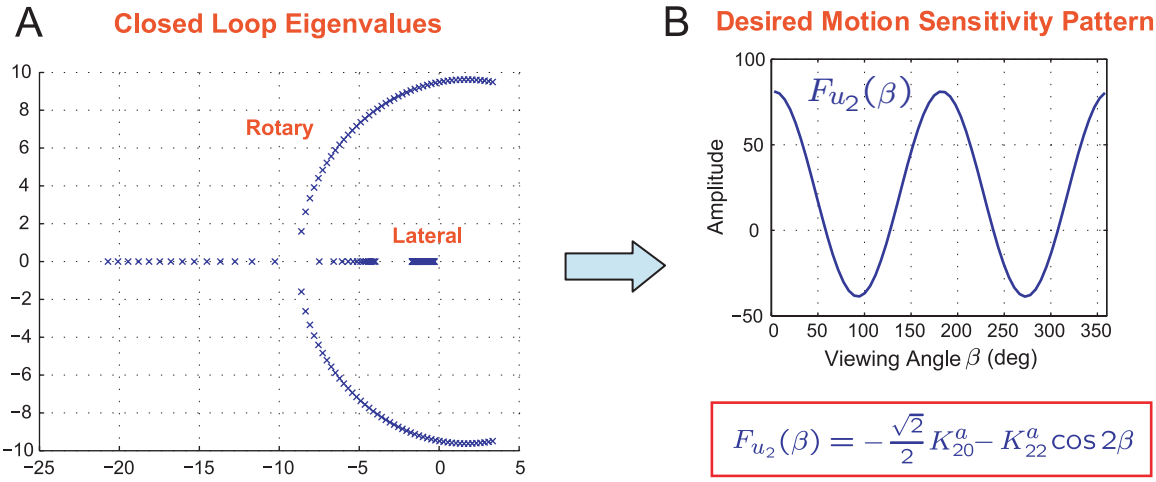

Figure 5.2: Connections between closed loop rotorcraft behavior (eigenvalues) and retinal motion sensitivity shape. (A) Root locus plot for $K_\phi = -90.0$, $K^a_{22} = -30.0$, and $-25 \leq K^a_{20} \leq 5$. (B) Once the desired closed loop eigenvalues (solutions to (5.14)) are selected, the shape of the motion sensitivity function is determined by the coefficients of the characteristic polynomial.

require $K^a_{22} - K^a_{20} < 0$. An example plot of the closed loop eigenvalues is shown in Figure 5.2.

5.1.2 Simulations of Hover Stabilization

Simulations were constructed based on the full nonlinear planar flight dynamics (4.26) to study the performance of the proposed WFI-based control methodology for hover in general environments composed of surface landscapes with obstacles. A spatially-discrete WFI processing model was used, modeled after the simulation environment described in Section 4.2.3. Environments were defined as bitmaps, and the instantaneous optic flow was computed by estimating the depth at the current position and orientation at 60 equally-spaced circumferential points and combining it with the current kinematics according to the rotorcraft version of (4.20). WFI outputs are generated at each time instant by taking the discrete inner product of the instantaneous optic flow with weighting functions corresponding to F_{u_1} and F_{u_2}. The WFI output gains used in the simulation were chosen based on the the performance index of maximizing the bandwidth of the slow (altitude) flight mode in the linearized closed loop system (5.14). Figure 5.3 plots the path of the vehicle along with the time traces of various kinematic states and control outputs for a perfectly flat surface. In this case the closed form expressions for the WFI outputs were computed and used in

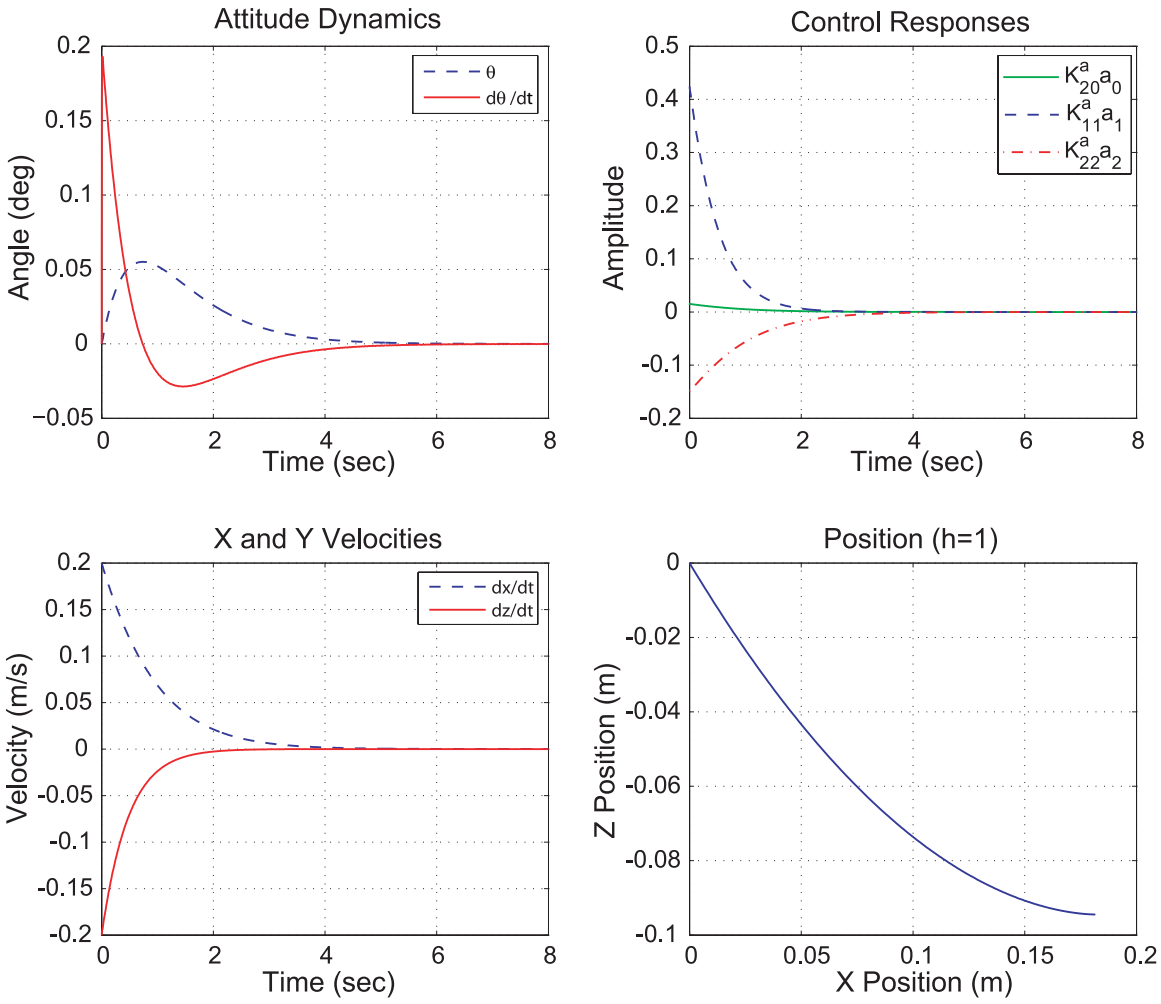

Figure 5.3: Simulations of WFI-based hovering behavior for an initial velocity $(v_x, v_y) = (0.2, -0.2)$ m/s over a flat surface.

simulation. For comparison purposes, Figure 5.4 plots the same information for a textured surface with obstacles.

5.2 Forward Flight Stabilization Methodology

In this section we consider the interpretation of WFI outputs in the context of maintaining a trajectory with a forward reference velocity v_0, fixed height h, and pitch orientation $\phi = 0$ with respect to the ground. If we assume a nearness function (3.8) describing a planar surface geometry, we can explicitly compute the spatial Fourier harmonics of the resulting optic flow in terms of kinematic variables $\boldsymbol{x} = (\dot{x}_b, z, \dot{z}_b, \phi, \dot{\phi})$ (Table 5.2). These signals contain information with respect to general pitch and altitude perturbations from a

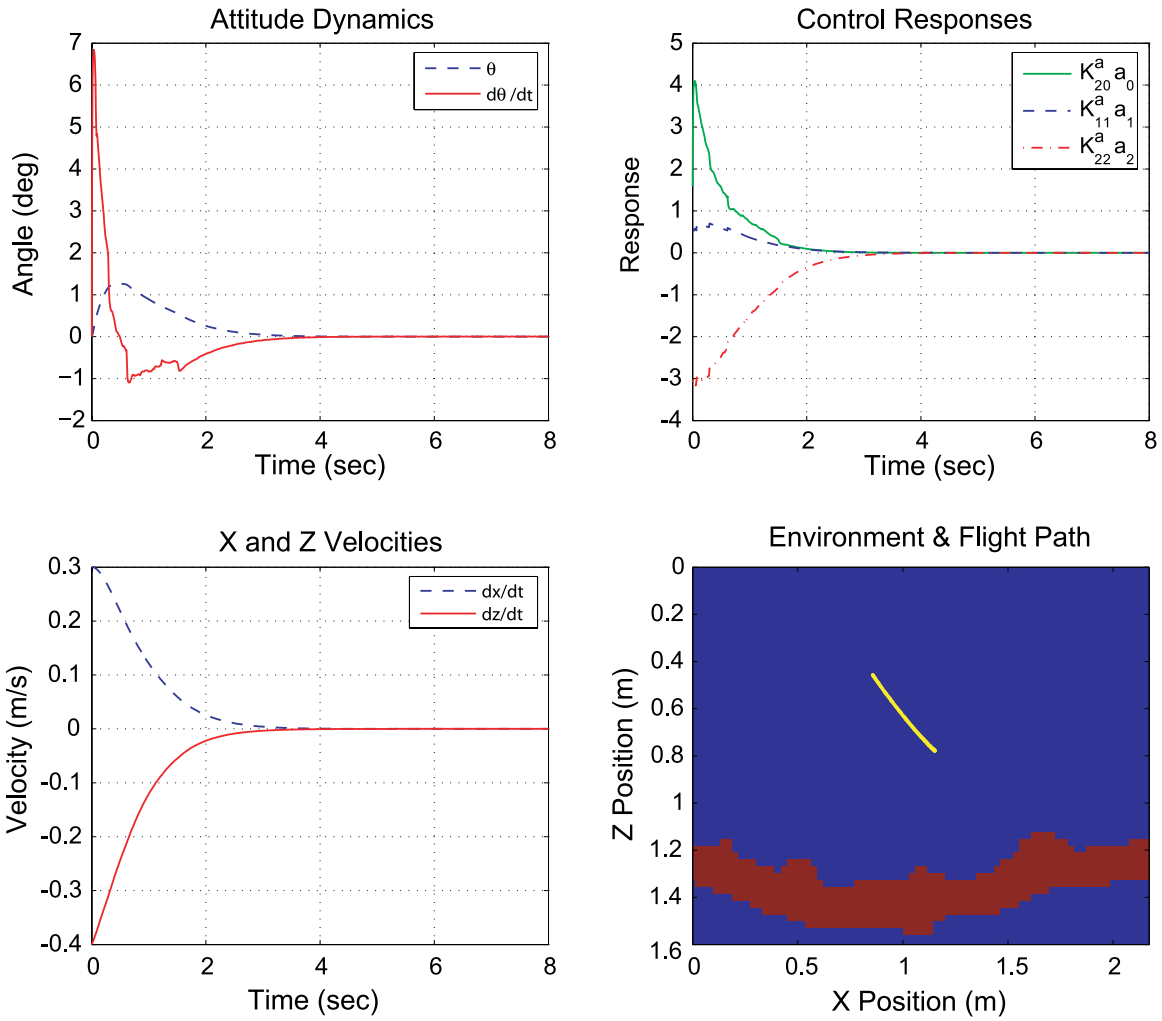

Figure 5.4: Simulations of WFI-based hovering behavior for an initial velocity $(v_x, v_y) = (0.3, -0.4)$ m/s over a textured surface.

balanced nearness function (Figure 5.1B), composed of a fundamental sine harmonic B_1 and DC and even (negative) cosine harmonics $\{A_0, A_k, k = 2, 4, \ldots\}$. Table 5.2 also shows their linearization $y(\boldsymbol{x}) = y(\boldsymbol{x}_0) + \sum_i \frac{\partial y}{\partial x_i}(\boldsymbol{x}_0)\ (x_i - x_{0i})$ with respect to the reference trajectory $\boldsymbol{x}_0 = (v_0, 0, 0, 0, 0)$. To leading order, we find that the a_0, b_1, and a_2 signals contain state coupling between $\dot{x}_b$ and z, due to the $1/(z+h)$ dependence in the spatial harmonics of the nearness function that contributes a first order term that is proportional to z. In addition, the a_1 and b_2 modes contain coupling between ϕ and $\dot{z}_b$. In this case we cannot expect to be able to arbitrarily place closed loop eigenvalues since at best we have constrained state feedback.

In the following we will introduce a nested loop controller, based on the a_0, a_1, and

Table 5.2: Spatial Fourier Decomposition of Planar Surface Optic Flow and Linearizations about the Forward Flight Equilibrium

Mode	Planar Surface Geometry	Linearization ($\boldsymbol{x}_0$)
a_0	$-\sqrt{2}\dot{\phi} - \frac{\sqrt{2}}{4(z+h)}\ (\dot{x}_b\cos\theta - \dot{z}_b\sin\theta)$	$-\frac{1}{\sqrt{2}}\left[2\dot{\phi} + \frac{1}{2h}\left(\dot{x} - \frac{v_0}{h}z\right)\right]$
a_1	$\frac{2}{3\pi(z+h)}\left[\dot{x}_b\sin\theta\cos\theta + \dot{z}_b(\cos^2\theta - 2)\right]$	$\frac{2}{3\pi h}\left(v_0\phi - \dot{z}_b\right)$
b_1	$\frac{2}{3\pi(z+h)}\left[\dot{x}_b(\cos^2\theta + 1) - \dot{z}_b\sin\theta\cos\theta\right]$	$\frac{4}{3\pi h}\left(\dot{x}_b - \frac{v_0}{h}z\right)$
a_2	$\frac{1}{4(z+h)}\left(\dot{x}_b\cos\theta + \dot{z}_b\sin\theta\right)$	$\frac{1}{4h}\left(\dot{x}_b - \frac{v_0}{h}z\right)$
b_2	$\frac{1}{4(z+h)}\left(-\dot{x}_b\sin\theta + \dot{z}_b\cos\theta\right)$	$-\frac{1}{4h}\left(v_0\phi - \dot{z}_b\right)$

a_2 signals, that stabilizes the x and ϕ dynamics and a separate altitude controller that stabilizes the z dynamics that utilizes the a_2 signal. It is important to note that since we are attempting exact altitude tracking for the forward flight case, we will need an independent measurement of forward speed (or altitude) as the optic flow information is only a relative speed/depth measure [37]. In the obstacle avoidance problem in Chapter 4, we did not experience this difficulty with the relative nature of the optic flow measurement since the goal of the control system was to navigate between obstacles, not maintain a prescribed distance from any one obstacle in particular (in this case a surface).

5.2.1 Local Asymptotic Stability Analysis

As in previous section, the intent is to show feasibility of the proposed output feedback methodology, and hence a linearized control design which guarentees local asymptotic stability of the equilibrium point in the nonlinear system is discussed. Rewriting the three independent signals a_0, a_1, and a_2 in terms of inertial states $\boldsymbol{x} = (\dot{x}, z, \dot{z}, \phi, \dot{\phi})$, and computing their respective linearizations along $\boldsymbol{x}_0 = (v_0, 0, 0, 0, 0)$, we form the observation

equation $\boldsymbol{y} = C\boldsymbol{x}$:

$$\begin{pmatrix} y_{a_0} \\ y_{a_1} \\ y_{a_2} \end{pmatrix} = \begin{pmatrix} -\frac{1}{2\sqrt{2}h} & \frac{v_0}{2\sqrt{2}h^2} & 0 & 0 & -\sqrt{2} \\ 0 & 0 & -\frac{2}{3\pi h} & \frac{4v_0}{3\pi h} & 0 \\ \frac{1}{4h} & -\frac{v_0}{4h^2} & 0 & 0 & 0 \end{pmatrix} \begin{pmatrix} \dot{x} \\ z \\ \dot{z} \\ \phi \\ \dot{\phi} \end{pmatrix}. \tag{5.15}$$

Introducing the following input definitions

$$\begin{aligned} u_1 &= \frac{1}{m}(F_s + F_p) - g \\ u_2 &= \frac{r_0}{J}(F_s - F_p), \end{aligned} \tag{5.16}$$

along with the state definition $v = \dot{x} - v_0$, and assuming small states and control inputs, the linearized equations of motion for the above equilibrium flight trajectory become

$$\begin{aligned} \dot{v} &= -g\phi \\ \ddot{z} &= u_1 \\ \ddot{\phi} &= u_2. \end{aligned} \tag{5.17}$$

Altitude Control

In the linearization (5.17) the z dynamics and the lift input u_1 are decoupled from the v and ϕ dynamics and the torque input u_2. Ideally in order to stabilize these altitude dynamics, we would like to have access to estimates of z and $\dot{z}$. However, WFI outputs that are a function of these states are linearly coupled with v, ϕ, and $\dot{\phi}$. Additionally, since the WFI outputs we have available are derived from an optic flow field which is purely a relative measurement of speed/depth, we require either an absolute height or a forward velocity measurement to obtain zero steady-state tracking error in altitude. If we assume the forward velocity $\dot{x}$ is available for feedback, we can decouple the $\dot{x}$ and z states to leading order using the the a_2 output. Therefore, with the choice of static gains K_z and $K_{\dot{z}}$, we obtain stiffness and

damping in the z coordinate with PD feedback of the a_2 signal:

$$u_1 = \left(K_z + K_{\dot{z}}\frac{d}{dt}\right) a_2, \tag{5.18}$$

where $a_2 = \langle \dot{Q}, F_{u_1} \rangle_w$ with $F_{u_1} = \cos 2\beta$. To leading order, this force control input is

$$u_1 = -\frac{K_z v_0}{4h^2} z - \frac{K_{\dot{z}} v_0}{4h^2} \dot{z}. \tag{5.19}$$

Therefore, with the appropriate choice of gains K_z and $K_{\dot{z}}$, one will be able to locally stabilize the altitude dynamics of the nonlinear system.

Pitch Control

In (5.17) the forward speed v dynamics are coupled to pitch through the $g\phi$ term, and therefore, even though we do not have an available input in the thrust direction we can utilize the torque input to stabilize both the ϕ and v dynamics. The only WFI output that is a function of pitch rate $\dot{\phi}$ is the DC component y_{a_0}; however this is also a function of the optic flow imbalance term $\frac{1}{4h}\left(\dot{x} - \frac{v_0}{h} z\right)$. To leading order this is proportional to the y_{a_2} output, and therefore the combination yields a pitch rate signal that can be used to add rotational damping:

$$\dot{\phi} = -\left(\frac{\sqrt{2}}{2} y_{a_0} + y_{a_2}\right) \tag{5.20}$$

To add rotational stiffness, we require feedback of the y_{a_1} output, which unfortunately is also a function of $\dot{z}$. With the appropriately signed gain to provide a stabilizing stiffness, this term will also add positive altitude damping. However, it will still be possible to stabilize this inner loop combination using the feedback

$$u_2 = K_\phi a_1 - K_{\dot{\phi}}\left(\frac{\sqrt{2}}{2} a_0 + a_2\right), \tag{5.21}$$

and hence $u_2 = \langle \dot{Q}, F_{u_2} \rangle_w$, corresponding to the motion sensitivity function

$$F_{u_2}(\beta) = -\frac{\sqrt{2}}{2} K_{\dot{\phi}} + K_\phi \cos\beta - K_{\dot{\phi}} \cos 2\beta. \tag{5.22}$$

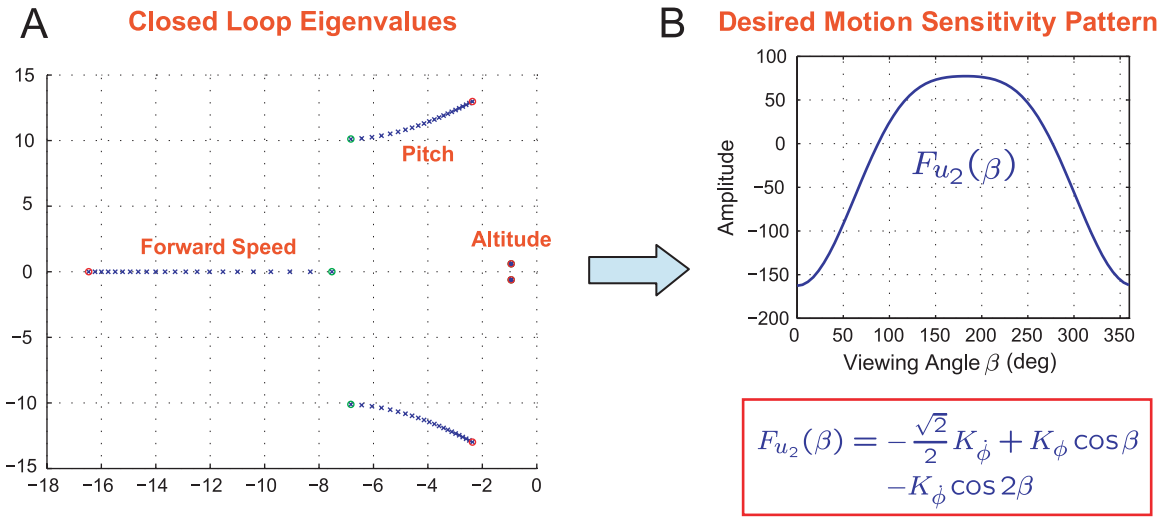

Figure 5.5: Connections between closed loop pitch-altitude behavior (eigenvalues) and retinal motion sensitivity shape. (A) Root locus plot for $K_\phi = -140.0$, $K_{\dot{\phi}} = 5.0$, $K_z = 10.0$, $K_{\dot{z}} = 15.0$, and $27 \leq K_v \leq 70$. (B) Once the desired closed loop eigenvalues (solutions to (5.26)) are selected, the shape of the motion sensitivity function is determined by the coefficients of the characteristic polynomial.

To leading order, this torque control law is

$$u_2 = -\frac{2K_\phi}{3\pi h}\dot{z} + \frac{4K_\phi v_0}{3\pi h}\phi - K_{\dot{\phi}}\dot{\phi}. \tag{5.23}$$

Forward Speed Regulation

We have assumed in the design of the altitude control (force) input u_1 (5.18) that a measurement of forward velocity $\dot{x}$ is available for feedback. Therefore, in order to regulate the v dynamics, the torque input (5.21) requires an additional term $K_v(\dot{x} - v_0)$ composed of the forward velocity and a reference v_0:

$$u_2 = \langle \dot{Q}, F_{u_2} \rangle_w + K_v v. \tag{5.24}$$

Linearized Closed Loop Dynamics

With these choices of control inputs, we can write down the linearized constrained state

feedback equation $\boldsymbol{u} = K\boldsymbol{x}$ where $\boldsymbol{u} = (u_1, u_2)$, $\boldsymbol{x} = (v, z, \dot{z}, \phi, \dot{\phi})$, and

$$K = \begin{pmatrix} 0 & -\frac{K_z v_0}{4h^2} & -\frac{K_{\dot{z}} v_0}{4h^2} & 0 & 0 \\ K_v & 0 & -\frac{2K_\phi}{3\pi h} & \frac{4K_\phi v_0}{3\pi h} & -K_{\dot{\phi}} \end{pmatrix}. \tag{5.25}$$

This results in the closed loop chracteristic equation

$$\begin{aligned} s^5 + \left(\frac{v_0}{4h^2}K_{\dot{z}} - K_{\dot{\phi}}\right)s^4 + \left(\frac{v_0}{4h^2}K_z - \frac{4v_0}{3\pi h}K_\phi + \frac{v_0}{4h^2}K_{\dot{\phi}}K_{\dot{z}}\right)s^3 \\ + \left(gK_v + \frac{v_0}{4h^2}K_z K_{\dot{\phi}} - \frac{v_0^2}{3\pi h^3}K_\phi K_{\dot{z}}\right)s^2 \\ + \left(\frac{v_0 g}{4h^2}K_v K_{\dot{z}} - \frac{v_0^2}{3\pi h^3}K_z K_\phi\right)s + \frac{v_0 g}{4h^2}K_v K_z = 0. \end{aligned} \tag{5.26}$$

The natural dynamics (5.17) contain only inertial terms, and therefore to stabilize the altitude response we require $K_z > 0$ and $K_{\dot{z}} > 0$, and to stabilize the pitch response we require $K_\phi < 0$, and $K_{\dot{\phi}} > 0$, and $K_v > 0$. An example plot of the closed loop eigenvalues is shown in Figure 5.5.

5.2.2 Simulations of General Terrain Navigation

Simulations were constructed based on the full nonlinear planar flight dynamics (4.26) to study the performance of the proposed WFI-based control methodology in general environments composed of surface landscapes with obstacles. A spatially-discrete WFI processing model was used, modeled after the simulation environment described in Section 4.2.3. Environments were defined as bitmaps, and the instantaneous optic flow was computed by estimating the depth at the current position and orientation at 60 equally-spaced circumferential points and combining it with the current kinematics according to the rotorcraft version of (4.20). WFI outputs are generated at each time instant by taking the discrete inner product of the instantaneous optic flow with weighting functions corresponding to F_{u_1} and F_{u_2}. The WFI output gains used in the simulation were chosen based on the the performance index of maximizing the bandwidth of the slow (altitude) flight mode in the linearized closed loop system (5.26). Figure 5.6 plots the path of the vehicle along with the time traces of various kinematic states and control outputs for an initial height of $h = 1$ m above a flat surface, Figure 5.7 and Figure 5.8 plot the same for a landscape with a hill and with various obstacles. The rotorcraft was able to successfully navigate landscapes with

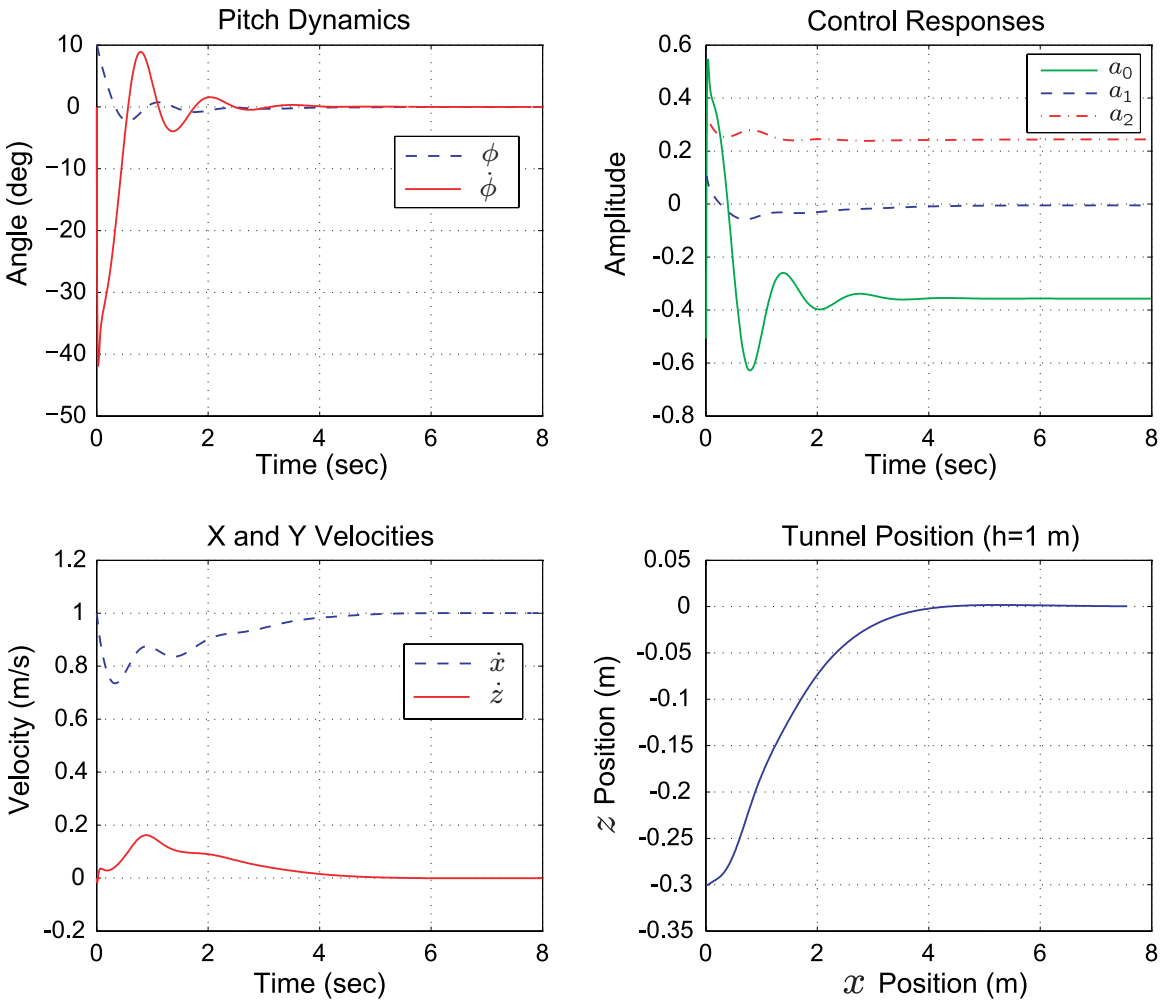

Figure 5.6: Simulations of WFI-based pitch-altitude stabilization and terrain following over a flat surface for $h = 1$ m.

various sizes and shapes of obstacles, warranting further work to completely characterize the stability and performance of this control methodology.

5.3 Comparisons with Previous Work

Optic flow cues have been previously utilized, in conjunction with other sensory modalities, to accomplish altitude regulation and terrain following. In the 3 DOF tethered vertical flight experiments of [47], the optic flow over a patch of the visual space that extended over a portion of the frontal and downward regions is computed and averaged, then compared to a reference averaged optic flow, corresponding to a pre-programmed altitude and ground-speed. The difference produces a new reference altitude, and terrain following is achieved

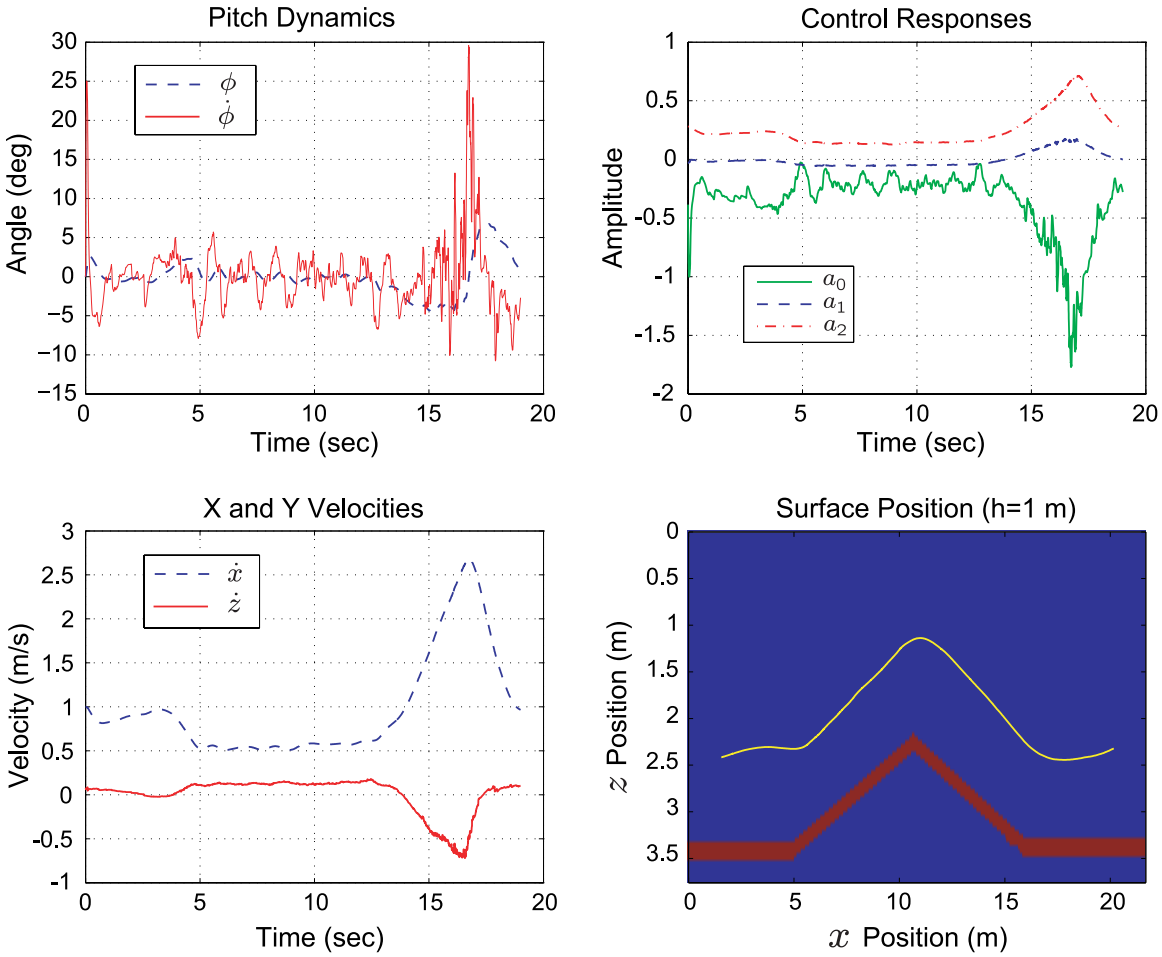

Figure 5.7: Simulations of WFI-based terrain following and pitch-altitude stabilization of a forward reference trajectory over a landscape with a hill.

by adjusting the vertical thrust such that the computed optic flow average is adjusted to the reference optic flow average. The pitch (attitude) and forward airspeed are regulated via a PID control loop that utilizes inertial sensory information.

Similarly in the free-flying experimental platforms of [65], altitude regulation and terrain following were demonstrated. An optic flow sensor was placed on the ventral part of the vehicle covering a downward patch of the ground. The optic flow was computed using an interpolation algorithm [57], and interpreted based on the the motion parallax formulation (4.44) by [68], as described in Section 4.4. It is assumed that the components of the optic flow due to rotary and (in this case) vertical motion are negligible, hence the resulting measured optic flow can be averaged to generate a signal, representing the spatial imbalance, which is reflective the height above ground if the forward speed of the aircraft is known. In this

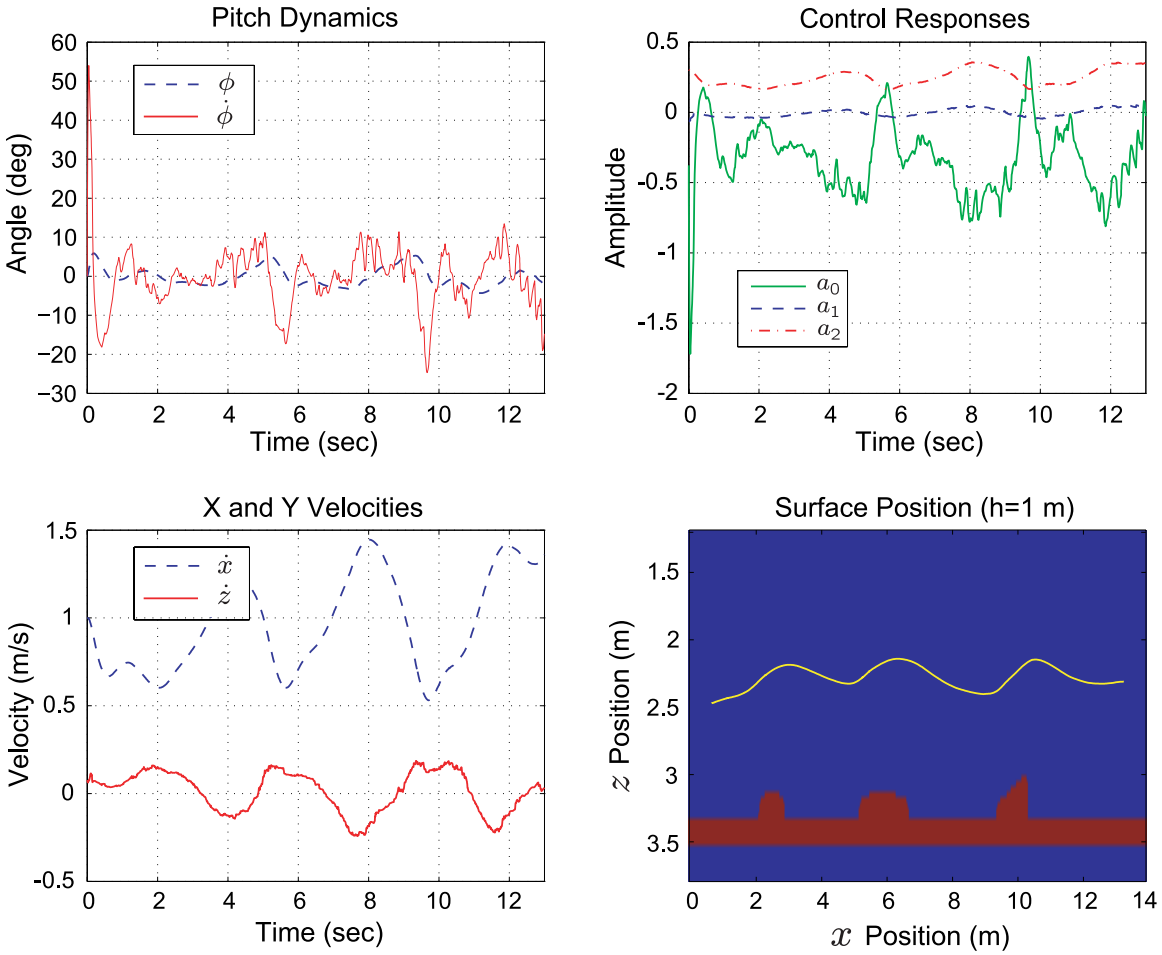

Figure 5.8: Simulations of WFI-based terrain following and pitch-altitude stabilization of a forward reference trajectory over a landscape with various obstacles.

implementation the aircraft was stabilized using a complete suite of inertial sensors.

Based on the analysis in this chapter, we conclude the terrain following applications to date have only utilized a limited part of the information that is available from optic flow. Through the LPTC-inspired wide-field integration approach developed in this thesis, additional information is available that can be used to significantly improve closed loop stability and performance, as well as simplify sensory and actuation requirements. Specifically, the optic flow altitude imbalance due to a textured surface can be directly estimated from a $F(\gamma) = \cos 2\gamma$ motion sensitivity function, which eliminates the need for actively removing the rotation term from the DC (averaged) component, or assuming it is negligible, and allows for the possibility of injecting rotational damping about the pitch axis using the $F(\gamma) = 1/\sqrt{2}$ motion sensitivity function. Additionally, the pitch orientation (attitude)

with respect to a textured surface can be determined using a $F(\beta) = \cos\beta$ motion sensitivity function, which can be used to add rotational stiffness to the loop. However, the ability to extract pitch orientation information did not extend to the hover equilibrium behavior as forward speed is required to generate optic flow with pitch orientation information.

These conclusions become important when extending optic flow stabilization and navigation methodologies to the planar hover and flight problems posed in Sections 5.1 and 5.2. This work presents a methodology which demonstrates planar vertical 3 DOF flight stabilization and terrain following behaviors utilizing a minimum of sensory information from other modalities, unlike comparable implementations which use optic flow as an indicator of range to the ground but require significantly more inertial sensory information in order to stabilize flight as well as kinematic motion constraints in order to utilize the optic flow measurements. Specifically, in the methodology presented in this chapter, only an outside measurement of forward speed was required to achieve zero steady state error in tracking an altitude reference, and only an outside measurement of pitch orientation was required to stabilize the hover equilibrium.

Chapter 6

Conclusions and Future Work

In this thesis a rigorous characterization of the information available from wide-field integration of retinal image flow for environments with non-homogeneous, non-uniform spatial distributions of objects was performed. A spatial inner product model for LPTCs was presented and analyzed with an emphasis on extraction of behaviorally-relevant optic flow cues by selection of appropriate retinal motion sensitivity functions. A static output feedback control structure was proposed, where force and torque inputs are computed (as would be the case with LPTCs) by taking the inner product of the instantaneous optic flow with pre-determined sensitivity functions for each required control input. Sensitivity function shape was then tied to behavior (closed loop eigenvalues) via a local asymptotic stability analysis.

Through balancing various spatial harmonics of optic flow, we can obtain generalized feedback terms that are functions of rotational and lateral stiffness with respect to a balanced nearness function, as well as terms that contain rotational, lateral, and forward velocities, which are useful for designing closed loop stabilization and performance. The computationally efficient wide-field integration outputs require no direct estimation of depth or kinematic states, nor any prior knowledge of the environment. It is shown that this methodology has sufficient complexity to give rise to the centering (obstacle avoidance) and clutter (forward speed regulation) responses exibited in experiments with insects (Section 1.3). Additional behaviors for pitch-altitude rotorcraft dynamics were demonstrated, including hovering and terrain following tasks. Hence, the global optic flow cues extracted by LPTCs, which are generalized combinations of speed/depth, provide control-relevant information, as well as a novel methodology for utilizing optic flow sensory information in autonomous robotic navigation and control applications.

These successful results suggest two future avenues for research, including experimental validation and demonstration of embedded planar optic flow sensors, as well as an extension of this analysis approach to 3-D environments and vehicles with 6 DOF dynamics. We provide some additional results along these lines in the remainder of the chapter.

6.1 Experimental Validation of WFI-Based Planar Navigation and Control

As an initial demonstration and experimental verification of the hovercraft navigation methodology proposed in Section 4.3.2, the torque and forward force control laws were implemented on a vehicle (Figure 6.1A) from the Caltech Multi-Vehicle Wireless Testbed (MVWT) [10]. The vehicle laptops receive sensory input directly over a wireless network and generate control (force) commands to the fans (Figure 6.1B). In this arrangement, the inertial configuration $\mathbf{q} = (x, y, \theta)$ of the vehicle is estimated from an overhead vision system, and the vehicle velocity $\dot{\mathbf{q}} = (\dot{x}, \dot{y}, \dot{\theta})$ is computed from the configuration estimates. At the time of implementation, a planar optic flow sensor was under construction, but not available. However, if we assume a planar tunnel environment (Section 3.3.1), we can explicitly compute the force and torque control inputs, assuming estimates of the current vehicle position $\mathbf{q}$ and velocity $\dot{\mathbf{q}}$ are available. In this case, as in (4.31) and (4.34) the force and torque inputs are

$$\begin{aligned} u_1 &= K_{11}^b (N v_0 - b_1) \\ u_2 &= K_{20}^a a_0 + K_{21}^a a_1 + K_{22}^a a_2, \end{aligned} \tag{6.1}$$

where the spatial harmonics for tunnel optic flow, in terms of inertial coordinates ($\mathbf{q}$,$\dot{\mathbf{q}}$), are given by

$$\begin{aligned} b_1(\mathbf{q}, \dot{\mathbf{q}}) &= \frac{4a}{3\pi(a^2 - y^2)} (2\dot{x}\cos\theta - \dot{y}\sin\theta) \\ a_0(\mathbf{q}, \dot{\mathbf{q}}) &= -\sqrt{2}\dot{\theta} + \frac{y}{\sqrt{2}(a^2 - y^2)}\, \dot{x} \\ a_1(\mathbf{q}, \dot{\mathbf{q}}) &= \frac{4a}{3\pi(a^2 - y^2)} (2\dot{x}\sin\theta - \dot{y}\cos\theta) \\ a_2(\mathbf{q}, \dot{\mathbf{q}}) &= -\frac{y}{2(a^2 - y^2)} \left(\dot{x}\cos 2\theta + \dot{y}\sin 2\theta\right). \end{aligned} \tag{6.2}$$

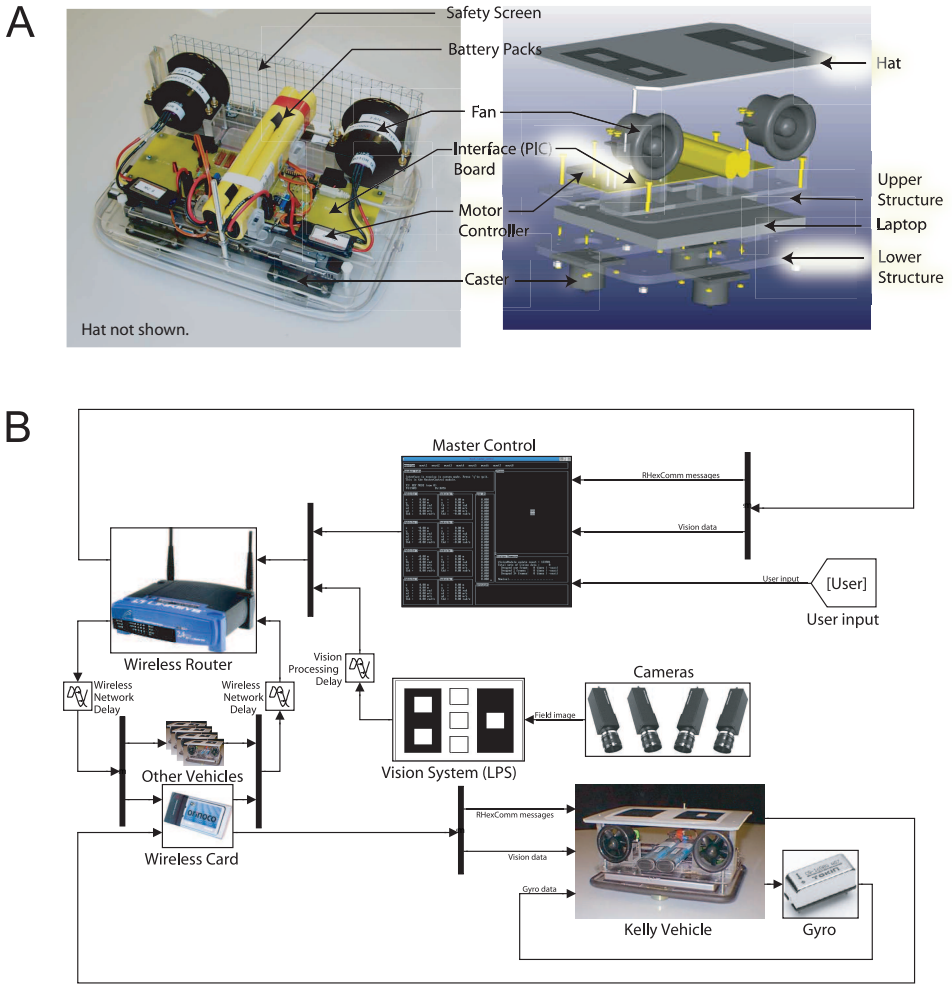

Figure 6.1: Experimental setup for centering and clutter response verification. (A) The Kelly vehicle, composed of a laptop on three castor wheeles, two fans, and associated electronics. (B) Structure of the MVWT experiment: Vehicles receive wireless input and output thrust commands to their fans. An overhead vision system measures the vehicle configuration.

A tunnel width of $a = 1.5$ meters was assumed along with a reference velocity of $v_0 = 0.4$ m/s. The hovercraft was started at rest in a position with a lateral and rotary displacement. Figure 6.2 plots the measured states $\theta(t)$, $y(t)$, $\dot{x}(t)$, and $\dot{y}(t)$ against the simulation results. The vehicle path $x(t)$ versus $y(t)$ is also plotted against the prediction from the simulation. The experimental results agree well with the simulation that used the methodology described in Section 4.3.2 to design the gains.

These results are a promising first step towards practical real-time implementation of embedded optic flow sensory systems for autonomous navigation and control. To further this goal, a collaborative effort has been initiated with Tanner Research, Inc., to develop

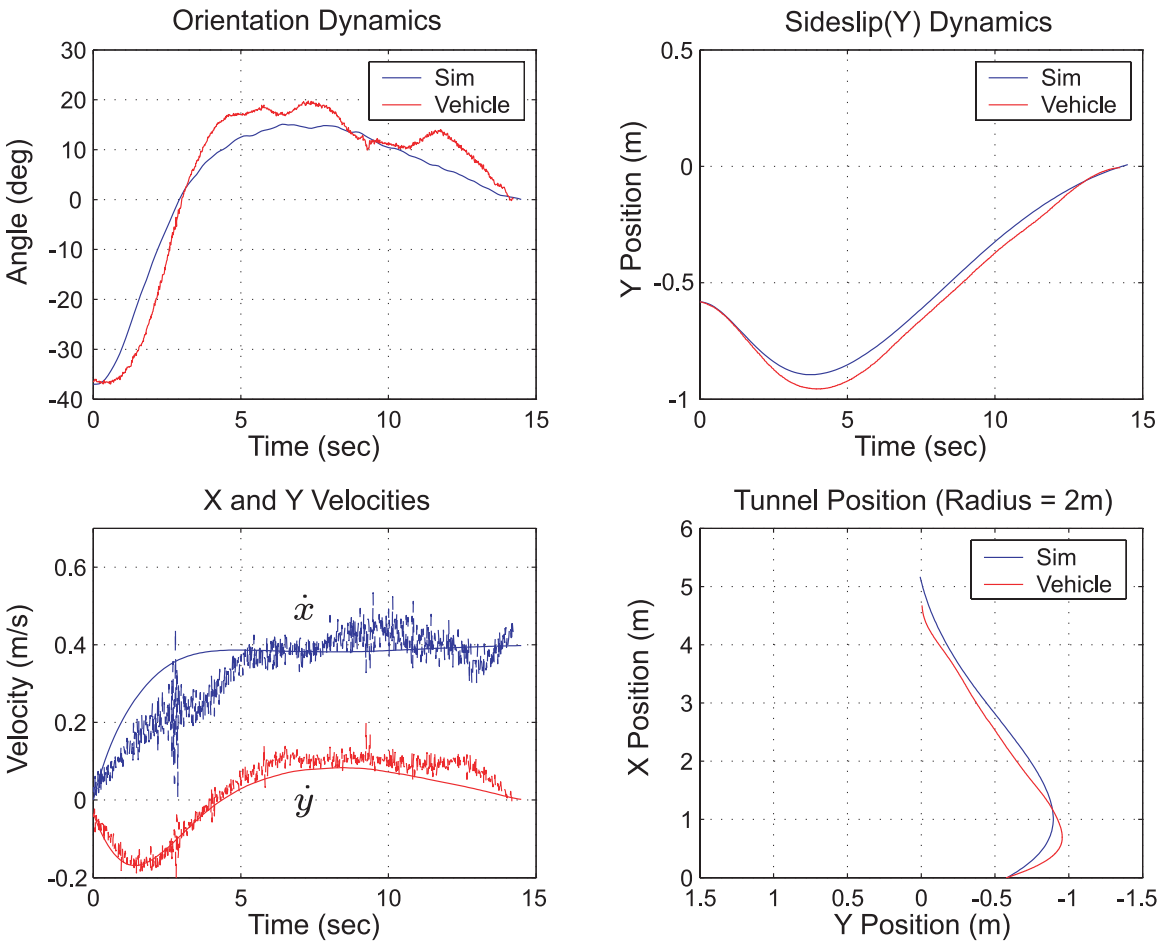

Figure 6.2: Experimental validation of WFI-based centering and clutter response behavior for planar hovercraft versus simulation.

an analog VLSI chip that will demonstrate the feasibility of navigation using wide-field motion detection and integration. Through several DoD-funded projects, Tanner Research has developed a silicon version of an optic flow estimation array, based on principles of insect neurobiology, that is exceptionally robust to stimulus characteristics unrelated to motion. Through this highly synergistic collaboration that combines Tanner's electronic design and packaging capabilities with the advances in bio-inspired control methodologies described herein, we seek to significantly improve the capability of autonomous UAVs to navigate extensive near-ground obstacle fields.

6.2 Extensions to 3-D Environments with 6 DOF Dynamics

By coupling planar (1-D) optic flow information to 3 DOF dynamics, we were able to develop a remarkable amount of insight for designing optic flow based navigation and control methodologies for planar vehicles. Given this success, the next logical step in the theory is a generalization of the analysis approach to 3-D environments, i.e., 2-D optic flow fields, coupled with 6 DOF vehicle dynamics. If the analysis presented in this thesis can be successfully extended to the 3-D, 6 DOF case, it will provide a tremendous opportunity to analyze the LPTC receptive field organizations that have already been mapped out by various researchers [32], [42].

In the planar case, we were able to formalize the spatial decomposition performed by LPTCs in $L_2[0, 2\pi]$, the space of square-integrable periodic functions of angle, hence a trigonometric Fouier series was the natural choice for an orthogonal basis. For the more general case, the spherical optic flow equation developed in Chapter 2,

$$\dot{\boldsymbol{Q}}(\gamma, \beta, \mathbf{q}, \dot{\mathbf{q}}) \;\; = \;\; A(\gamma, \beta) \cdot \boldsymbol{\omega} + \mu(\gamma, \beta, \mathbf{q}) \cdot B(\gamma, \beta) \cdot \boldsymbol{v}, \tag{6.3}$$

has two components $\dot{\boldsymbol{Q}} = \dot{Q}_\gamma \;\hat{\boldsymbol{e}}_\gamma + \dot{Q}_\beta \;\hat{\boldsymbol{e}}_\beta$, each of which live in the function space $L_2\left([0, 2\pi] \times [-\frac{\pi}{2}, \frac{\pi}{2}]\right)$. The most general approach would involve utilization of spherical harmonics as the orthogonal basis to decompose (6.3). This analysis approach will definitely be investigated; however since the azimuth and elevation components of (6.3) are tangential and normal to the directions of various control-relevant quantities such as pitch, roll and yaw rates, some initial intuition might be extracted from first examining the individual spherical components. In this case, azimuthal and elevation sensitivities would be modeled as weights $F_i(\gamma, \beta) \in L_2\left([0, 2\pi] \times [-\frac{\pi}{2}, \frac{\pi}{2}]\right)$, and the WFI operation would be represented by a transformation W, representing a spatial inner product over the sphere S^2 with the optic flow kernels $\dot{Q}_\gamma$ and $\dot{Q}_\beta$, which acts on elements $F_i(\gamma, \beta)$ to produce a sensor output signal z_i, and hence

$$W : \; F_i \in L_2\left([0, 2\pi] \times [-\frac{\pi}{2}, \frac{\pi}{2}]\right) \;\mapsto\; z_i \in \mathbb{R}.$$

Therefore, a similar analysis approach as outlined in this thesis could be utilized.

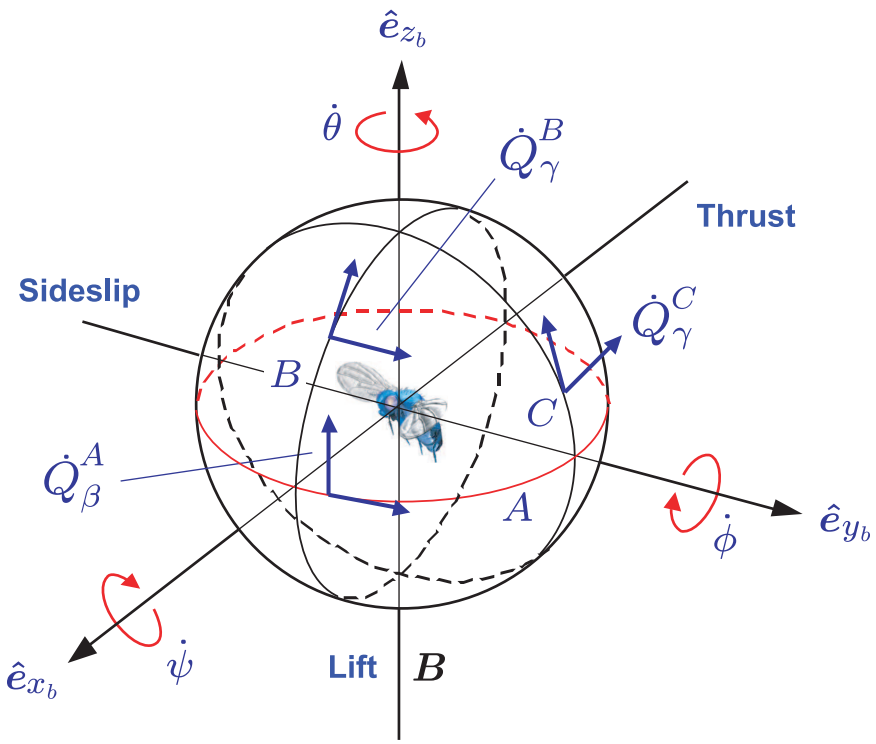

Figure 6.3: Off-axis retinal motion field components $\dot{Q}^A_\beta$, $\dot{Q}^B_\gamma$, and $\dot{Q}^C_\gamma$ for three concentric circular sensor bands A, B, and C.

6.2.1 Off-Axis Retinal Motion Spatial Harmonics

In the analysis of planar retinal motion fields in this thesis the tangential components to planar cross sections through equation (6.3) were examined (Sections 2.3.1 and 2.3.2). The normal, or off-axis, components of the optic flow on these circular retinas were considered to be zero, due to the fact that the kinematics of the vehicles were restricted 3 DOF. If we relax this assumption, the off-axis components become nonzero, and it is useful to consider a sensory arrangement (Figure 6.3) where there are three concentric circular bands, one about the horizon $\beta = 0$ (band A) and one about the two verticals $\gamma = 0, \pi/2$ (bands B, C), coupled to 6 DOF vehicle dynamics.

For band A, the off-axis component $\dot{Q}^A_\beta$ is

$$\dot{Q}^A_\beta(\gamma, 0, \mathbf{q}, \dot{\mathbf{q}}) \quad = \quad -\dot{\psi}\sin\gamma + \dot{\phi}\cos\gamma - \mu(\gamma, 0, \mathbf{q})\ \dot{z}_b, \tag{6.4}$$

and the first several spatial Fourier harmonics are computed in Table 6.1. Note that the notation A^A_k and B^A_k corresponds to the spatial Fourier harmonics of the nearness function for

Table 6.1: Off-Axis Retinal Motion Field Spatial Fourier Decomposition

Mode	$\dot{Q}^A_\gamma$	$\dot{Q}^B_\beta$	$\dot{Q}^C_\beta$
a_0	$-\frac{\dot{z}_b}{\sqrt{2}}A^A_0$	$-\frac{\dot{y}_b}{\sqrt{2}}A^B_0$	$\frac{\dot{x}_b}{\sqrt{2}}A^C_0$
a_1	$\dot{\phi} - \dot{z}_b A^A_1$	$-\dot{\theta} - \dot{y}_b A^B_1$	$-\dot{\phi} + \dot{x}_b A^C_1$
b_1	$-\dot{\psi} - \dot{z}_b B^A_1$	$\dot{\psi} - \dot{y}_b B^B_1$	$\dot{\phi} + \dot{x}_b B^C_1$
a_2	$-\dot{z}_b A^A_2$	$-\dot{y}_b A^B_2$	$\dot{x}_b A^C_2$
b_2	$-\dot{z}_b B^A_2$	$-\dot{y}_b B^B_2$	$\dot{x}_b B^C_2$

the particular band in question. For band A, the nearness function of interest is $\mu(\gamma, 0, \mathbf{q})$, and hence

$$\begin{aligned} A^A_k(\mathbf{q}) &= \frac{1}{\pi}\int_0^{2\pi} \mu(\gamma, 0, \mathbf{q}) \cdot \cos k\gamma \; d\gamma \\ B^A_k(\mathbf{q}) &= \frac{1}{\pi}\int_0^{2\pi} \mu(\gamma, 0, \mathbf{q}) \cdot \sin k\gamma \; d\gamma. \end{aligned} \tag{6.5}$$

Similarly for bands B and C, the off-axis components of the retinal motion field are

$$\dot{Q}^B_\gamma(0, \beta, \mathbf{q}, \dot{\mathbf{q}}) = \dot{\psi}\sin\beta - \dot{\theta}\cos\beta - \mu(0, \beta, \mathbf{q})\; \dot{y}_b \tag{6.6}$$

$$\dot{Q}^C_\gamma(\pi/2, \beta, \mathbf{q}, \dot{\mathbf{q}}) = \dot{\psi}\sin\beta - \dot{\theta}\cos\beta - \mu(\pi/2, \beta, \mathbf{q})\; \dot{y}_b. \tag{6.7}$$

From Table 6.1, we see that the first several spatial harmonics are relatively simple combinations of linear and angular velocities and nearness function spatial harmonics, as opposed to the on-axis harmonics for each respective case. Therefore, if one is able to make progress utilizing the analysis approach presented in previous chapters, this would provide a substantial first step in developing a general theory for retinal image motion based autonomous navigation and flight control of 6 DOF vehicles, i.e., MAV/UAVs, in 3-D environments.

Appendix A

Useful Mathematical Properties of Inner Product Spaces

The space of square-integrable functions over $[0, 2\pi]$, defined as

$$L_2[0, 2\pi] \quad = \quad \left\{ f : [0, 2\pi] \to \mathbb{R} : \int_0^{2\pi} |f(\gamma)|^2 \, d\gamma < \infty \right\},$$

holds significant importance in the analysis presented in this thesis as it is the space where the optic flow $\dot{Q}$, the nearness μ, and, as we will see in this chapter, the retinal motion sensitivities F_i reside. In the following we list several definitions and properties that will be useful in subsequent analysis. For additional detail, see references [1], [46]. Throughout let V denote a linear space over the field $\mathbb{F} = (\mathbb{R}$ or $\mathbb{C})$.

Definition An inner product on a linear space V is a mapping $\langle \cdot, \cdot \rangle : V \times V \to \mathbb{F}$ such that $\forall\, x, y, z \in V$ and $\forall\, \alpha, \beta \in \mathbb{R}$:

(i) $\langle x, x \rangle \geq 0$

(ii) $\langle x, x \rangle = 0 \Rightarrow x = 0$

(iii) $\langle x, y \rangle = \overline{\langle y, x \rangle}$

(iv) $\langle \alpha x + \beta y, z \rangle = \alpha \langle x, z \rangle + \beta \langle y, z \rangle$

Definition An *inner product space* is a linear space V with an inner product $\langle \cdot, \cdot \rangle$ defined on V, and is denoted $(V, \langle \cdot, \cdot \rangle)$.

Remark When refering to topological properties of inner product spaces, this is a reference to the metric defined by $d_2(x, y) = \{\langle x - y, x - y \rangle\}^{1/2}$.

Definition A *Hilbert space* is a complete inner product space.

Definition A maximal orthonormal set B in a Hilbert space H is referred to as an *orthonormal basis* for H.

Theorem A.0.1. Fourier Series Theorem

(i) *A Hilbert space H has a countable orthonormal basis $\{e_n : n \in \mathbb{Z}^+\}$ if and only if it is separable.*

(ii) *(Fourier series expansion) In a separable Hilbert space any $x \in H$ can be written uniquely in the form*

$$x = \sum_n \langle x, e_n \rangle \, e_n$$

Proof. See references [1] and [46]. □

Remark A.0.2

(i) The linear space of Lebesgue square-integrable functions $L_2[0, 2\pi]$, defined on the interval $[0, 2\pi]$, is a Hilbert space under inner product

$$\langle x, y \rangle = \int_0^{2\pi} x(\gamma) \cdot \overline{y(\gamma)} \, d\gamma$$

because $(L_2[0, 2\pi], d_2)$ is complete.

(ii) $L_2[0, 2\pi]$ is a separable Hilbert space [1].

(iii) The orthonormal set

$$\Phi = \{1/\sqrt{2}\} \cup \{\cos n\gamma : n = 1, 2, \ldots\} \cup \{\sin n\gamma : n = 1, 2, \ldots\}$$

is an orthonormal basis for $L_2^r[0, 2\pi]$ under the inner product

$$\langle x, y \rangle_w = \frac{1}{\pi} \int_0^{2\pi} x(\gamma) \cdot y(\gamma) \, d\gamma.$$

Bibliography

[1] G. Bachman, L. Narici, and E. Beckenstein. *Fourier and Wavelet Analysis*. Springer Verlag, New York, 2000.

[2] G.L. Barrows, J.S. Chahl, and M.V. Srinivasan. Biologically inspired visual sensing and flight control. *The Aeronautical Journal*, 107:159–168, 2003.

[3] A. Borst. How do flies land? *Bioscience*, 40:292–299, 1990.

[4] A. Borst and M. Egelhaaf. Principles of visual motion detection. *TINS*, 12:297–306, 1989.

[5] A. Borst and M. Egelhaaf. In vivo imaging of calcium accumulation in fly interneurons as elicited by visual motion stimulation. *Proc. Natl. Acad. Sci., USA*, 89:4139–4143, 1992.

[6] A. Borst and J. Haag. Neural networks in the cockpit of the fly. *J. Comp. Physiol. A*, 188:419–437, 2002.

[7] J.S. Chahl and M.V. Srinivasan. A complete panoramic vision system, incorporating imaging, ranging, and three dimensional navigation. In *Proceedings of the IEEE Workshop on Omnidirectional Vision*, pages 104–111. Hilton Head, South Carolina, 2000.

[8] D. Coombs, M. Herman, T.H. Hong, and M. Nashman. Real-time obstacle avoidance using central flow divergence, and peripheral flow. *IEEE Transactions on Robotics and Automation*, 14:49–59, 1998.

[9] D. Coombs and K. Roberts. Centering behavior using peripheral vision. In *Proceedings of IEEE Conference on Computer Vision and Pattern Recognition*, pages 440–445. New York City, NY, 1993.

[10] Lars Cremean, William Dunbar, David van Gogh, Jason Hickey, Eric Klavins, Jason Meltzer, and Richard M. Murray. The Caltech multi-vehicle wireless testbed. *Conf. on Decision and Control (CDC)*, 2002.

[11] H.J. Dahmen, M.O. Franz, and H.G. Krapp. Extracting egomotion from optic flow: limits of accuracy and neural matched filters. In J.M. Zanker and J. Zeil, editors, *Motion Vision – Computational, Neural and Ecological Constraints*, pages 143–168. Springer, Berlin, Heidelberg, New York, 2001.

[12] C.T. David. Compensation for height in the control of groundspeed by *Drosophila* in a new, barber's pole wind tunnel. *J. Comp. Phisiol.*, 147:485–493, 1982.

[13] Michael H. Dickinson. The initiation and control of rapid maneuvers in fruit flies. *Integr. Comp. Biol.*, 45:274–281, 2005.

[14] A. Duchon. Maze navigation using optical flow. In *Proceedings of the Fourth International Conference on Simulation of Adaptive Behavior*, pages 224–232. Cambridge, MA, 1996.

[15] M. Egelhaaf and A. Borst. Motion computation and visual orientation in flies. *Comp. Biochem. Phisiol.*, 104A:659–673, 1993.

[16] M. Egelhaaf, R. Kern, H. Krapp, J. Kretzberg, R. Kurtz, and A. Warzecha. Neural encoding of behaviourally relevant visual-motion information in the fly. *Trends in Neurosciences*, 25:96–102, 2002.

[17] N. Franceschini, J.M. Pichon, and C. Blanes. From insect vision to robot vision. *Phil. Trans. R. Soc. Lond. B*, 337:283–294, 1992.

[18] M.O. Franz, J.S. Chahl, and H.G. Krapp. Insect-inspired estimation of egomotion. *Neural Computation*, 16:2245–2260, 2004.

[19] M.O. Franz and H.G. Krapp. Wide-field, motion-sensitive neurons and matched filters for optic flow fields. *Biological Cybernetics*, 83:185–197, 2000.

[20] M.O. Franz and H.A. Mallot. Biomimetic robot navigation. *Robotics and Autonomous Systems*, 30:133–153, 2000.

[21] S. Fry, R. Sayaman, and M.H. Dickinson. The aerodynamics of free flight maneuvers in *Drosophila*. *Nature*, 300:495–498, 2003.

[22] M.A. Frye and M.H. Dickinson. Fly flight: A model for the neural control of complex behavior. *Neuron*, 32:385–388, 2001.

[23] V. Gauck and A. Borst. Spatial response properties of contralateral inhibited lobula plate tangential cells in the fly visual system. *J. Comp. Neurol.*, 406:51–71, 1999.

[24] G. Geiger and D.R. Nassel. Visual processing of moving single objects and wide-field patterns in flies: behavioural analysis after laser-surgical removal of interneurons. *Biol. Cybern.*, 44:141–149, 1982.

[25] J.J. Gibson. *The perception of the visual world*. Houghton Mifflin, Boston, 1950.

[26] K.G. Gotz. Optomotorische untersuchung des visuellen systems einiger augenmutanten der fruchtfliege *Drosophila*. *Kybernetik*, 2:77–92, 1964.

[27] K.G. Gotz. Flight control in *Drosophila* by visual perception motion. *Kybernetik*, 9:159–182, 1968.

[28] K.G. Gotz. The optomotor equilibrium of the *Drosophila* navigation system. *J. Comp. Physiol.*, 99:187–210, 1975.

[29] W. Gronenberg and N.J. Strausfeld. Descending neurons supplying the neck and flight motor of diptera: physiological and anatomical characteristics. *J. Comp. Neurol.*, 302:973–991, 1990.

[30] K. Hausen. Monocular and binocular computation of motion in the lobula plate of the fly. *Verh. dt. Zool. Ges.*, 74:49–70, 1981.

[31] K. Hausen. Motion sensitive interneurons in the optomotor system of the fly, part i. the horizontal cells: structure and signals. *Biol. Cybern.*, 45:143–156, 1982.

[32] K. Hausen. Motion sensitive interneurons in the optomotor system of the fly, part ii. the horizontal cells: Receptive field organization and response characteristics. *Biol. Cybern.*, 46:67–79, 1982.

[33] K. Hausen and C. Wehrhahn. Microsurgical lesion of horizontal cells changes optomotor yaw responses in the blowfly *Calliphora erythrocephala*. *Proc. R. Soc. Lond. B*, 219:211–216, 1983.

[34] M. Heisenberg and R. Wolf. *Vision in Drosophila*. Springer Verlag, Berlin, 1984.

[35] R. Hengstenberg, K. Hausen, and B. Hengstenberg. The number and structure of giant vertical cells (vs) in the lobula plate of the blowfly *Calliphora erythrocephala*. *J. Comp. Physiol.*, 149:163–177, 1982.

[36] J. S. Humbert, R. M. Murray, and M. H. Dickinson. A control-oriented analysis of bio-inspired visuomotor convergence (*submitted*). In *Proceedings of the 44th IEEE Conference on Decision and Control*. Seville, Spain, 2005.

[37] J. S. Humbert, R. M. Murray, and M. H. Dickinson. Pitch-altitude control and terrain following based on bio-inspired visuomotor convergence. In *Proceedings of the AIAA Guidance, Navigation and Control Conference*. San Francisco, CA, 2005.

[38] J. S. Humbert, R. M. Murray, and M. H. Dickinson. Sensorimotor convergence in visual navigation and flight control systems. In *Proceedings of the 16th IFAC World Congress*. Praha, Czech Republic, 2005.

[39] K. Karmeier. Early visual experience and receptive field organization of the optic flow processing interneurons in the fly motion pathway. *Visual Neurosci.*, 18:1–8, 2001.

[40] J.J. Koenderink. Optic flow. *Vision Res.*, 26:161–180, 1986.

[41] J.J. Koenderink and A.J. van Doorn. Facts on optic flow. *Biol. Cybern.*, 56:247–254, 1997.

[42] H.G. Krapp, B. Hengstenberg, and R. Hengstenberg. Dendritic structure and receptive-field organization of optic flow processing interneurons in the fly. *J. Neurophysiol.*, 79:1902–1917, 1998.

[43] H.G. Krapp and R. Hengstenberg. Estimation of self-motion by optic flow processing in single visual interneurons. *Letters to Nature*, 384:463–466, 1996.

[44] G. Nalbach. The halteres of the blowfly *Calliphora*, part I: kinematics and dynamics. *J. Comp. Phisiol. A*, 173:293–300, 1993.

[45] G. Nalbach and R. Hengstenberg. The halteres of the blowfly *Calliphora*, part II: three-dimensional organization of compensatory reactions to real and simulated rotations. *J. Comp. Phisiol. A*, 175:695–708, 1994.

[46] A.W. Naylor and G.R. Sell. *Linear Operator Theory in Engineering and Science*. Springer Verlag, New York, 1982.

[47] T. Netter and N. Franceschini. A robotic aircraft that follows terrain using a neuromorphic eye. In *Proceedings of the IEEE/RSJ IROS Conference on Robots and Systems*. Lausanne, Switzerland, October 2002.

[48] W. Reichardt. Autocorrelation, a principle for relative movement discrimination by the central nervous system. In W. Rosenblith, editor, *Sensory Communication*, pages 303–317. MIT Press, New York, 1961.

[49] W. Reichardt. Movement perception in insects. In W. Rosenblith, editor, *Processing of optical data by organisms and machines*, pages 465–493. Academic, New York, 1969.

[50] W. Reichardt. Evaluation of optical motion information by movement detectors. *Biol. Cybern.*, 56:247–254, 1997.

[51] M.B. Reiser, J.S. Humbert, M.J. Dunlop, D. Del Vecchio, R.M. Murray, and M.H. Dickinson. Vision as a compensatory mechanism for disturbance rejection in upwind flight. In *Proceedings of the American Control Conference*. Boston, MA, 2004.

[52] S. Sane and M.H. Dickinson. The aerodynamic effects of wing rotation and a revised quasi-steady model of flapping flight. *J. Exp. Biol.*, 205:1087–1096, 2002.

[53] J. Santos-Victor, G. Sandini, F. Curroto, and S. Garibaldi. Divergent stereo in autonomous navigation - from bees to robots. *International Journal of Computer Vision*, 14:159–177, 1995.

[54] P. Sobey. Active navigation with a monocular robot. *Biol. Cybern.*, 71:433–440, 1994.

[55] M. Srinivasan, J.S. Chahl, K. Weber, S. Venkatesh M.G. Nagle, and S.W. Zhang. Robot navigation inspired by principles of insect vision. *Robotics and Autonomous Systems*, 26:203–216, 1999.

[56] M.V. Srinivasan. How bees exploit optic flow. *Phil. Trans. R. Soc. Lond. B*, 337:253–259, 1992.

[57] M.V. Srinivasan. An image interpolation technique for the computation of optic flow and egomotion. *Biol. Cybern.*, 71:401–415, 1994.

[58] M.V. Srinivasan, M. Lehrer, W.H. Kirchner, and S.W. Zhang. Range perception through apparent image speed in freely flying honeybees. *Visual Neurosci.*, 6:519–535, 1991.

[59] M.V. Srinivasan, M. Poteser, and K. Kral. Motion detection in insect orientation and navigation. *Vision Research*, 39:2749–2766, 1999.

[60] M.V. Srinivasan, S.W. Zhang, M. Lehrer, and T.S. Collet. Honeybee navigation *en route* to the goal: visual flight control and odometry. *J. Exp. Biol.*, 199:237–244, 1996.

[61] G. Stange, S. Stowe, J.S. Chahl, and A. Massaro. Anisotropic imaging in the dragonfly median ocellus: a matched filter for horizon detection. *J. Comp. Physiol.*, 188:455–467, 2002.

[62] N.J. Strausfeld. *Atlas of the insect brain.* Springer, Berlin, Heidelberg, New York, 1976.

[63] Lance F. Tammero and Michael H. Dickinson. The influence of visual landscape on the free flight behavior of the fruit fly *Drosophila melanogaster. J. Exp. Biol.*, 205:327–343, 2002.

[64] Lance F. Tammero, Mark A. Frye, and Michael H. Dickinson. Spatial organization of visuomotor reflexes in *Drosophila. J. Exp. Biol.*, 207(1):113–122, 2004.

[65] S. Thakoor, J. S. Chahl, D. Soccol, B. Hine, and S. Zornetzer. Bio-inspired enabling technologies and new architectures for unmanned flyers. In *Proceedings of the 2nd "Unmanned Unlimited" Systems, Technologies and Operations - Aerospace.* San Diego, CA, September 2003.

[66] K. Weber, S. Venkatesh, and M.V. Srinivasan. Robot navigation inspired by principles of insect vision. *Robotics and Autonomous Systems*, 26:203–216, 1997.

[67] R. Wehner. Matched filters – neuronal models of the external world. *J. Comp. Physiol. A*, 161:511–531, 1987.

[68] T.C.D. Whiteside and G.D. Samuel. Blur zone. *Nature, Lond.*, 225:94–95, 1970.